The Study of Dark Matter in Edge-on Galaxy IC5249

(エッジオン銀河IC5249に付随する暗黒物質の研究)

柳沢 俊史

Abstract

The southern edge-on galaxy IC5249 was observed for an extremely long time with the two passbands in order to investigate the dark matter problem of spiral galaxies. The 61 cm Boller and Chivens telescope of Mt John University Observatory in New Zealand and a wide-field mosaic CCD camera for MACHO research, the MOA-cam2, were used for these observations. As a result, an extended light profile in addition to the thin disk was discovered. This light profile is well described by the thick disk model or the flat halo model. For the case that the light profile is fitted to the flat halo model, the source of the light profile is inferred to be that of a red dwarf by the color information and the mass-to-light ratio of IC5249 obtained by thess observations. The above assumption implies that a flat halo composed of red dwarfs accounts for the total mass of dark matter of IC5249 calculated from the rotation curve. This suggests that all dark matter accompanying spiral galaxies is normal matter composed of baryons.

Contents

List of Figures

List of Tables

Chapter 1

Introduction

Dark matter exists at various scales of the universe. The mass density obtained by analysing vertical motions of stars around solar neighborhood in the Galactic plane(Oort limit) is 1.5 times that of nearby stars and gases(Oort 1960).

Many spiral galaxies including our Galaxy show constant rotation velocity at any place in the galactic plane(Rubin & Ford 1970; Sofue 1996). This indicates the each spiral galaxy possesses dark matter, whose mass is 10-50 times of visible mass(Rubin et al 1980; 1982; 1985).

The total mass of groups of galaxies or clusters of galaxies are estimated by virial theorem assuming that the system is in dynamic equilibrium. Zwicky used this method for the Coma cluster and discovered the total mass was about 400 times that estimated from the number of galaxies in the cluster(Zwicky 1933). From this discovery, Zwicky made the first suggestion of the existence of dark matter.

Inflation, which is thought to occur at the birth of the universe demands that the density parameter Ω_0 becomes almost $\Omega_0 = 1$(Sato 1981; Guth 1981). Here the density parameter Ω_0 is the ratio of the average material density to the critical density. The density parameter Ω_0, which is obtained from dark matter accompanying group of galaxies and cluster of galaxies, is $\Omega_0 = 0.1$ at most(Sargent 1987). In order to explain $\Omega_0 = 1$, cosmological dark matter,

which exists in much larger scale than cluster of galaxies, must be considered.

Two candidates for the origin of dark matter are suggested. One is astronomical dark matter and the other is elementary particle dark matter. For astronomical dark matter, interstellar matter, brown dwarfs, red dwarfs, white dwarfs, neutron stars and black holes are considered. Brown dwarfs are stars which were not able to start hydrogen burning because of their low mass. Red dwarfs are main-sequence stars but dim as their masses are low and therefore the surface temperature is low. White dwarfs, neutron stars and black holes are the evolved results of main-sequence stars. Main-sequence stars evolve into three types of objects through three different processes according to their masses. It is quite difficult to observe these compact objects directly since the radiation from these objects is extremely low at all wavelengths.

For elementary particle dark matter, axions and super-symmetry particles are considered. Axions appear when one requires the symmetry of strong interaction theory to avoid CP violation. Super-symmetry particles appear when one requires natural law not to change against conversion called super-symmetry between Bose particles with integer spin and Fermi particles with half integer spin.

In 1994, Sackett et al observed northern edge-on galaxy NGC5907($15h15m54s$, $56°19'00''$) over a long period of time with an R passband filter. They found a weak extended light profile around NGC5907 which was consistent with dark matter mass expected from its rotation curve(Sackett et al 1994). Here edge-on galaxy is the galaxy which is observable from the side for observers. One may detect light emitted by objects outside of the thin disk, by observing an edge-on galaxy for a long period of time.

The results of Sackett et al are shown in Figure 1.1 as brightness distributions perpendicular to the galactic plane. Dashed-line, dotted-line, and solid-line rep-

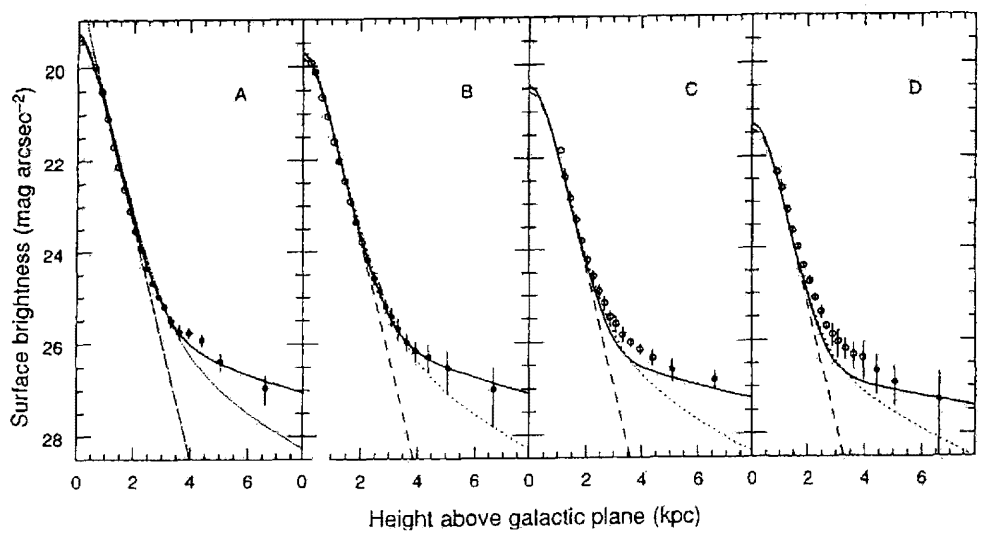

Figure 1.1: The observation result of NGC5907 by Sackett et al. The total surface brightness (in the R band) as a function of height above the galactic plane of NGC5907 for four different cuts (spaced 4.1 kpc apart) perpendicular to the galactic plane.

resent the thin disk model, the thin disk + globular clusters model and the thin disk + halo model, respectively.

Here halo means the density distribution inversely proportional to the square of galactocentric distance, which explains the flat rotation curves of spiral galaxies. From Figure 1.1, it is clear that the results of Sackett et al. fit the thin disk + halo model well. This means the detected light profile is emitted by the dark matter accompanying NGC5907. Sackett et al mentioned that the origin of the light profile was red dwarfs as inferred from the mass-to-light ratio. After their observation, some groups observed NGC5907 with various passband filters(i.e. V, I, J and K) and confirmed the existence of the extended light profile(Lequeux et al 1996, Rudy et al 1997; James & Casali 1998). The results of Lequeux et al and Rudy et al are shown in Figure 1.2 and Figure 1.3, respectively. Both figures show perpendicular brightness to the galactic plane. It is clear that there is extended light profile in addition to the thin disk profile,

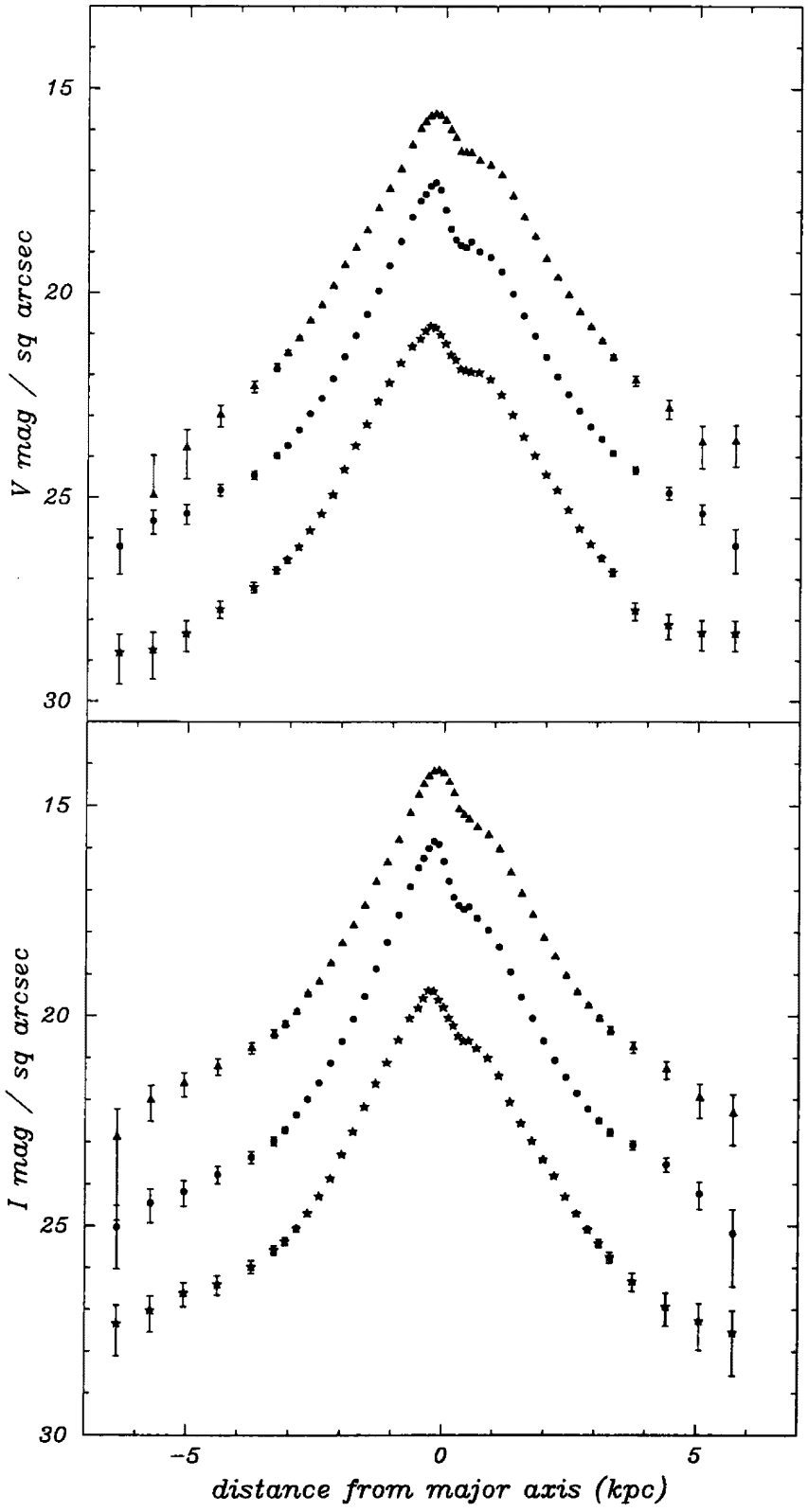

Figure 1.2: The observation result of NGC5907 by Lequeux et al. V (top) and I (bottom) surface brightness profiles perpendicular to the major axis of NGC5907. The magnitude scale corresponds to the lower profile of each set, the other profiles being shifted upwards by 2.5 and 5 mag, respectively.

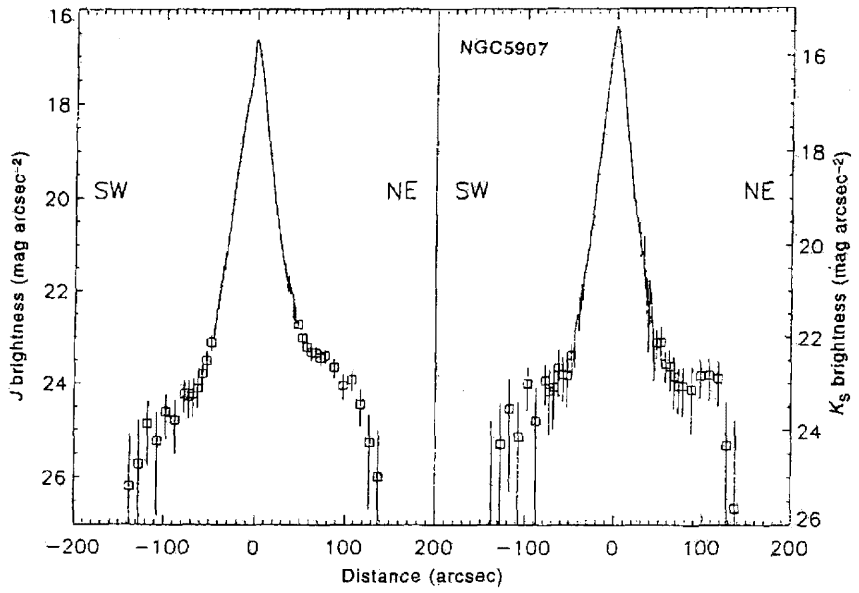

Figure 1.3: The observation result of NGC5907 by Rudy et al. Brightness profiles perpendicular to the major axis of NGC5907 in the $J(1.25\mu m)$ and $K_s(2.15\mu m)$ filters

which is drawn by straight line around the galactic plane. These observations demonstrated that the photometry of edge-on galaxies was effective to resolve dark matter problem which associated with spiral galaxies.

However, observations of other edge-on galaxies were not able to confirm an emission of the light from the a composed of red dwarfs. Casali and James observed NGC100($00h24m00s$, $16°29'00''$) through the K passband and suggested the existence of a brown dwarf halo (Casali & James 1995). Rauscher et al observed ESO240-G11($23h35m08s$, $-48°00'19''$) through the $K_{dark}(2.27\mu m - 2.43\mu m)$ passband but they did not confirm the presence of light corresponding to the halo(Rauscher et al 1998). Some edge-on galaxies were also observed from space with detectors aboard satellites and rockets. Gilmore and Unavane observed UGC711($01h08m40s$, $01°38'59''$), NGC2915($09h26m12s$, $-78°38'00''$), UGC12426($23h13m32s$, $06°33'20''$) and UGC1459($01h59m06s$, $36°03'32''$) with

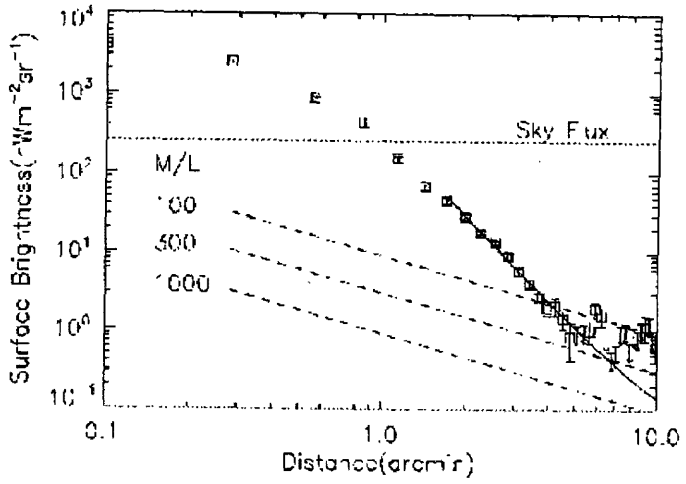

Figure 1.4: The observation result of NGC4565 with rocket borne infrared camera by Uemizu et al. The observed flux and the surface brightness profiles along the minor axis of NGC4565. The brightness is measured by averaging pixels in circular annuli. The best fit to the data is given by the solid line. The expected emission from the halo is shown as dashed lines for different M/L ratios.

ISO (Infrared Space Observatory)(Gilmore & Unavane 1998). Uemizu et al observed NGC4565($12h36m18s$, 25°59′00″) with the infrared rocket(Uemizu et al 1998; Figure 1.4). These observations did not confirm the presence of any light from the halos.

Furthermore a new observational result was introduced. It suggested that the light profile of NGC5907 was formed by the interaction with a nearby galaxy and not emitted by red dwarfs which formed the dark matter. Shang et al observed NGC5907 for a long time with a filter that reduced air glow, and obtained an image with an extremely high signal-to-noise ratio. As a result, they discovered a ring structure, that might be caused by a tidal force of nearby galaxy, dwarf galaxy PGC054419($15h15m48s$, 56°28′00″) and warp structure of

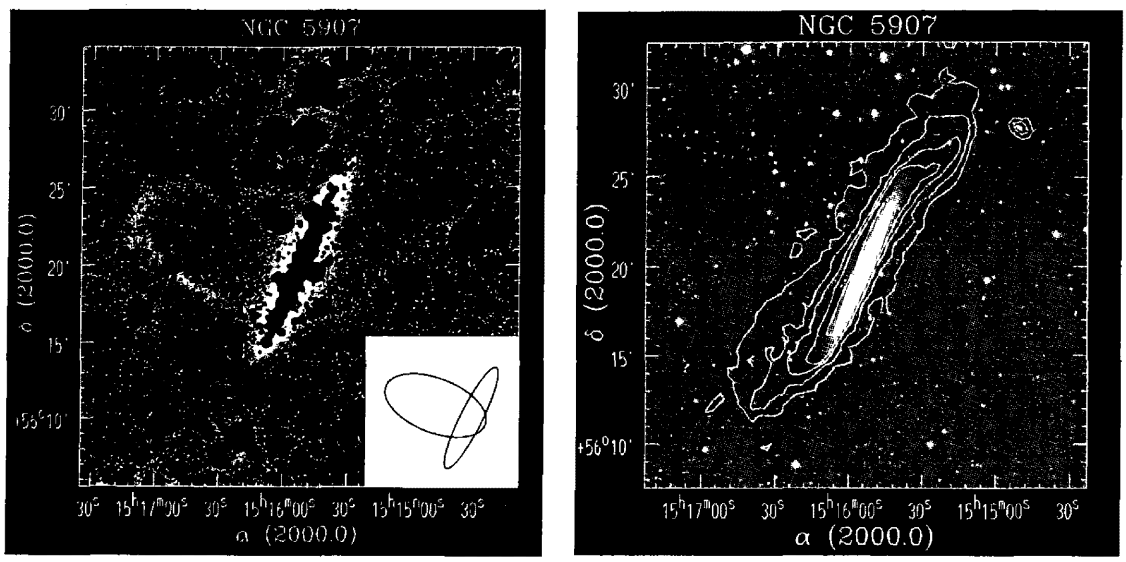

(a) The ring structure

(b) The warp and the dwarf galaxy PGC 54419

Figure 1.5: The observation result of NGC5907 by Shang et al.

NGC5907(Shang et al 1998; Figure 1.5). Warp is a phenomenon that galactic disk is distorted at far distant side from galactic center. This observation suggested that NGC5907 was affected by a nearby galaxy.

From the observation of Shang et al, Zheng et al inferred that the light profile of NGC5907 observed by Sackett et al came from a ring structure and unremovable stars in the data analysis(Zheng et al 1999). Lequeux et al observed NGC5907 again, and indicated that the light profile observed by Sackett et al was a consequence of the collision of a small elliptical galaxy on the basis of the observed color information and N-body numerical simulation(Lequeux et al 1998).

Concerning our Galaxy, observations indicated that dark matter was not composed of red dwarfs. Bahcall et al observed the high galactic latitude region

with HST(Hubble Space Telescope). From observed number of stars, they concluded that contribution ratio of red dwarfs to the dark matter of our Galaxy was less than 6 %(Bahcall et al 1994; Flynn, Gould & Bahcall 1996).

In addition to the observations of edge-on galaxies for a long period of time and observation of high galactic latitude with HST, a method using a microlensing effect is another way to find dark matter in our Galaxy. This method was suggested by Paczynski in 1986(Paczynski 1986). The MACHO collaboration of Alcock et al and the EROS group of Aubourg et al discovered first the microlensing events in the Large Magellanic Cloud(LMC) in 1993(Alcock et al 1993; Aubourg et al 1993). Then many other observations started namely OGLE(Udalski, Kubiak & Szymanski 1997), DUO(Alard et al 1995), AGAPE(Ansari et al 1997) and VATT-Columbia(Tomaney & Cotts 1996). Our group MOA started its observation in 1996. The MACHO collaboration gave an interpretation that 50 % of dark matter of our Galaxy was made of the stars with mass of $0.5M_{\odot}$ from their first two years of results(Alcock et al 1997). They also analysed the data with the EROS group and constrained the contribution of the stars in the mass range $10^{-7}M_{\odot} < m < 10^{-3}M_{\odot}$ to the dark matter was less than 25 %(Alcock et al 1998).

The three observational results above can be discussed as follows. The observational results of edge-on galaxies and high galactic latitude with HST almost seems to deny that halos of spiral galaxies are composed of red dwarfs. In consideration of the mass given by microlensing observation as $0.5M_{\odot}$, the objects are likely to be white dwarfs. However, in this case, the mass function of stars at galaxy formation(IMF: Initial Mass Function) must have a peak around 2 $M_{\odot}$(Adams & Laughlin 1997; Chabrier, Segretain & Mera 1996). Because main-sequence stars with mass of 2 $M_{\odot}$ evolve to white dwarfs with

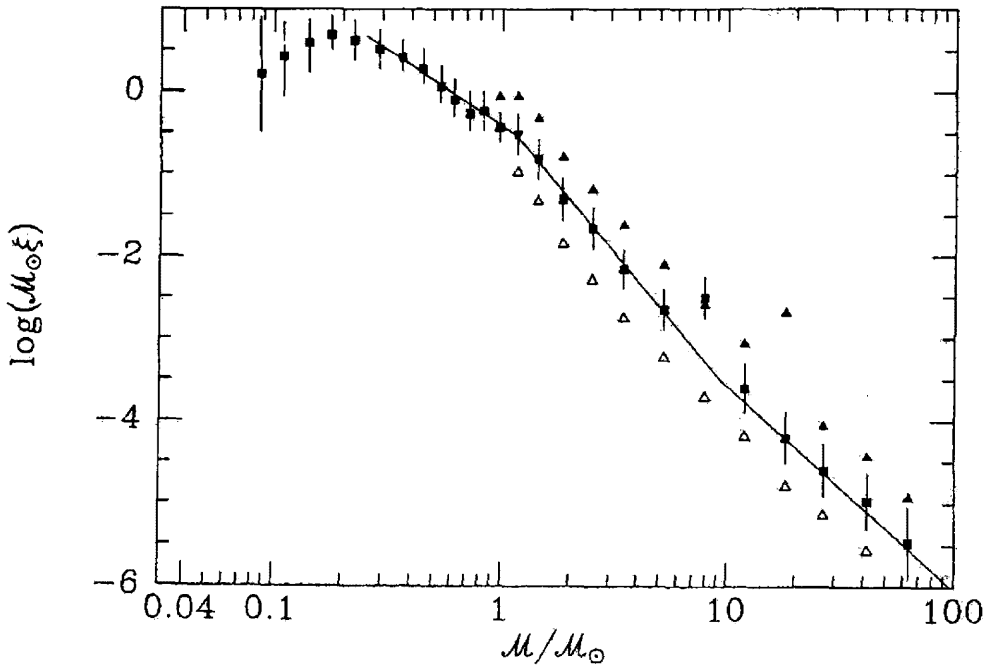

Figure 1.6: The initial mass function from Scalo(1986).

mass of 0.5 $M_\odot$ as a result of mass ejection. Initial mass function, which has a peak around 2 $M_\odot$, is hard to understand from present mass function of stars, which is inversely proportional to the third power of mass(Scalo 1986; Figure 1.6).

Also, such white dwarfs must be bright in their main-sequence epoch, and so, distant(old) galaxies must also be bright. Then the expected number of distant galaxies is more than is observed(Charlot & Silk 1995). Moreover, the abundance of helium, carbon and nitrogen produced by such white dwarfs is high and not consistent with those of observed in the sun(Charlot & Silk 1995). Brown dwarfs are unlikely for the halo objects from the expected mass by microlensing observation. Primordial black holes, which were made at the beginning of the universe, are suggested as another candidate for halo objects(Yokoyama 1997). In case primordial black holes are dominante in the halo of our Galaxy, gravi-

tational waves from the binary systems of these primordial black holes must be detected by LISA(Laser Interferometer Space Antenna)(Ioka,Tanaka & Nakamura 1998).

The above discussions show that, as dark matter candidates for our Galaxy red dwarfs, white dwarfs and brown dwarfs are almost excluded, and only primordial black holes will remain. However, it is too early yet to decide that primordial black holes comprise the dark matter of our Galaxy. The interpretation of the observational results by the MACHO collaboration depends strongly on the halo model adopted. Different interpretations are possible using different halo models. Although the MACHO collaboration adopted standard halo model(flat rotation curve and spherical mass distribution), Honma and Kan-ya used a model in which the rotation curve declines within observation error, and predicted that 90 % of Galactic dark matter was composed of 0.06 $M_{\odot}$ objects using the observational results of the MACHO collaboration(Honma & Kan-ya 1998; Figure 1.7).

Objects of mass 0.06 $M_{\odot}$ correspond exactly to brown dwarfs. Moreover, infrared observations of edge-on galaxies except NGC5907 which detected no halo emission used only the spherical standard halo model to reproducing observed data. Other models of the halo were never used.

The assumption that the halo must be spherical may lead to an incorrect interpretation of the dark matter problem in spiral galaxies. If the halo is extremely flat, microlensing objects decrease toward the Magellanic Cloud direction, and so, different interpretation may be possible from the same observation result(Sackett & Gould 1993; Gould, Miralda-Escude & Bahcall 1994). If edge-on galaxies possess flat halos, it is impossible to reproduce the observed data by a spherical halo model because the shape of a flat halo is quite different

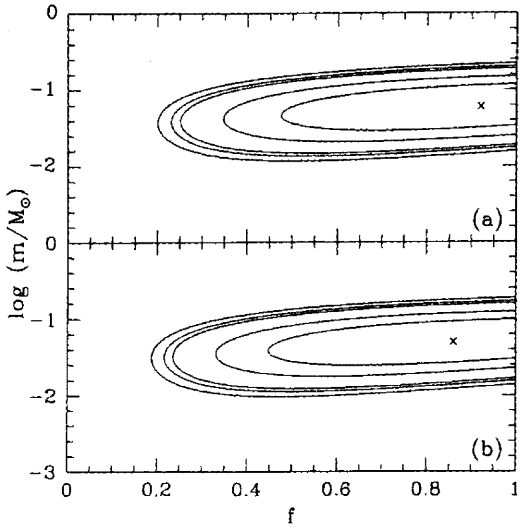

Figure 1.7: Likelihood coutours of the MACHO mass m and the halo MACHO fraction f for (a) Hernquist model(Hernquist 1990) and (b) Plummer model(see Binney & Tremaine 1987), respectively. The contours enclose total probabilities of 34%, 68%, 90%, 95% and 99%. The crosses denote the peak of likelihood.

from that of a spherical halo. In other words, the halo does not exist if one uses a spherical halo model to fit the observed data. The expected number of red dwarfs from HST observations toward the high galactic latitude must strongly depend on the adopted model. As a result, the contribution of red dwarfs to the Galactic dark matter is variable. It must be stressed here that quite different interpretations are given from the same observational results depending on the adopted halo model.

For a long time, many astronomers assumed that halos must be spherical. However, the existence of a flat halo was confirmed from the observational side and also theoretical side, recently. Sackett et al observed the galaxy NGC4650A($12h44m18s, -44°44'00''$) holding a ring structure. They examined the brightness and gas dynamics of the galaxy and concluded that the axial ratio of the halo in association with the galaxy was 0.3-0.4(Sackett &

Sparke 1990; Sackett et al 1994). Here the axial ratio is the ratio of minor axis of the galaxy to its major axis. Olling detected a gas flare of the galaxy NGC4244($12h17m30s, 37°49'00''$) by observing emission from the H_I region of the galaxy, and showed that the axial ratio of the halo was 0.2(Olling 1996). A flare is a phenomenon that the thickness of the galactic disk increases with to the increasing galactocentric distance. In some edge-on galaxies, warps were observed. It is suggested that the warp is the result of existence of a fat halo tilting against the galactic disk(Dekel & Shlosman 1983; Toomre 1983; Sparke & Casertano 1988). Hoffner and Sparke examined an evolution of the halo and concluded that one fifth of their studied system have flat halos with the axial ratio of 0.4(Hoffner & Sparke 1994). The halo, which was formed by putting baryonic gas into non-baryonic cold dark matter, was also shown to be flat from N-body numerical simulation(Dubinski 1994).

In order to solve the problem of dark matter accompanying spiral galaxies, it is quite important to consider the halo model. For this purpose, the observations, which were done for NGC5907 should be applied to other edge-on galaxies and the observed data should be analysed taking account of the possibility of a flat halo. Previous observations, except for NGC5907, did not consider this possibility. In this thesis, I interpreted the observed results for IC5249 in the context of a flat halo model. As a result, I obtained knowledge of dark matter associated with the edge-on galaxy IC5249.

Chapter 2

MOA project

The details of MOA project are presented in this chapter.

There is a possibility that dark matter in our Galaxy is made of MACHOs(MAssive Compact Halo Objects), which are extremely dark stars like red dwarfs, brown dwarfs and white dwarfs. MACHOs are too dim to be observed by photometry using a normal optical telescope. The most effective method for detecting them is considered to be observing microlensing effects. The microlensing effect happens as follows. When a MACHO passes in front of a background normal star,

the light from the normal star is bent by the gravitational field of the MACHO as in a lens. As a result, the brightness of the background star is amplified temporarily during the MACHO passage(see Figure 2.1). Microlensing effects are quite rare phenomena, because two objects(MACHO and background star) must be aligned on the observer's line of sight. Observers have to monitor the brightness of about a few millions of stars every night in order to detect microlensing effects. For this purpose, a dense region of stars such as LMC(the Large Magellanic Cloud), SMC(the Small Magellanic Cloud) or the Galactic bulge should be observed using telecopes with a wide field of view and large CCD cameras. The MACHO collaboration, which is composed of American and Australian astronomers, observed LMC at Mt Stromlo Observatory in Australia

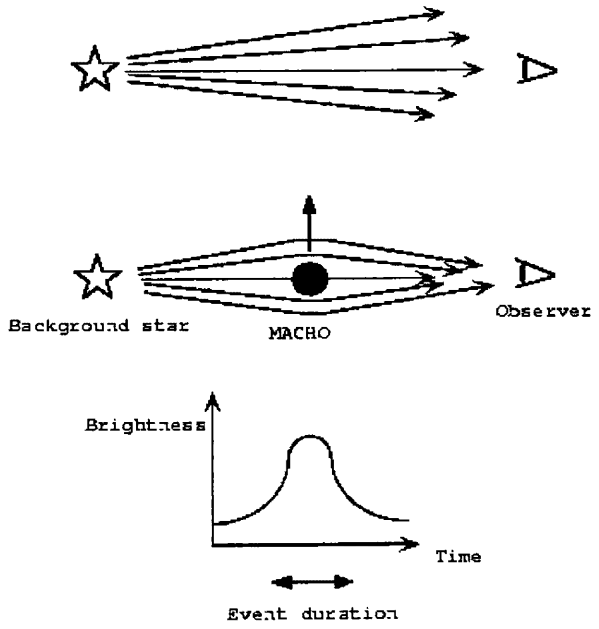

Figure 2.1: The microlensing effect.

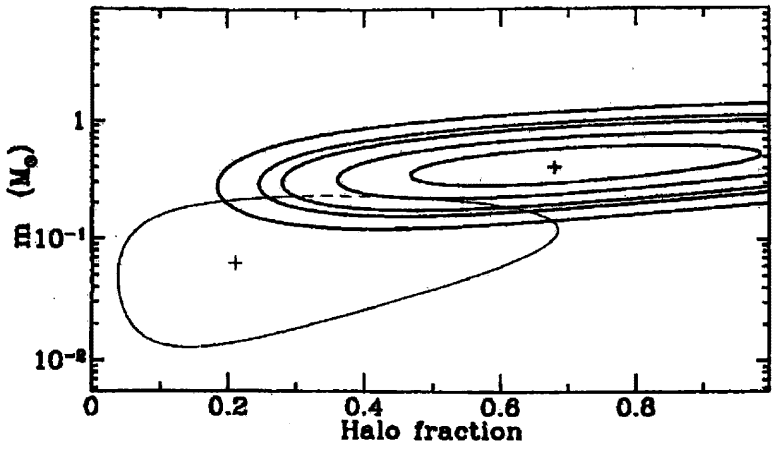

Figure 2.2: The observation result of the MACHO collaboration. Likelihood contours of MACHO mass m and halo MACHO fraction f for a delta-function mass destribution, for standard halo model. The most likely value is indicated with a plus sign, and the contours enclose total probabilities of 34%, 68%, 90%, 95% and 99%. The light line shows the 90% contour from the first year result of the MACHO collaboration(Alcock et al 1996).

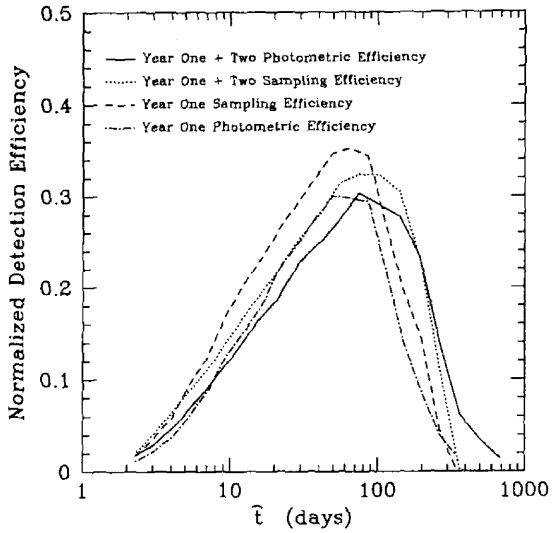

Figure 2.3: Microlensing detection efficiency of the MACHO collaboration as a function of of event time scale. The dotted line shows the 'sampling efficiency, and solid line shows the 'photmetric efficiency(see Alcock et al 1997). For comparison the corresponding curves from the first year result are shown(Alcock et al 1996).

with a 1.27 m telescope(F3.9) and two large CCD cameras which contain 4 CCD chips of 2K $\times$ 2K. They detected 8 events by observing 8.5 million stars every night for two years. While their observations showed clearly the existence of a MACHO, its mass and fraction within Galactic dark matter were still unclear. In Figure 2.2, the results of the MACHO collaboration are shown(Alcock et al 1997). The horizontal axis shows the fraction of Galactic dark matter, and the vertical axis shows the typical mass of MACHOs. The most likely value is indicated with plus sign, and the contours represent the most likely probabilities of 34%, 68%, 90%, 95% and 99%, respectively. The light line shows the 90% contour from the observation of the first year(Alcock et al 1996). They concluded that the half of Galactic dark matter was composed of compact objects of $0.5M_{\odot}$. However, from Figure 2.2, it is obvious that the fraction and the mass of MACHOs were not determined accurately. This arises from the small number of events. Detection efficiency of microlensing effect for the MACHO

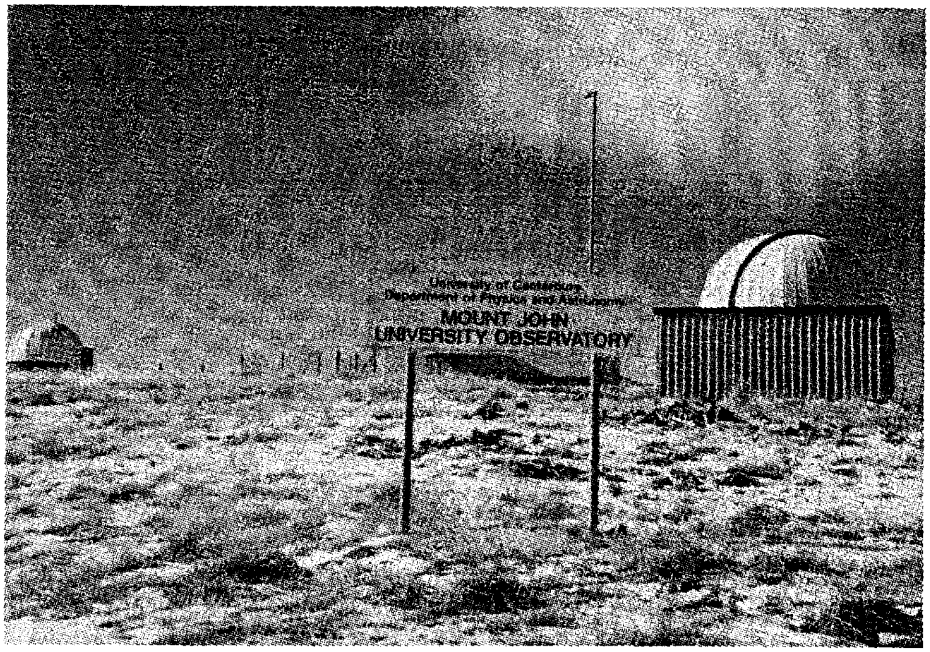

Figure 2.4: Mt John University Observatory(MJUO)

collaboration are shown in Figure 2.3. The horiozontal axis shows the event duration of microlensing effect, and the vertical axis shows the detection efficiency. Since the MACHO collaboration observed LMC once per night, the detection efficiencies of 1-10 days events was extremely low. The event duration is proportional to root of the mass of a MACHO, which means it was difficult for the MACHO collaboration to detect events caused by MACHOs with low mass. Observation ,which is able to detect many events and has a good detection efficiency for short events, is necessary to decide the properties of MACHOs accurately.

In order to compensate for the weak point of the MACHO collaboration, the MOA(Microlens Observation in Astrophysics) collaboration started observations at MJUO(Mt John University Observatory; Figure 2.4) in New Zealand in May 1996. The collaboration involved Japanese and New Zealand scientists;

MJUO is located at latitude 44 degrees south which is the most southern observatory used for microlensing observations. The Las Campanas Observatory and the La Silla Observatory, which are used by the OGLE and the EROS groups, are located at the latitude 29 degrees south. At these observatories, the air mass for LMC in winter time is about 4.5 which makes the observation of LMC impossible (Palanque-Delabrouille et al 1998). The latitude of Mt Stromlo Observatory is 35 degrees south, but the observation of LMC in winter time is impossible owing to a structural problem of the telescope. Mt John Observatory has a large advantage in terms of ability to observe LMC all the year round. The longest observation time in the winter time, when weather conditions are stable, is about 14 hours.

The observational equipment used were the 61 cm Boller and Chivens reflector(Figure 2.5) and the MOA-cam1 until 1998 July. The MOA-cam1 is a mosaic CCD camera, which contains 9 CCD TC215 chips manufactured by Texas Instruments of Japan(Yanagisawa 1996; Figure 2.6). The MOA-cam1 observes a $30' \times 30'$ region of the sky with one exposure. We observed 1.4 million stars in LMC and SMC 2-3 times per night to detect short events. As a result, one candidate in LMC and one candidate in SMC were observed(Sumi 1999). Many variable stars were detected by the photometries of 1.4 million stars. In many variable stars, strange variable stars, which show no change of color, were discovered(Noda 1999). The southern edge-on galaxy IC5249 was observed for a long period of time in July 1997 to study the dark matter problem from the different point of view except microlensing. This program of observation detected weak emission from the halo and restricted the halo component of IC5249(Abe et al 1999). In July 1998, we discovered a planet with mass of Earth-Neptune by dense observation of the event to which MACHO collaboration alerted(Rhie et al 1998).

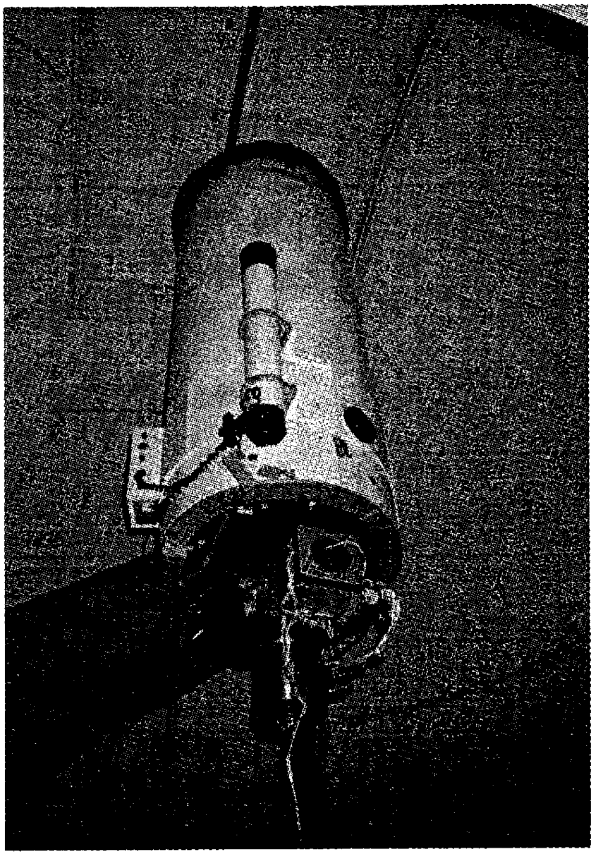

Figure 2.5: 61cm Boller and Chiven reflector.

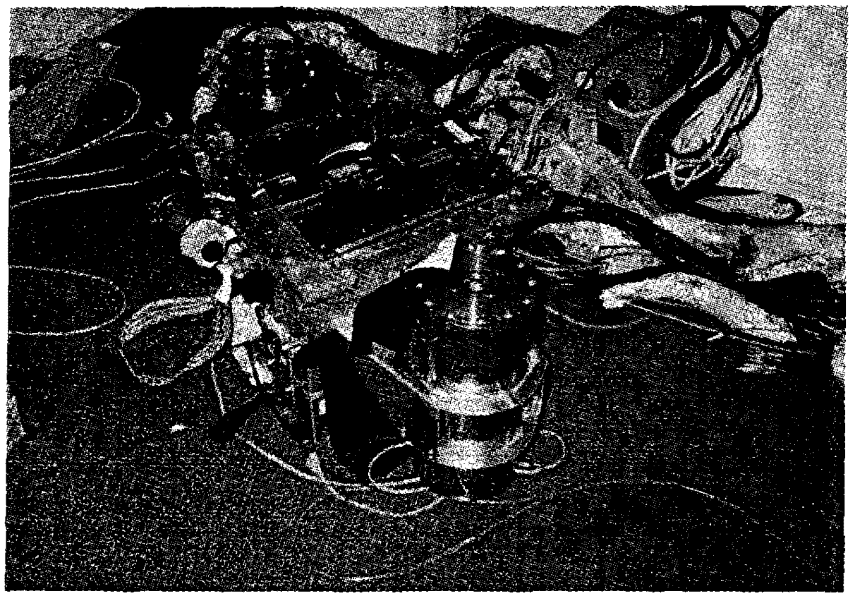

Figure 2.6: The wide field mosaic CCD camera, MOA-cam1.

A new mosaic CCD camera MOA-cam2 was mounted on the Boller and Chivens reflector and started the observation from 1998 August. The MOA-cam2 has three large ST-002A CCD chips manufactured by the Scientific Imaging Technologies, Inc. ST-002A is back-illuminated chip with 2K $\times$ 4K pixels. The MOA-cam2 has a 6 cm $\times$ 9 cm image area, which is 6 times as large as that of the MOA-cam1, and its quantum efficiency is twice as high as that of the MOA-cam1. This means that the MOA-cam2 has observational capability about 10 times as large as that of the MOA-cam1, and so the MOA-cam2 is expected to detect many events. Now, we are constructing the system, which can carry out the real-time analysis of the observed data, in MJUO. We observed IC5249 for a long time with the MOA-cam2 on photometric nights from 1998 August to November. The results are shown in this thesis. From 1999 April, the search for optical counterpart of Gamma Ray Burst was also started.

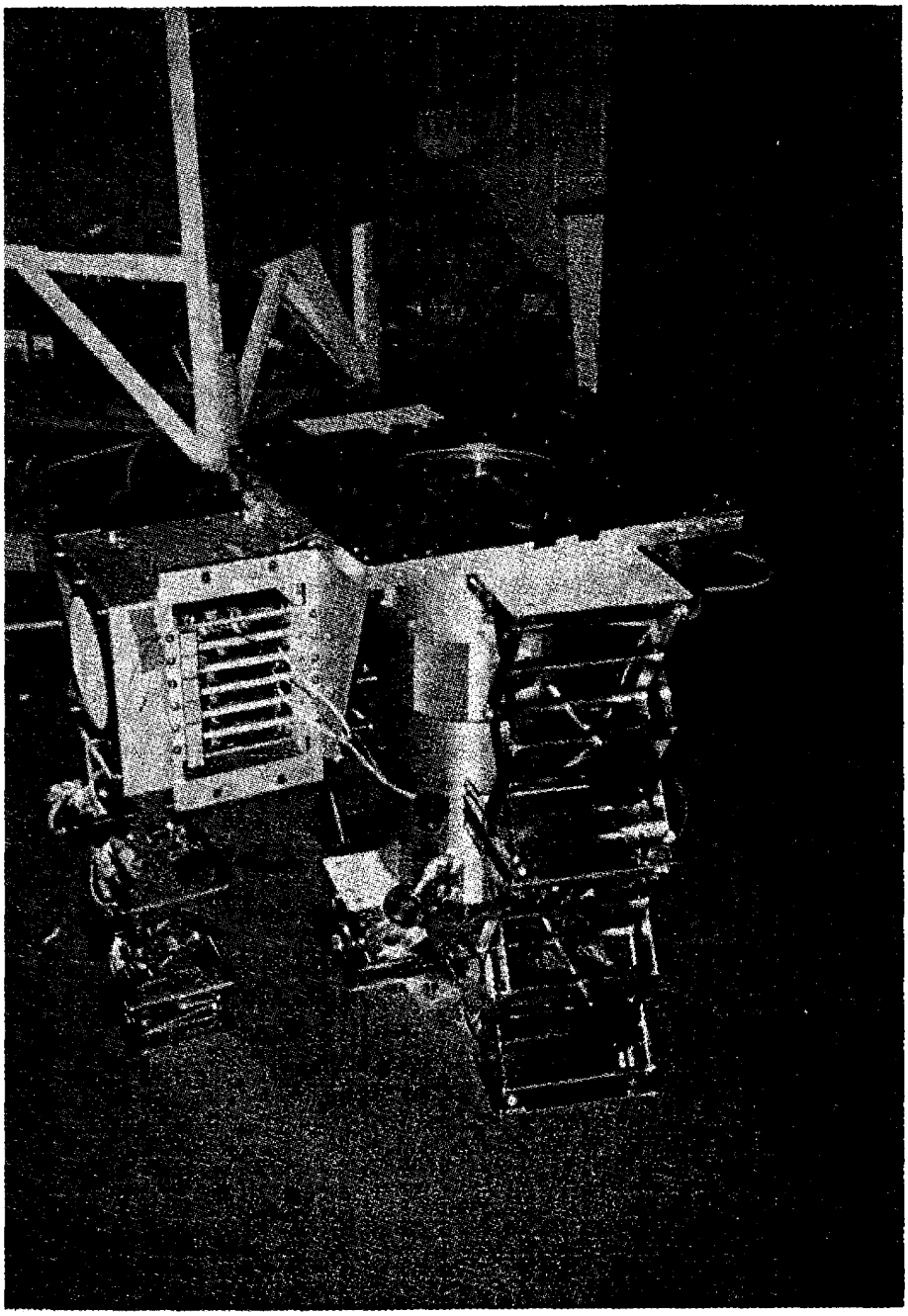

Figure 2.7: The wide field mosaic CCD camera, MOA-cam2.

Chapter 3

Previous Observations of IC5249

In this chapter, previous observations of the southern edge-on galaxy IC5249 ($RA = 22h47m7s$, $\delta = -64°49'54''$)are described.

IC5249 was included in the Southern Sky Redshift Survey (da Costa et al 1991) and in the Southern Sky Survey(Mathewson et al 1992). Relevant parameters taken from these two surveys are the type of galaxy, Sc or Sd; the inclination angle, $\approx$ 89°; the magnitude in the I passband $m_I \approx 13.1mag$; the central surface brightness in I passband $\mu_I = 20.1mag/arcsec^2$; the emission amount from H_I regions $H_I flux = 27.85Jykm/s$; the recession velocity(optical) $\approx 2332km/s$; the recession velocity (H_I) $\approx 3264km/s$; the recession velocity(Tully-Fisher relation) $\approx 2320\pm100km/s$; the rotation velocity(H_I) $\approx 100km/s$. The major- and the minor-axis of the contour of $23.5mag/arcsec^2$ in the I passband are 184″ and 17″, respectively.

The H_I synthesis observations of IC5249 were obtained with ATCA(Australia Telescope Compact Array) on 1992 October 18(Levasseur et al 1992). The total time on source was about 12 hours. The 8 MHz bandwidth centered on 1409 MHz was divided into 512 channels , which resulted in a velocity resolution of $3.35km/s$. The H_I distribution overlaided onto an optical image of IC5249 from DSS is shown in Figure 3.1. The H_I extent of IC5249 was about

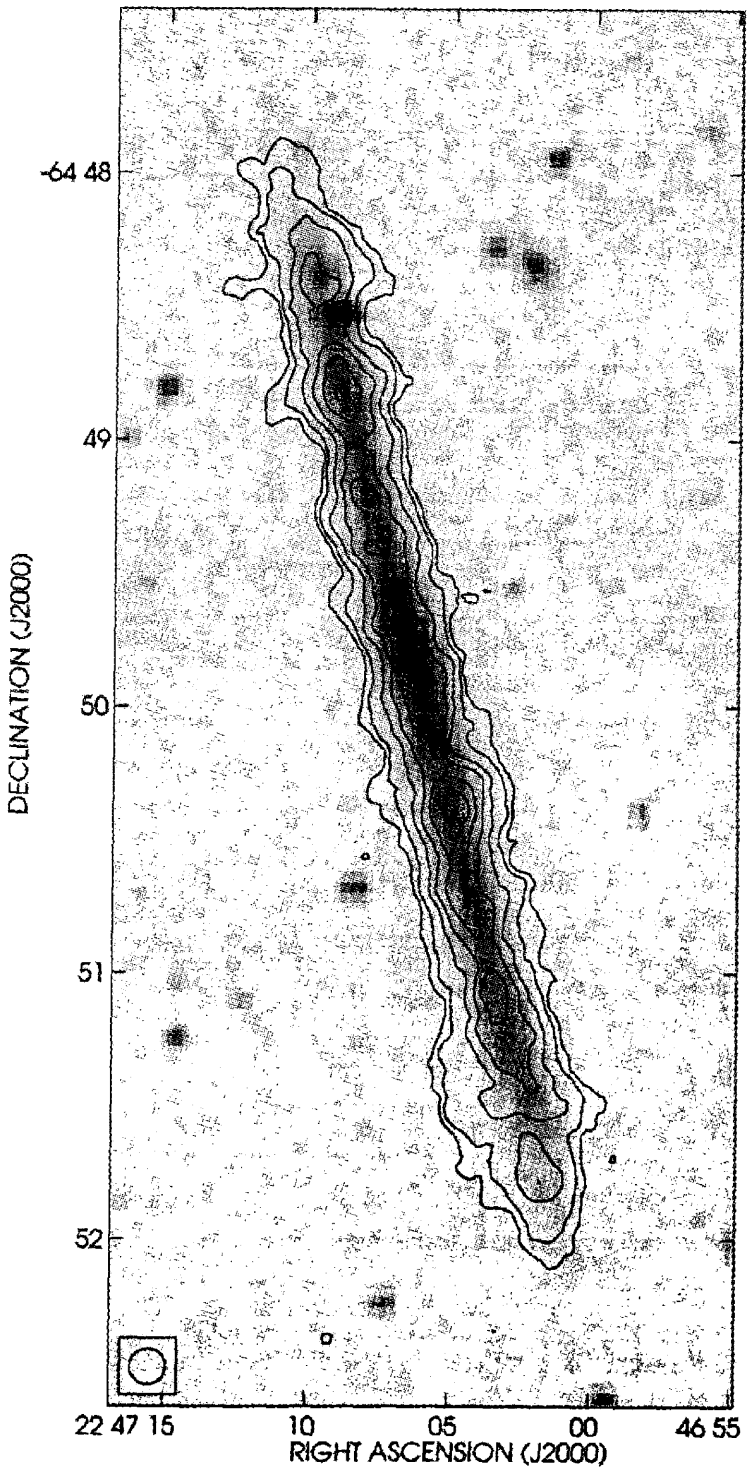

Figure 3.1: H_I distribution of the galaxy IC5249 overlaid on an optical image obtained from the Degital Sky Survey(DSS). The contour levels are 0.05, 0.1, 0.2, 0.3, 0.4 and 0.5 Jy/beam km/s and the angular resolution is 8″. North is to the top, and east to the left.

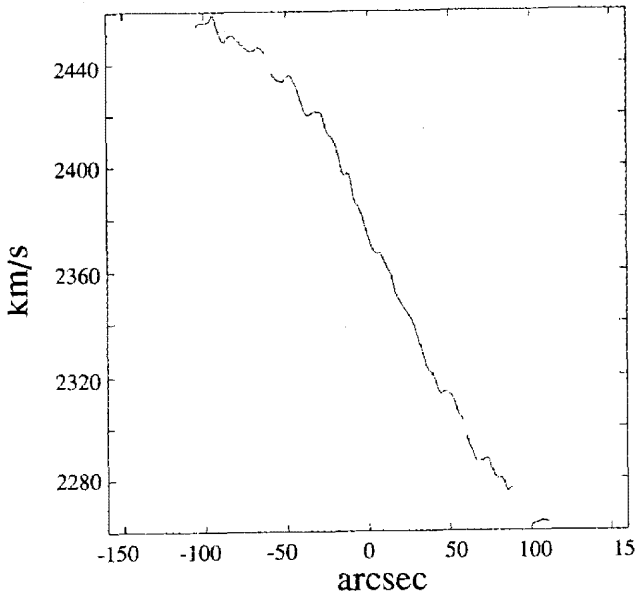

Figure 3.2: The rotation curve of IC5249.

$280 \times 24''$ (at $N_{H_I} = 9 \times 10^{20} atoms/cm^2$) compared with $246'' \times 22''$ of optical contour of $25.0 mag/arcsec^2$ in the R passband. The integrated H_I flux was about $20 Jykm/s$, which corresponded to an H_I mass of about $6 \times 10^9 M_\odot$ assuming a distance of 36 Mpc. The total H_I flux quoted by Mathewson et al using the 64 m Parkes radio telescope was $27.85 Jykm/s$, which was considerably higher(30%) than that obtained by Levasseur et al. This indicates that there is a more extended hydrogen emission, which has been filtered out with the ATCA interferometer. The current H_I distribution shows no evidence of flaring and warping. The rotation curve of IC5249, which was obtained by averaging the H_I velocity field along the galactic plane(width $22''$), is displayed in Figure 3.2. The systematic velocity of IC5249 is $\approx 2365 km/s$. A linear rise of rotation velocity, which is relative velocity to the systematic velocity, is seen within a radius of r=$40''$ or 7.0 kpc. Beyond that radius, the rotation curve slowly turns over and seems to flatten at about r=$100''$ or 17.5 kpc, although more sensitive data are needed to confirm this. The maximum observed rota-

tion velocity is about $100km/s$. The total mass of IC5249 within the observed H_I disk(r$\leq$140$''$ or 24.5 kpc) is about $5.7 \times 10^{10} M_{\odot}$. This assumes that the mass inside 24.5 kpc is distributed approximately spherically and yields a mass ratio $log(M_{H_I}/M_{tot}) \approx -0.98$. This correlates well with the expected value of roughly -1 for Sc/Sd galaxies(Roberts & Haynes 1994).

Our MOA collaboration observed IC5249 on the nights of 1997 July 4 and 6 using the 0.6 m Boller and Chivens telescope and the MOA-cam1. The MOA-cam1 was the CCD camera used for microlensing search(Abe et al 1999). Total exposure time in the R passband was 5 hours and 20 minutes. The final image, that was stacked with many frames, and observational results are shown in Figure 3.3 and 3.4, respectively. In thess observations, another light profile in addition to the thin disk was detected. In Figure 3.4, the perpendicular light profile to the galactic plane, where distance from minor axis is 7.5 kpc, is shown.

The dashed line is the best fit for the thin disk model(equation (3.1)) from 1-2 kpc with scale height $h_0 = 640pc$ and scale length $H_0 \approx 11kpc$. The dashed-dotted curve is the best fit for the double disk model(equation (3.2)) with the parameters given in Table 3.1. The dotted curve is the best fit for the thin disk + spherical halo model (equation (3.3)), which explains the dark matter in IC5249, with the parameters given in Table 3.2. The solid curve is the best fit for the thin disk + globular cluster model(equation (3.4)) with the parameters given in Table 3.3. Equations for each model are described in equations (3.1)-(3.4). Parameters for the double disk model, the thin disk + spherical halo model and the thin disk + globular cluster model are shown in Table 3.1, 3.2 and 3.3, respectively.

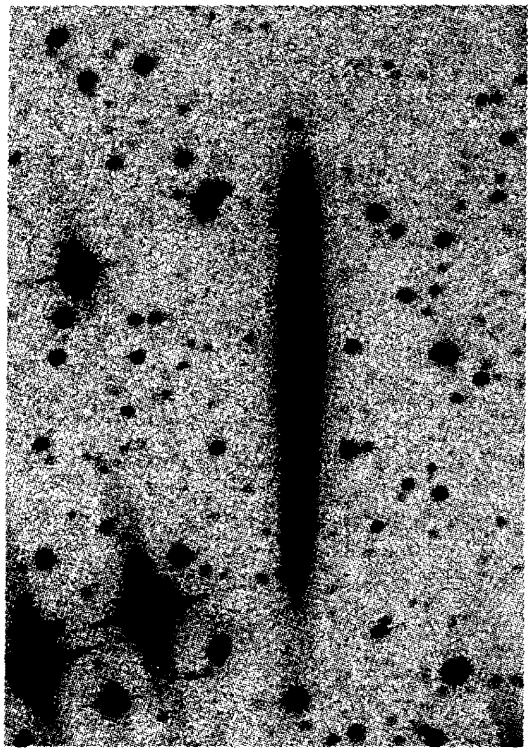

Figure 3.3: The image of IC5249 obtained with MOA-cam1.

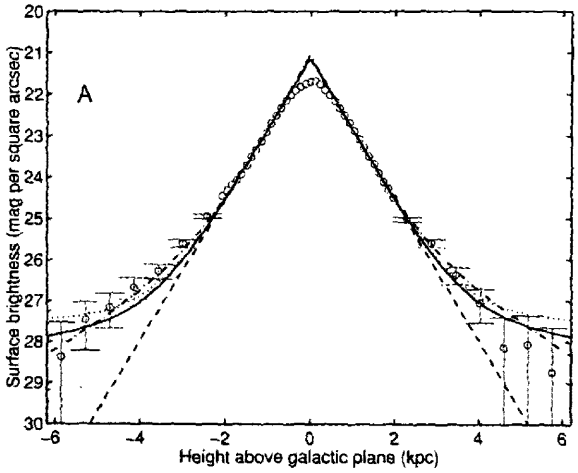

Figure 3.4: Brightness profiles perpendicular to the major axis of IC5249. The dashed lines, the dashed-dotted curve, the the dotted curve, the solid curve are best fit for 'thin disk model', 'double disk model', 'thin disk + spherical halo model' and 'thin disk + globular cluster model', respectively.

$$L(R,z) = L_0 exp(-R/H_0) exp(-|z|/h_0) \tag{3.1}$$

$$L(R,z) = L_0 exp(-R/H_0) exp(-|z|/h_0) + L_1 exp(-R/H_1) exp(-|z|/h_1) \tag{3.2}$$

$$L(r,R,z) = L_0 exp(-R/H_0) exp(-|z|/h_0) + L_{dm}(r/H_0)^{-2} \tag{3.3}$$

$$L(r,R,z) = L_0 exp(-R/H_0) exp(-|z|/h_0) + L_{gc}(r/H_0)^{-3.5} \tag{3.4}$$

Table 3.1: Parameters for the double disk model

Parameter	Corresponding Value
$h_0(pc)$	570
$H_0(kpc)$	11 ± 2
$h_1(pc)$	1690
$H_1(kpc)$	6 ± 1
L_1/L_0	0.135
Reduced χ^2	1.2

Table 3.2: Parameters for thin disk + spherical halo model

Parameter	Corresponding Value
$h_0(pc)$	630
$H_0(kpc)$	11 ± 2
L_{dm}/L_0	4.5×10^{-6}
Reduced χ^2	1.7

Suppose that main-sequence stars with same masses are distributed as a spherical halo(see equation(3.3)), the total mass of spherical halo is calculated.

Table 3.3: Parameters for thin disk + globular cluster model

Parameter	Corresponding Value
$h_0(pc)$	620
$H_0(kpc)$	11 ± 2
L_{gc}/L_0	2.8×10^{-4}
Reduced χ^2	1.7

The total luminosity of the spherical halo is obtained by integrating the halo profile in equation (3.3) $L_{dm}(r/H_0)^{-2}$ from galactic center to cut off radius r_c.

$$4\pi \int_0^{r_c} r^2 L_{dm}(r/H_0)^{-2} dr = 4\pi r_c L_{dm} H_0^2 \tag{3.5}$$

Multiplying the total luminosity by M/L(mass-to-light ratio) of the main-sequence star with the mass, leads the total mass of the spherical halo.

$$M_{total} = 4\pi r_c L_{dm} H_0^2 \frac{m}{L} \tag{3.6}$$

Comparing the total mass calculated from equation (3.6) with the mass of the spherical halo($5.7 \times 10^{10} M_\odot$) obtained from rotation curve of IC5249(see Figure 3.2) extracts the upper limit on the ratio of the main sequence star in dark matter of IC5249. The mass-to-light ratio(Baraffe et al 1997) of each main-sequence star, the total mass of the stars and the upper limit of the contribution from the stars are shown in Table 3.4. The uncertainty in the photometry in the halo corresponds to an uncertainty in M_{total} of about 50 %. The upper limit represents the value at the 95 % confidence level. Table 3.4 indicates that a halo composed entirely of main-sequence stars heavier than $0.13 M_\odot$ is excluded, and that less than 20 % of the halo can be made up of main-sequence

stars heavier than $0.30M_{\odot}$. The results are shown in Figure 3.5 and compared with some Galactic results. These results were obtained by the gravitational microlensing observations of the EROS and MACHO collaborations(Alcock et al 1998; Afonso et al 1999) and by infrared photometry for four external galaxies (Gilmore & Unavane 1998).

Table 3.4: Galactic mass fraction of main-sequence halo stars in IC5249

Mass of star($M_{\odot}$)	Mass-to-light ratio(in $M_{\odot}/L_{\odot}$)	Total mass($M_{\odot}$)	Upper limit of mass fraction(%
0.13	88.3	1.90×10^{10}	66.6
0.15	65.5	1.40×10^{10}	49.0
0.20	40.3	8.7×10^{9}	30.4
0.30	23.8	5.2×10^{9}	18.4
0.40	16.5	3.6×10^{9}	12.6
0.50	7.9	1.9×10^{9}	6.6
0.60	3.1	7.8×10^{8}	2.7
0.70	1.3	3.6×10^{8}	1.3
0.80	0.36	1.2×10^{8}	0.4

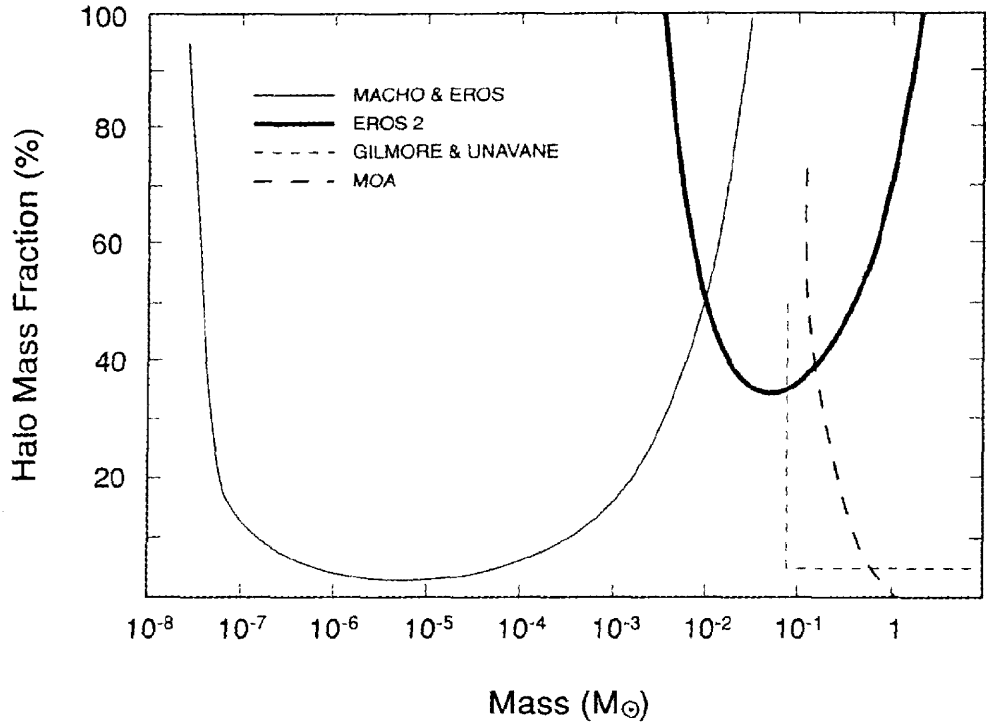

Figure 3.5: Upper limit to the contribution of main-sequence halo stars to the total mass of IC5249 inside a galactocentric radius of 24.5 kpc. Corresponding results for other galaxies obtained by gravitational microlensing and infrared photometory are also included. The thin solid line denotes the upper limit for low-mass objects of any type in the Galactic halo reported by Alcock et al. (1998) using the gravitational microlensing technique, and thick solid line is similar limit due to Afonso et al.(1999). The thinned dashed line denotes an upper limit for main-sequence stars that was obtained by Gilmore & Unavane (1998) for four external galaxies by infrared photometry.

Since the light profile in association with the thin disk detected by the MOA-cam1 was extremely weak, it is too difficult to decide its exact shape and components. The observations started in 1998 August using the MOA-cam2. The MOA-cam2 has twice the quantum efficiency of the MOA-cam1. Again, IC5249 was observed with the MOA-cam2 through the V and I passbands and restricted its shape and components more accurately. The results and their interpretation are given in this later thesis.

Chapter 4

Equipments used for the Observations

In this chapter, the equipment used for the observations are presented. In particular, the wide-field mosaic CCD camera MOA-cam2, which was prepared mainly by myself, is described in detail.

The sky coverage of the MOA-cam1 that was used until 98 July was 30×30 square arcmin. This extent is about a half of that of camera used by the MACHO collaboration(42×42 square arcmin, Alcock et al 1993). In order to study more events, a wide field camera with sensitivity more than 10 times greater than that of the MOA-cam1 was built. This is the MOA-cam2 instrument. The MOA-cam2 was assembled and tested at the National Astronomical Observatory of Japan(NAOJ). Three CCD chips with 2048×4096 pixels were used which had been manufactured by Scientific Imaging Technologies, Inc(SITe)(Figure 4.1). The MOA-cam2 has three major advantages over the MOA-cam1:

1) The image area is six times larger,

2) The CCD chip has two times higher quantum efficiency,

3) The CCD chip has three abuttable sides.

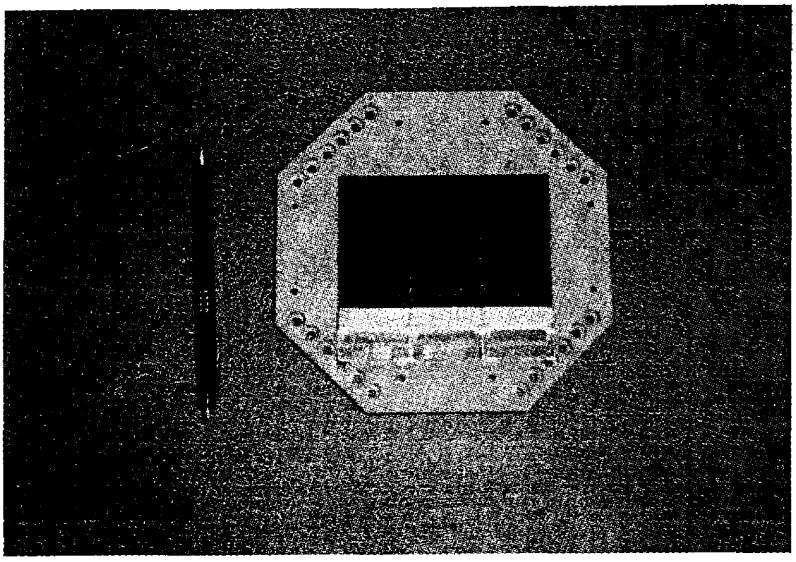

Figure 4.1: CCD chip, ST-002A.

3) means that the SITe CCD chips can be mounted very close to each other. This greatly facilitates the analysis of large images in comparison to the previous camera MOA-cam1(Sekiguchi et al 1992). With these advantages, the MOA-cam2 is expected to be more than 10 times more efficient than the MOA-cam1 for the detection of rare events.

Although the MOA-cam2 was made for microlensing survey, its quite high quantum efficiency and wide field of view are also useful to observe the weakly extended halo of the edge-on galaxy IC5249.

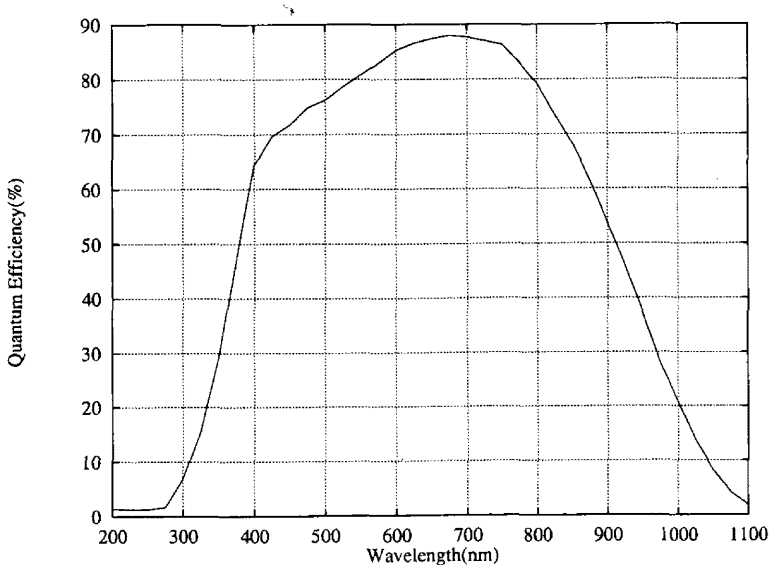

Figure 4.2: The quantum efficiency of ST-002A

4.1 The technical details of MOA-cam2

4.1.1 The CCD chip

We used the SITe CCD chip type ST-002A of SITe. This is a thinned, back-illuminated chip with 2048×4096 pixels of size $15 \times 15 \mu m$. It has three abuttable sides and special packaging to facilitate a close placement of arrays with minimal image loss in intergaps. The chip is a three phase, frame transfer device with a 100% optical fill factor, so the maximum area of the sensor is actively gathering the image. The device also features a buried channel for high transfer efficiency at low signal levels. The buried channel is made by growing another layer of highly doped n-type onto the existing p-type substrate to separate it from the insulating layer. Buried channels prevent charge trapping around electrodes. This is quite important when attempting to analyse weak images.

The chip incorporates multi-phase pinned(MPP) operation for low dark current and a lightly doped drain output MOSFET for low readout noise to

enhance the detection of weak images. The multi-phase pinned technology allows the ST-002A chip to be operated totally inverted during integration and line readout. This results in much lower dark current than conventional operation of a CCD. Other advantages of the MPP operation are the reduction of surface residual image effects and increase of quantum efficiency.

The thinned back-illuminated version is a unique SITe technology that provides a superior quantum efficiency over a wide range of wavelengths from near infrared to ultraviolet. The quantum efficiency(QE), measured by the manufacturer, is more than 80% around $550nm - 800nm$, 60% around $400nm$ and $900nm$, and 20% around $350nm$ and $1000nm$(Figure 4.2). Specifications of CCD chip ST-002A are given in Table 4.1.

Table 4.1: Specifications of ST-002A

format	frame-transfer, 4096 × 2048 pixels
pixel size	$15\mu m \times 15\mu m$
die size	$63.43mm \times 31.46mm$
MPP dark current(20C ref.)	$30pA/cm^2$
non-MPP dark current(20C ref.)	$100pA/cm^2$
readout noise	2-4 electrons,rms
parallel full well	100,000 electrons
serial full well	200,000 electrons
serial readout clock rate	$45KHz$
amplifier gain	$1.8\mu V/electron$
CTE	0.99995 at 500 electrons
	0.99999 at 5000 electrons

There is some distortion on the surface of CCD chips which has been measured by the 3-dimensional measurement machine in NAOJ, and its value turned

out to be about $90\mu m$ from peak to valley. This is about a half of the focal depth of our telescope against MOA-cam2. Here focal depth is the maximum permissible shift of CCD surfaces from focal plane of telescope. This is described as the product of ± 1 pixel size by the F-number of telescope. In our observation system, the focal depth is about $190\mu m(\pm 15\mu m \times 6.25)$. Using the techniques described in section 5.3.1, we installed the chips within the focal depth of the telescope.

4.1.2 The camera frame

The main camera frame is shown in Figure 4.3. It consists of the camera head and the liquid nitrogen tank. The dewar of the camera head is made of aluminium. Three flanges were prepared for the interior circuits, and hermetic connectors(41pin) were attached on three sides of the dewar(Figure 4.4). Another smaller hermetic connector(32pin) was attached for an interior temperature monitor and heater.

The three SITe CCD chips are mounted on a $120 \times 120 \times 10mm$ aluminium nitride(AlN) plate which has nearly the same thermal expansion rate as the die carrier of CCD chip(invar) with silver plated and vented screws. These screws have holes bored along their axes. They were used inside the dewar because they assist in evacuating the space between the screws and the screw holes. We designed the AlN plate for mounting the chips and ordered it from Mitsui Mine Material, Co. We required the flatness to be within $10\mu m$, to mount the chips within the focal depth of the telescope. We confirmed that the flatness of the AlN plate was about $9\mu m$. We did not glue the chips to the plate in case one needed to be replaced at a later date. Indium sheets were inserted between the CCD chips and the AlN plate to help the heat conduction. As mentioned

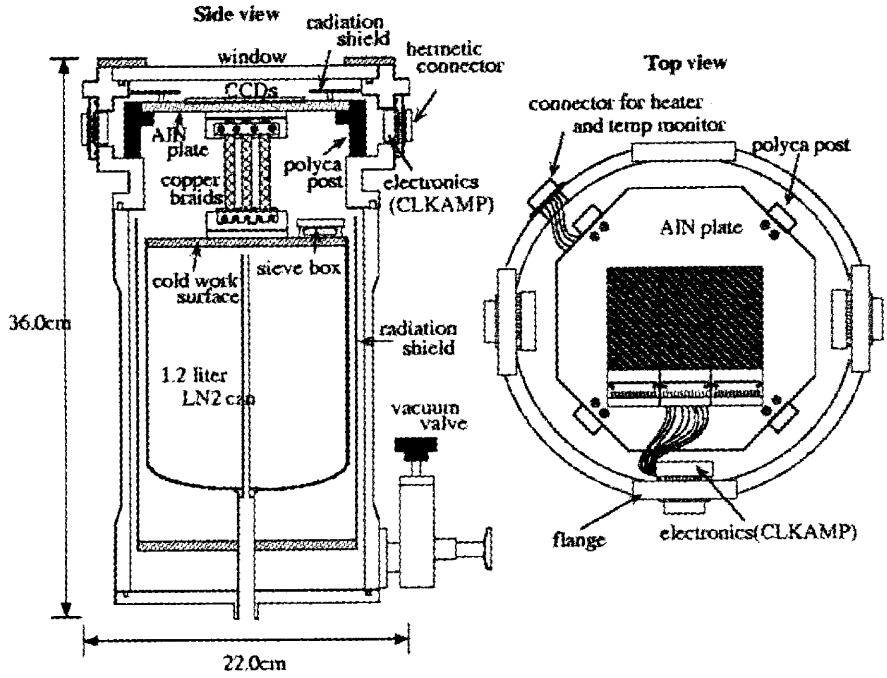

(a) The side view and the top view of the main camera frame

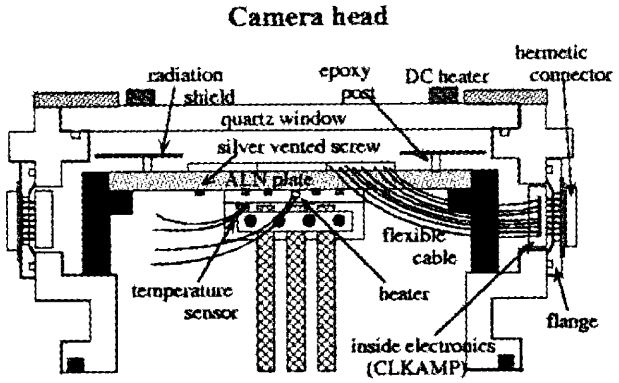

(b) The camera head

Figure 4.3: The detail of the main camera frame.

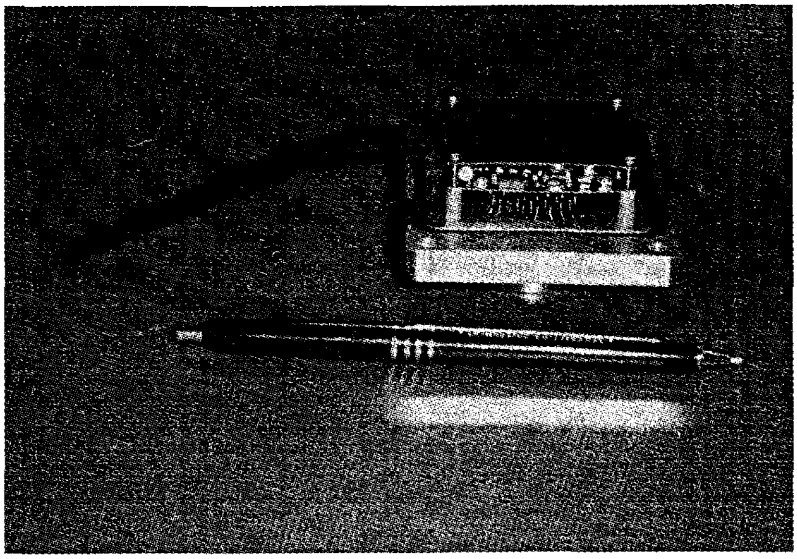

Figure 4.4: The circuit inside the camera(CLKAMP) and the 41 pin hermetic connector.

above, the SITe chip has three abuttable sides. We placed the three chips very carefully with $100\mu m$(about 7 pixels) dead space between them.

The AlN plate is supported by four polycarbonate posts, each about $5cm$ high and $2 \times 2cm$ square. We used polycarbonate because it provides relatively good thermal isolation $(0.1 - 0.2W/mK)$ and has a high Young's modulus($7 \times 10^4 kg/cm^2$). Polycarbonate is also easily processed. This assisted accurate positioning. In particular, the four polycarbonate posts were machined to the same height within $10\mu m$.

The dewar has a quartz window of diameter $20cm$ and thickness $15mm$. A light baffle/radiation shield is situated between the AlN plate and the quartz window. This masks the entire focal plane except the CCD chips. The shield is supported by four epoxy posts to insulate it from the AlN plate. This helps to reduce the consumption of liquid nitrogen. The surface of the baffle facing the incoming light beam is flat black to minimize stray light reflection, and the

surface facing the focal plane is gold-plated stainless to act as a radiation shield.

As described in 5.2.1, the circuit inside the camera(CLKAMP) is on a flexible printed board to minimize connection to the dewar. The 41 pin hermetic connector is soldered to the circuit through the flange. The circuit is supported by 4 epoxy posts on the flange(see Figure 4.4). As shown in Figure 4.3, the circuit is placed in a small space of the camera head. The flexible cable which is shown in Figure 4.4 is connected to the CCD chip. The circuit has two operational amplifiers each of which dissipate $1000mW$. The only connection to the cold part of the camera head is the flexible cable. This constrains the heat conduction from the operational amplifiers to the CCD chip. We have set a DC heater on the outside of the quartz window to keep moisture off.

We used a liquid nitrogen tank(ND5) manufactured by Infrared Laboratories because they are known to be reliable, and help to save time and simplify the fabrication. This tank contains a single cryogenic vessel with $1.2l$ capacity. We evacuate the camera to nearly $10^{-6}Torr$ to operate at very cold temperatures(about $-100°C$). A cooled radiation shield surrounds the vessel and the cold work surface(Figure 4.3).

The vacuum is enhanced by a molecular sieve getter which is mounted on the cold work surface. The cold work surface is connected to the AlN plate by three copper braids. Both ends of the copper braids are mounted to copper fixtures with screws and attached to the AlN plate and cold work surface with further screws. The number of copper braids was chosen to be sufficient to maintain the AlN plate at $-100°C$. The copper fixtures and screws enabled numerous tests to be carried out. A platinum resistor for temperature monitoring and a $1W$ resistance for heater were fixed to the copper fixture at the AlN plate. As described in section 5.2, the electronics of the camera(MFront) and the CCD

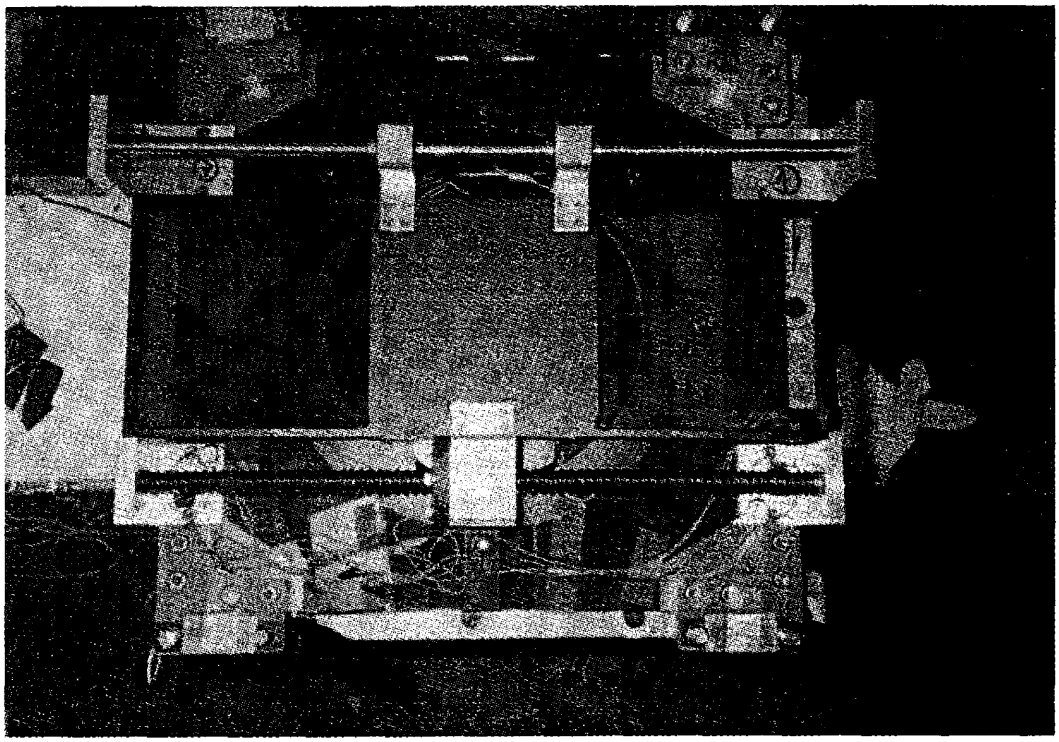

(a) The filter and shutter system

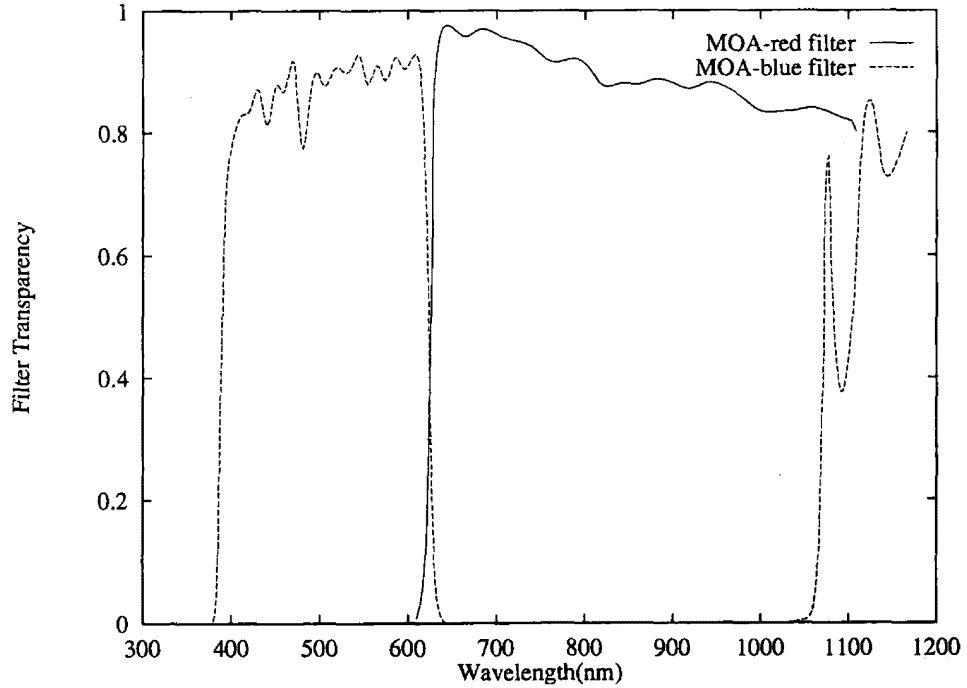

(b) The transmission of the filters

Figure 4.5: The filter and shutter system ,and the transmission of the filters.

controller(Messia3) control the CCD temperature. The liquid nitrogen holding time is more than 12 hours.

4.1.3 The filter and shutter system

Figure 4.5 shows the filter and shutter system, and the transmission of the filters as a function of the wavelength. The filters are $13cm \times 13cm$ square and $10mm$ thick. Their main purpose of using filters is to distinguish gravitational microlensing events from normal variable stars. Gravitational microlensing is achromatic, whereas most variable stars change colors. To compensate for the small aperture of the telescope, we chose wide passband filters rather than standard filters. As shown in Figure 4.5a, the shutter is located between the filters. The whole system slides sideways for observations in each color via a stepping motor which is controlled by the CCD controller Messia3(see section 5.2.2).

4.2 Electronics and CCD control

We used MFront(Mosaic CCD Front-end Electronics) for the electronics which was developed by the Subaru CCD development group. We use Messia3(modularized expandable system for image acquisition, Sekiguchi et al 1998) as the CCD controller and data acquisition system. Figure 4.6 shows the block diagram of MFront and Messia3.

4.2.1 MFront

MFront is a set of front-end electronics for mosaic CCD cameras that is designed for 2K×4K chips such as MITL, SITe, EEV and Hamamatsu and works with any type of CCD controller. It enables the construction of a camera with any number of chips. MFront consists of four electronics boards:

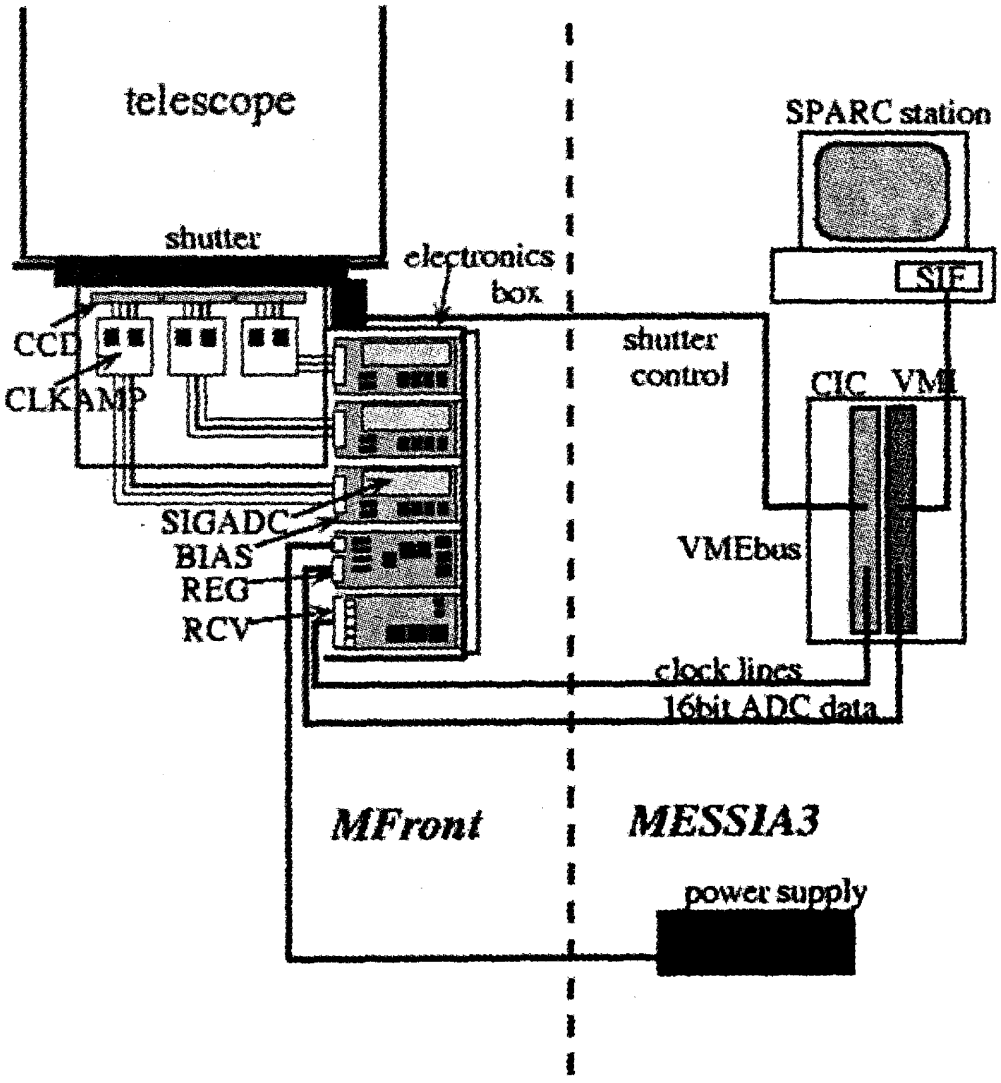

Figure 4.6: The block diagram of MFront and Messia3.

1) Clock-driver/pre-amplifier board(CLKAMP),

2) Bias board(BIAS),

3) High-speed signal/ADC board(SIGADC),

4) Power Regulator/Bus-receiver(REGRCV).

CLKAMP is installed in the dewar of the camera head and has two operational amplifiers(BURR-BROWN OPA627) for the two output signals from the SITe chips, and four analog switchs(TEMIC DG403) which provide eight clock-lines to the CCD chip. CLKAMP is built as a flexible printed circuit in order to minimize connections in a dewar(see Figure 4.4). The size of the circuit is about $4cm$ square by $1cm$ thick.

BIAS is designed as a standard 3U Eurocard with a 96 pin DIN connector for easy system integration(Figure 4.7). This board uses EEPROM-based 8bit-DACs(ASAHI KASEI AK9813) to generate 32 programmable voltages. All voltages(for biases and clocks) which are generated on this board can be monitored by an on-board 12bit ADC(ANALOG DEVICES AD7876). On this board there is a temperature monitor for the platinum resistor and the control signal for the heater driver is provided. All voltages on this board and temperatures of the CCD chips are controlled from Messia3.

SIGADC cosists of a classical dual-slope correlated sampling(DSCS) circuit and an analogic 500kHz 16bit ADC (Analogic ADC4325). The size of this board is about $4.5cm \times 13.0cm$. Two SIGADC boards can be mounted on a

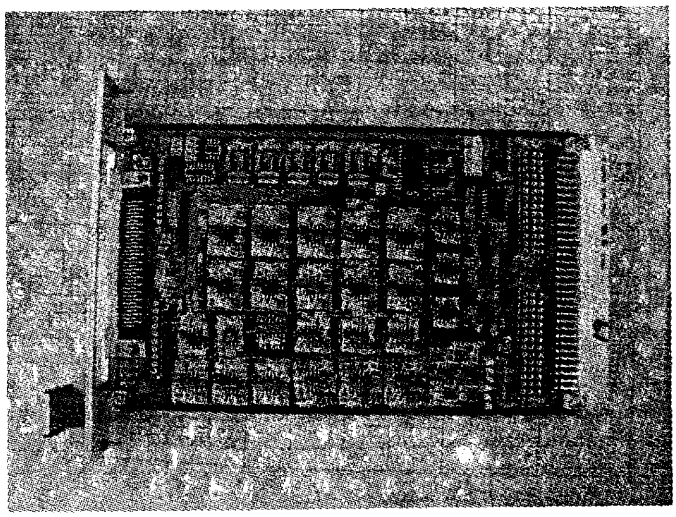

Figure 4.7: BIAS board

BIAS board.

REGRCV consists of two boards, i.e. REG and RCV. Both are designed as standard 3U Eurocards and have 96 pin DIN connectors. The REG board regulates incoming DC voltages and supplies clean voltages to other boards of MFront. The REG board has RS485 drivers to send ADC data. The RCV board includes high speed photocouplers to receive the digital control signals from the CCD controller. These photocouplers prevent outside noise entering the camera electronics and damage to the CCD chips. We also use the photocouplers in one module of the Messia3(VMI) to get digital data from the REG board. There is no electronic connection between MFront and Messia3. The ground of each board of MFront is connected to the power supply ground.

Five boards, the three BIAS boards with the SIGADC board, the REG board and the RCV board are inserted in the electronics box(see Figure 4.6). This is a manufactured rack with height for a 3U Eurocard and back plane for a 96 pin DIN connector. We wire-rapped the back plane for our system. Almost CCD clock lines and voltage lines from the REG board and the RCV board are

in parallel, so wire-rapping is not complicated. As shown in Figure 4.6, we use one set of CLKAMP, BIAS and SIGADC circuits for each CCD chip. With this configuration, the CCD chips of the mosaic are completely isolated from one another, except for having a common ground. This strongly reduces the risks of interchip crosstalk and noise injection. The system can read the outputs of the three CCD chips simultaneously. MFront is the standard front-end electronics for the mosaic CCD camera at the Subaru telescope. The details of MFront are described on the web site(http://www.mfront.com/).

4.2.2 Messia3

For the CCD control and data acquisition system, we use a system called modularized expandable system for image acquisition 3(Messia3), which was developed at NAOJ as a prototype CCD controller for the Subaru telescope. Messia3 is based on VMEbus, and was designed not only for single-chip CCD cameras but also for mosaic CCD cameras. As shown in Figure 4.6, Messia3 consists of three boards:

1) SIF(Sbus Inter Face),

2) VMI(VME and Memory Interface),

3) CIC(CCD and Instrument Controller).

The SIF is a Sbus card of the SPARC station. It communicates with the VME and transfers the data from the VME to the SPARC station by fibre channel. The VMI takes charge of the communication with the SIF from the VME side. The VMI is a master on the VME and can read and write on the CIC board. The memory of 64Mbyte can be installed on the VMI. The CIC can generate 32

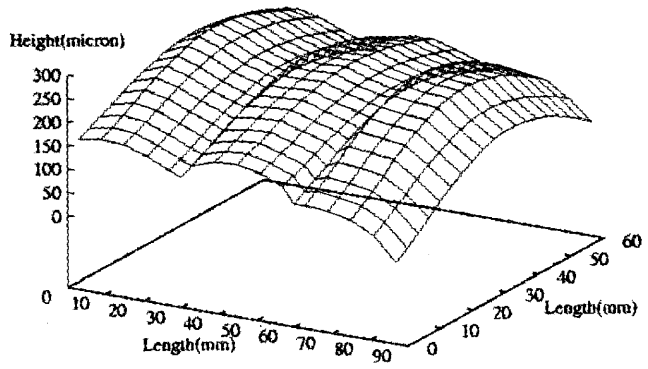

Figure 4.8: The flatness of ST-002A(for three chips).

CCD clocks under DSP(Digital Signal Processor) control and has 16bit digital input and output for real time control of other devices.

Software for Messia3 is supplied from ftp site messia.mtk.nao.ac.jp(133.40.203.95). This software should be installed in the host machine, SPARC station. Before installation of software for Messia3, gcc and Tcl/Tk must be installed. The C compiler for DSP is also needed because Messia3 uses DSP. Gcc is used for compilation of software for Messia3. Tcl/Tk is the basic software for Messia3 and is useful for on-line control of astronomical observations.

4.3 The performance

4.3.1 The flatness

As described in section 5.1.1, the ST-002A SITe chip has a rise around the middle of the chip surface. Figure 4.8 shows the flatness of our chips which

was measured with a laser measurement machine relative to the plane at which the camera is mounted to the telescope. The three bumps correspond to each chip. It is apparent that all three chips are inclined relative to the mounting plane. To adjust the inclination, we inserted aluminium spacers of appropriate thicknesses at three corners of the plane. The size of the mounting plate is about $30cm \times 30cm$, and the thickness of the thickest spacer was about $1.0mm$. With this adjustment, the entire CCD surfaces became optically planar and aligned to within $100\mu m$. We checked the seeing with stars in various positions in several images that were taken toward the Galactic center and the LMC. We found that the seeing varied by less than one pixel over entire image plane, confirming the flatness of the surface within the focal depth($190\mu m$) of the telescope.

4.3.2 Readout noise, readout time and gain

To realize our observational goal, we need low readout noise. We noticed that the readout noise increased suddenly beyond a readout speed of 120KHz, and the noise around that frequency was very sensitive to a small clock timing difference. We determined the best clock timing with low readout noise and high readout speed by trial and error. We obtained a readout noise of around 6 electrons at a readout speed of 133KHz. At this speed, about 60 seconds are needed to read out the data on a CCD chip. As stated in section 5.2.1, MFront reads out the three chips simultaneously. The gain of the CCD chips obtained from standard deviation of ADUs in a uniformly exposed image was 2.7 electrons/ADU.

4.3.3 Test image

As a demonstration of our camera, we took images of the Galactic Bulge region using 3 minutes exposure time. A typical image is shown in Figure 4.9.

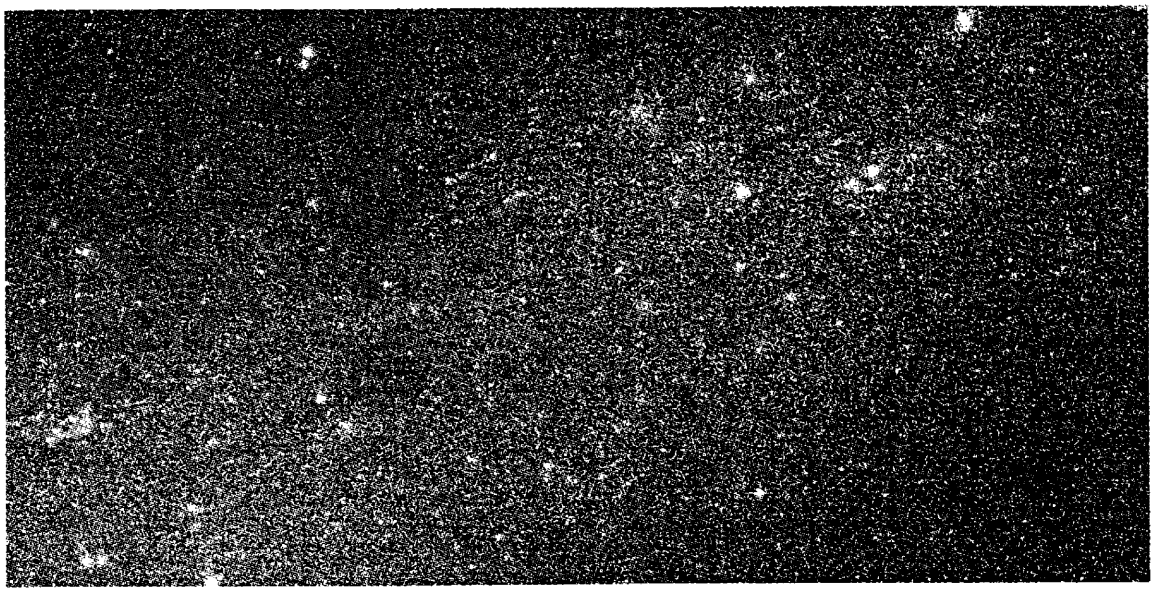

Figure 4.9: The test image taken toward the Glactic Bulge region.

To show the quality of the raw data, only naive sky subtraction was done for this image. Also, no flat fielding correction was made. In this region($0.92° \times 1.39°$), we found three hundred thousand star images.

4.4 Observation system

The observing site is the Mt John University Observatory in New Zealand at $170°27.9'E$, $43°59.2'S$, $1030m$ altitude. Typical sky background values are 21.9, 22.6, 21.5, 20.9 and 19.1 magnitudes per square arc second in the U, B, V, Rc and Ic passbands respectively at an air mass of 1.0, and 21.7, 22.1, 20.8, 20.3 and 18.6 at an air mass of 2.7(Gilmore 1994). Spectroscopic hours at Mt John are approximately 45% of total available observing time, and the seeing is typically in the range 1.0-2.5 arc seconds. The global seeing of the entire set-up is typically 2.0-3.5 arc seconds.

In Figure 4.10, our observation system is shown. The telescope is a stan-

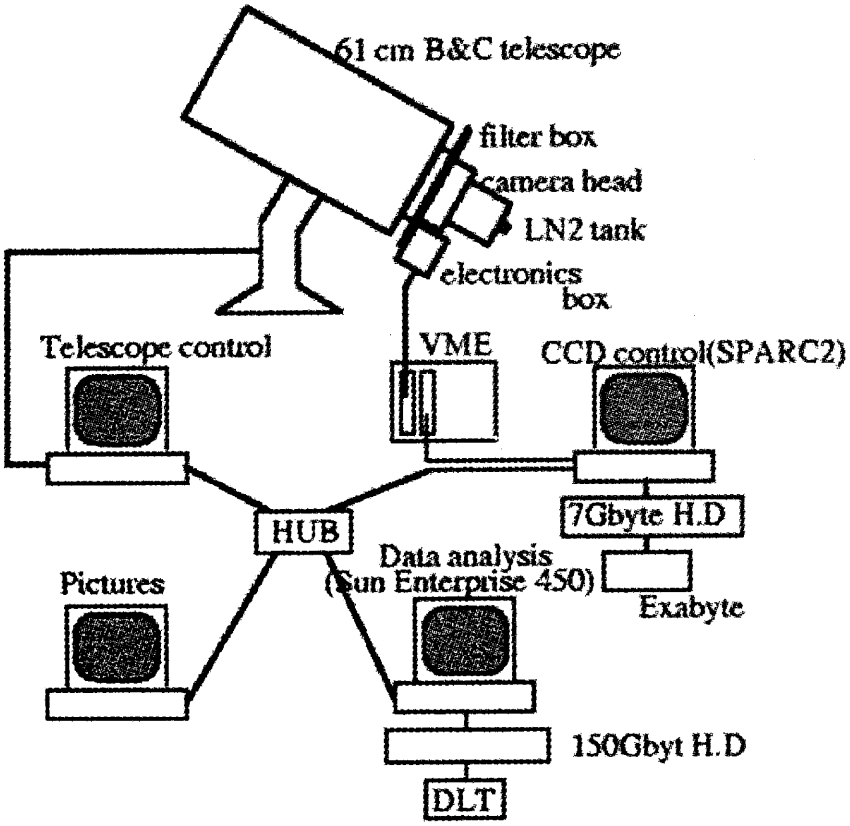

Figure 4.10: The observation system of MOA.

dard Boller and Chivens 61cm aperture Ritchey-Chretien Cassegrain reflector. It has been modified to operate semi-automatically by replacement of the original AC motors with microstepper motors operating under 'TELJOY'(Williams 1996). It was working at F/13.5 and later updated to a F/6.25 system, by means of a new spherical secondary mirror and a three lens field corrector added to the original hyperboloid primary mirror to provide a flat diffraction limited field of 85mm diameter. It was also found that this field could be extended with some vignetting but without image degradation for the larger field requirement of the MOA-cam2 system(Pennycook 1998). The CCD controller, Messia3, which is responsible for all operations of the camera(clock sending, readout, temperature monitoring and shutter movement) is managed by a SPARC station 2. A 7 Gbyte hard disk and an 8mm Exabyte device are connected for data archival to this machine. Another PC is included for on-line image monitoring and analysis during observations. The image reduction and analysis facility(IRAF) is installed on this PC. Moreover, another PC for telescope control and a Sun workstation with four cpus (Sun Enterprise 450) for real-time analysis are installed. All the machines are connected with a switching hub for communication with one another. The telescope and the camera are both controlled by the SPARC station 2, so we can survey many targets almost automatically. Table 4.2 summarizes the specification of MOA-cam2.

Table 4.2: Specifications of MOA-cam2

CCD chip	Scientific Imaging Technologies ST-002A
array size	$1 \times 3(4096 \times 6144 pixels)$
pixel size	$15\mu m \times 15\mu m$
dead space	$100\mu m$(7 pixels)
effective area	$61.44mm \times 92.16mm$
pixel scale	$0.81 arcsec$ with B &C telescope
effective coverage	$0.92° \times 1.39°$
filter	blue$(400 - 630nm)$ & red$(630 - 1100nm)$
mounting plate	aluminium nitride:AlN $12cm \times 12cm \times 10mm$
LN_2 tank	Infrared Laboratories ND5$(1.2l)$
LN_2 holding time	12.5 hours
operating temp	$-100°C$
window	$20cm$ diameter,$15mm$ thick quartz
weight	$40kg$

Chapter 5

Observation, Data analysis and Results

In this chapter, the detail of the observations of IC5249, the method of the data analysis and our results are presented.

5.1 Observation

The photometry of IC5249 was done on photometric nights between 1998 August and November. The MOA-cam2 was installed in the 61 cm Boller and Chivens telescope for the observation. Only the middle chip of three CCD chips in the MOA-cam2 was used for the photometry of IC5249. Both filters, MOA-red and MOA-blue were used (see Figure 4.5).

Three regions(A, B, C) were determined on the middle chip, and IC5249 was observed in these three regions by turns(see Figure 5.1). This process was carried out many times cyclically to minimize the effects of changing the air mass. In each cycle, the position of IC5249 was shifted about 100 pixels(80″) to ensure that the target was not observed in the same position of the chip. Exposures were carried out for two cases ,i.e, 3 minutes and 10 minutes. The long exposure time makes images with a good signal-to-noise ratio and reduced dead time(i.e. non-usable time, due to the reading out CCD signals and the data storage time). However, poor tracking and atmospheric turbulence may cause a bad shape of a star. On the other hand, the short exposure time

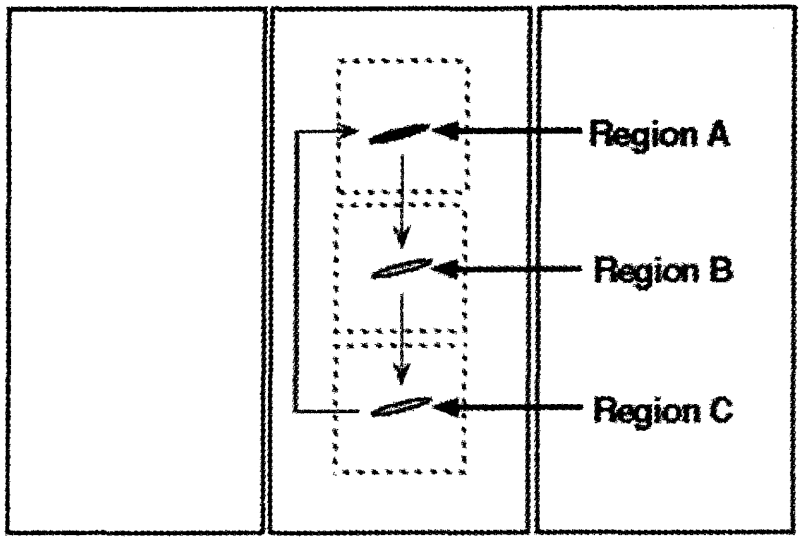

Figure 5.1: The observation method for IC5249.

can get a good shape of a star, but increases the dead time. By taking many images for two different exposure times and adding them, one can get good final images efficiently. Dark frames were taken every one process(three exposures for IC5249 in A, B and C region on the CCD chip) because the amount of dark current changed with the temperature. The procedure of the observation in 10 minutes exposure is shown in Figure 5.2. 33 images were obtained for 10 minute exposures and 36 images for 3 minute exposures using the MOA-red filter. In addition, 51 images were obtained for 10 minute exposures and 57 images for 3 minute exposures using the MOA-blue filter.

5.2 First data analysis

The procedure for the first data analysis is shown in Figure 5.3. IRAF(Tody 1986) was used for the first data analysis. IRAF(Image Reduction and Analysis Facility) was developed at NOAO(National Optical Astronomy Observatories

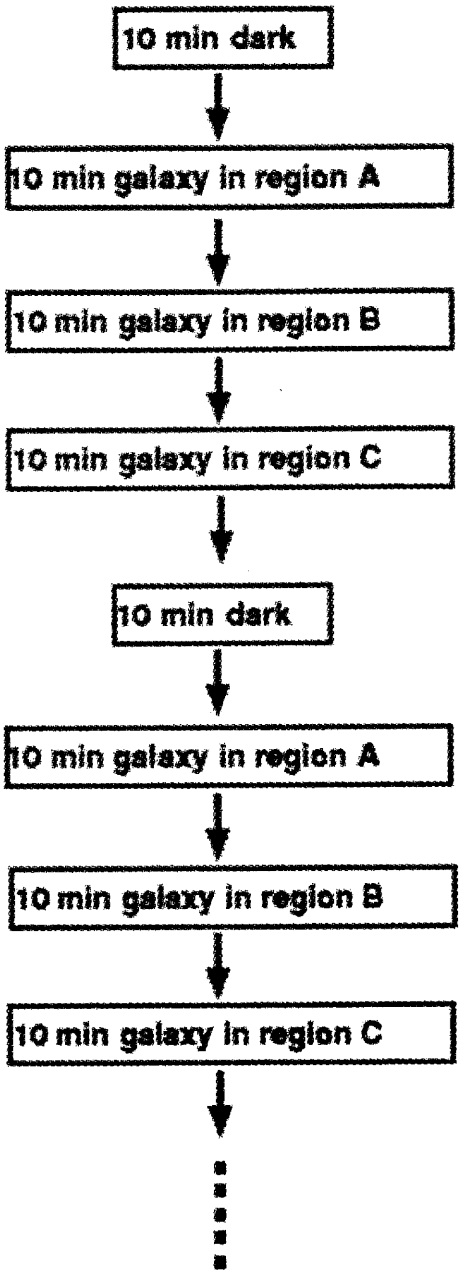

Figure 5.2: The procedure of the observation in 10 minutes exposure.

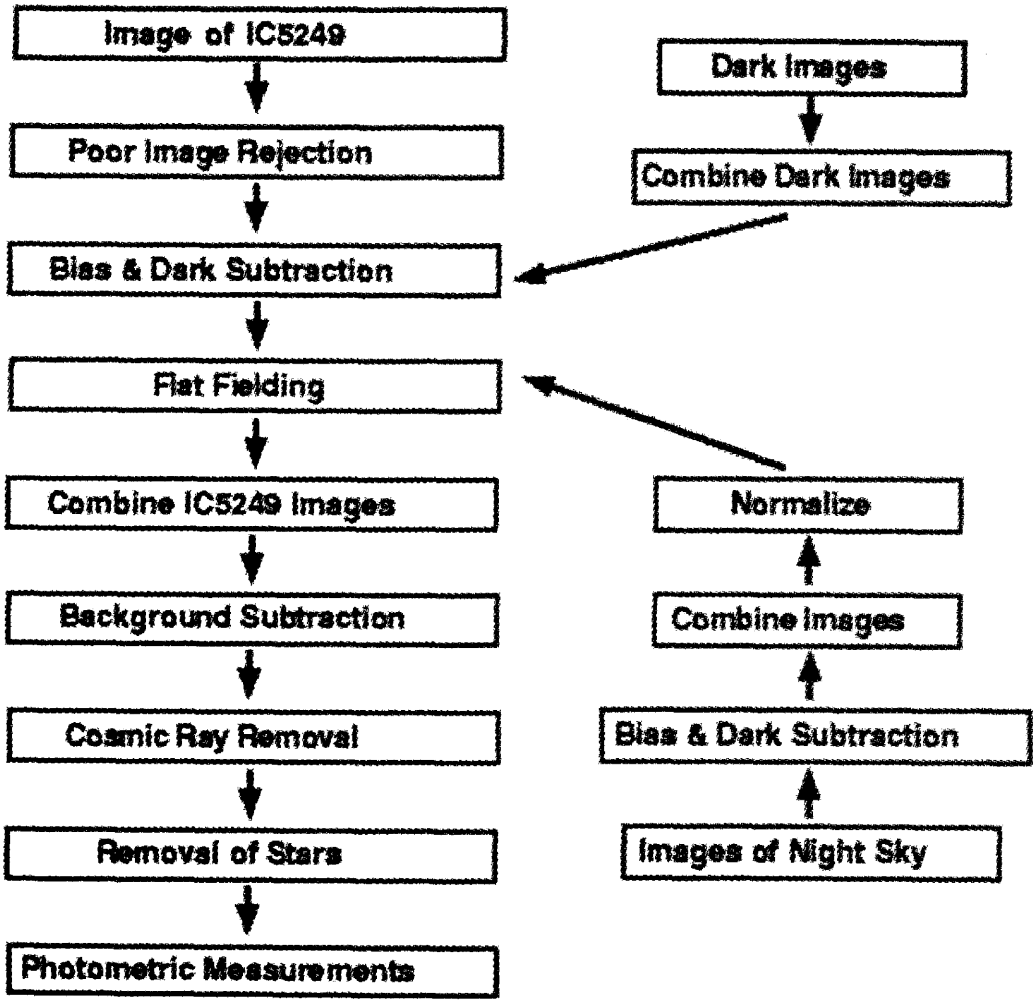

Figure 5.3: The procedure of the first data analysis.

in Tucson, Arizona) as software for the analysis of astronomical images at various wavelengths. Whole images of IC5249 were checked with IRAF command "imexamine" and bad images, in which poor tracking caused trailed star shape or seeing exceeded over 4″, were excluded. As a result, 27 images at 10 minute exposures and 26 images at 3 minute exposures were used for the actual data analysis in the images of the MOA-red filter. In the images of the MOA-blue filter, 39 images at 10 minute exposures and 53 images at 3 minute exposures were used.

The final dark image, which was subtracted from one raw image, was prepared by taking median value of more than three dark images in order to prevent image degeneracy by cosmic rays. Dark images taken at near the time when the image was taken were used. The IRAF command "imcombine" was used when the median value of many dark images was taken. The final dark image for each raw image of IC5249 was subtracted with IRAF command "imarith".

Flat field images are needed to correct the differences of the quantum efficiency between each pixel. The process of making up the flat field images is as follows. There are three types of flat field images. One is called "dome flat" which is made by taking screen inside the telescope dome. A weak light is projected to the screen. The other is called "sky flat" which is made by taking the twilight sky. The final one is "dark flat" which is made by taking night sky. Each flat field image has advantage and disadvantage. In "dome flat" and "sky flat", light to the CCD chips is not uniform. In "dark flat", stars are left and light level is quite low. In order to get extremely weak light from the outer region of IC5249, accurate flat field images were needed. For this purpose, the "dark flat" was used because light on CCD chips is most uniform among three flat fields.

IC5249 was taken in one of the three regions(A, B, C) of the CCD chip, and the remaining two images were used for "dark flat". Three regions(A, B, C) with the size of 900 × 900 pixels were cut off from whole images (I call these small images sub-images). The IRAF command "imcopy" was used to cut off sub-images from the original images. Whole sub-images, in which IC5249 was not involved, were prepared to make up a "dark flat" for each region. One image of "dark flat" contains many stars, because night sky was taken for it. When the target galaxy IC5249 was taken by the CCD camera, a shift of the telescope of 80″(100 pixels) was made between each cycle. Therefore, each star did not appear at the same position on the CCD chip(see section 5.1). Stars disappeared by means of taking the median values of many images of "dark flat". Many images of "dark flat" overcame the disadvantage that light level was quite low. One had to be careful to use whole sub-images where IC5249 was not involved. When IC5249 is near one sub-image, that sub-image might be contaminated by the leakage of light from IC5249. I chose three regions(A,B,C) as near as possible to each other to avoid the change of sky level in a wide surface of the CCD chip. As a result, if IC5249 was observed on upper part of region B, light from the halo of IC5249 might fall onto the lower part of region A. If IC5249 was observed outside of sub-image within a size of 250 pixels, that sub-image was excluded in the following process to avoid the phenomenon of light leakage from the halo of IC5249(see Figure 5.4). The number of sub-images, which were used to make up final "dark flat" images of each filter (MOA-red and MOA-blue) and each exposure time(10 minutes and 3 minutes), are shown in Table 5.1. The reason why sub-images of region B is less than that of regions A and C is that sub-images of region B, which were contaminated by light leakage of IC5249 of regions A and C, were excluded.

It is clear that the median value of each sub-image is changeable which means that the sky level was fluctuating during the observation period. In particular,

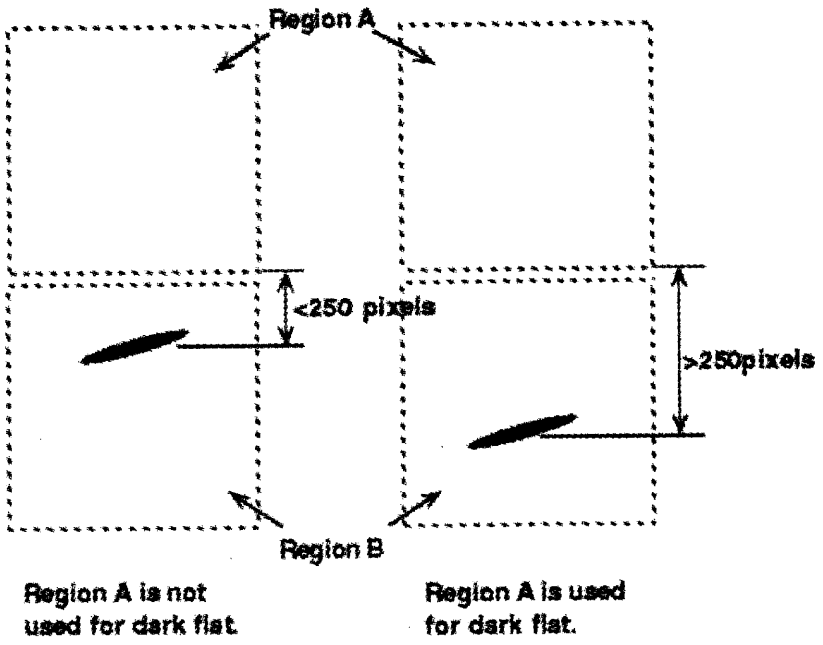

Figure 5.4: The sub-iamge for flat field construction.

this was remarkable for the MOA-red filter. Fluctuations of the value for 10 minute exposure time was about $\pm 25\%$ while for the MOA-blue filter, it was about $\pm 5\%$.

The first step to make up the final "dark flat" image is to normalize whole sub-images using their median values. The next step is to decide the median values of the same pixels in whole sub-images. At this time, the pixels whose values exceeded 8 times the normalized sky fluctuation(which corresponds to 30 ADU for 10 minutes exposure time in the MOA-red filter and 11 ADU in the MOA-blue filter) were ignored. Central regions of bright stars were excluded with this method. Outer regions of bright stars and dark stars were excluded with the σ-clipping method. The *sigma*-clipping method works as follows. At first, the median values of the same pixels and their standard deviations were calculated. Next, the pixels whose values exceeded 3 times the standard

Table 5.1: The number of sub-images that were used to make up flat field images

Filter	Exposure time(minutes)	Region	Number of frames
MOA blue	10	A	17
"	"	B	14
"	"	C	18
"	3	A	19
"	"	B	17
"	"	C	20
MOA red	10	A	19
"	"	B	16
"	"	C	19
"	3	A	21
"	"	B	18
"	"	C	21

deviation were excluded. Then the median value and the standard deviation were recalculated. This process was continued until whole values of the pixels were settled less than 3 times of the standard deviation. The σ-clipping method was applied to whole pixels of three regions. Finally, the value of each pixel of final image was divided by the median value of whole pixels of the region to normalize the median value to 1.0. Final flat field images are shown in Figure 5.5. All processes to create flat field images were carried out with the IRAF command "imcombine".

After flat field corrections for whole sub-images of IC5249, cosmic ray traces in the images were removed by the IRAF command "cosmicrays". Cosmic ray traces, whose ADU values were too low to be removed with "cosmicrays", were removed with the IRAF command "imedit". Then, all images were combined with "imcombine". At that time, 5 stars near IC5249 were used in order to shift

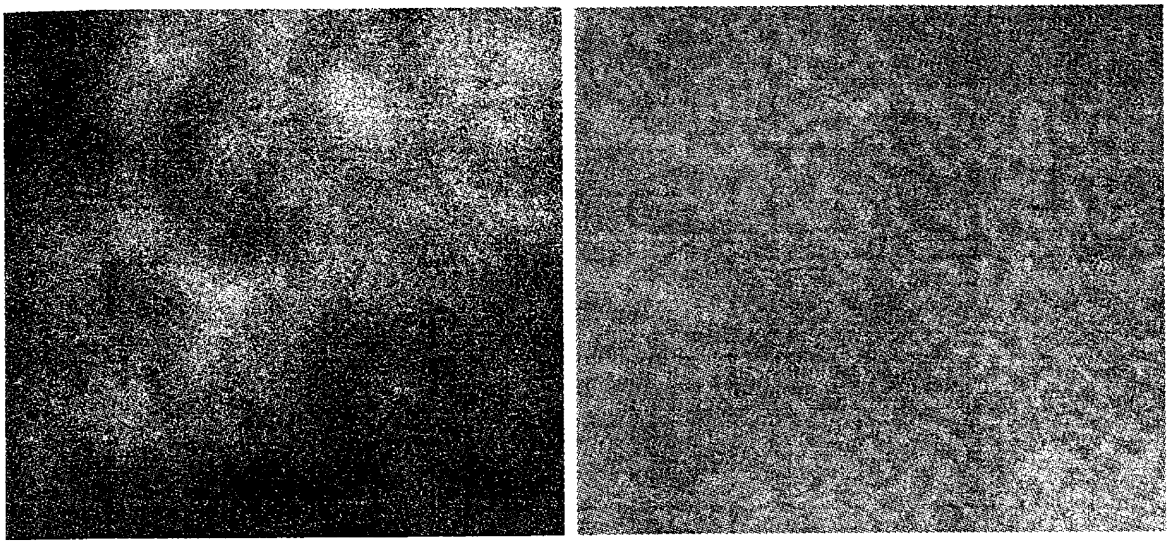

(a) MOA-blue filter (b) MOA-red filter

Figure 5.5: The flat field images

and rotate the images by "imcopy" and "rotate" for matching the positions of IC5249. Total exposure times were 5 hours 48 minutes for the MOA-red filter and 9 hours 9 minutes for the MOA-blue filter. Both final images are shown in Figure 5.6. Seeings of final images are 2.9″ in the MOA-red filter and 3.6″ in the MOA-blue filter. IRAF commands, which were used in the first data analysis, and their properties are summarized in Table 5.2.

5.3 Calibration

Photometoric measurements by the MOA-red and the MOA-blue filters with the SITe CCD chip are nearly equivalent to those of the I and V pass-bands, respectively (see Chapter 4). Five uncrowed stars near IC5249 with V magnitudes in the range of 12-15 magnitude and colors $0.8 \leq$ B-V ≤ 1.8 were used to convert our filter system to the standard V and I systems. They are

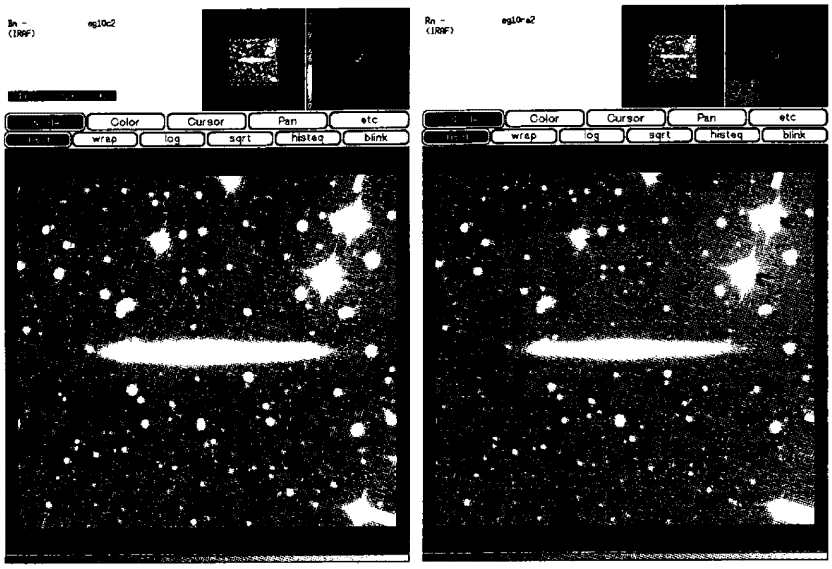

(a) MOA-blue filter(9 hours 9 minutes)

(b) MOA-red filter(5 hours 48 minutes)

Figure 5.6: The final images.

Figure 5.7: The stars used for the calibration

Table 5.2: IRAF commands which were used in first data analysis and their faculties

IRAF command name	properties
imexamine	calculates statistical values(average, median, max, minimum and so on).
imcombine	combines many images.
imarith	adds, subtracts, divides and multiplies images.
imcopy	copies images and cuts off specified regions of images.
cosmicrays	removes cosmic ray features with various parameters.
imedit	revises small ADU variations in images.
rotate	rotates images around specified points in images.
daophot	does photometry of stars in images.

shown in Figure 5.7. Photometric measurements of these stars in the B, V, Rc and Ic passbands were carried out using the 60 cm Optical Craftman Telescope at MJUO on August 19 1999. Comparing the results of these photometric measurements with the magnitudes of these stars in several sub-images was found to satisfy the relationships as follows.

$$m_{Ic} = m_{MOA-red} + 0.86 \tag{5.1}$$

$$m_V = m_{MOA-blue} + 1.33 \tag{5.2}$$

The magnitudes of the five stars in several sub-images were measured by IRAF command "daophot". Here m_{Ic} and m_V denote the Ic magnitude and the V magnitude, respectively. $m_{MOA-red}$ and $m_{MOA-blue}$ denote the output magnitudes after "daophot" photometry of sub-images in the MOA-red and the MOA-blue filters, respectively. The accuracies of these two relationships are about ± 0.09 magnitude in m_{Ic}, and ± 0.22 magnitude in m_V, respectively. In terms of the surface brightness, equations (5.1) and (5.2) imply that 1ADU/pixel corresponds to $\mu_{Ic} = 25.40 mag/arcsec^2$ for a 10 minute exposure by the MOA-red filter and $\mu_V = 25.87 mag/arcsec^2$ by the MOA-blue filter, respectively.

5.4 Scattered Light

The atmospheric turbulence and the scattered light in a telescope, especially at optical surfaces close to the focal plane, may produce an extended light profile surrounding a bright object and contaminate results. This effect was pointed out and its magnitude was measured by other groups (Morrison et al 1994; Sackett et al 1994; Lequeux et al 1996). I estimated the magnitude of this effect using a technique similar to those used by other groups. At first, an accurate point spread function(PSF) was determined for the final image of the MOA-blue filter(Figure 5.6b) whose seeing was worse than that of the MOA-red filter. I found the shape of the PSF was more spread for brighter stars. Images of nine stars, whose intensities were nearly equal to the central value of IC5249(about 580ADU), were cut off from the final image with the size of 60 $\times$ 60 pixels(48.6$''$ $\times$ 48.6$''$). These stars were combined by the median value after scaling the intensity. This produced an unsaturated image of a bright star that was free from cosmic rays and surrounding stars, from which the PSF was accurately determined. The star image produced and its radial profile in ADU are shown in Figures 5.8 and 5.9, respectively. One can see that the influence of star light around 10$''$ - 30$''$ from the center whose ADU value is about one ten thousandth of the central one.

Next, the bright region of IC5249 in the final image was convolved with the PSF and compared with observed data. The convolution was meant to degenerate the real data through some filter functions (in this case, filter function is the PSF.). The observed data were a result of the passage through filter functions which are the scattering of light in a telescope and the atmospheric turbulence. Therefore, they were not real data. I chose the region from the final image inside $\pm$ 1 kpc from the galactic plane as the bright region of IC5249. Results are shown in Figure 5.10. The distance from the galactic plane is shown along the horizontal axis in units of pixel. The surface brightness of IC5249 is shown

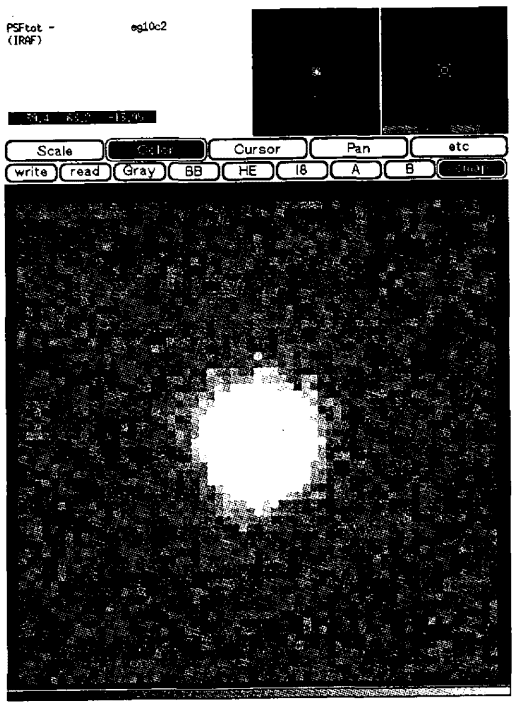

Figure 5.8: Point Spread Function of the final image

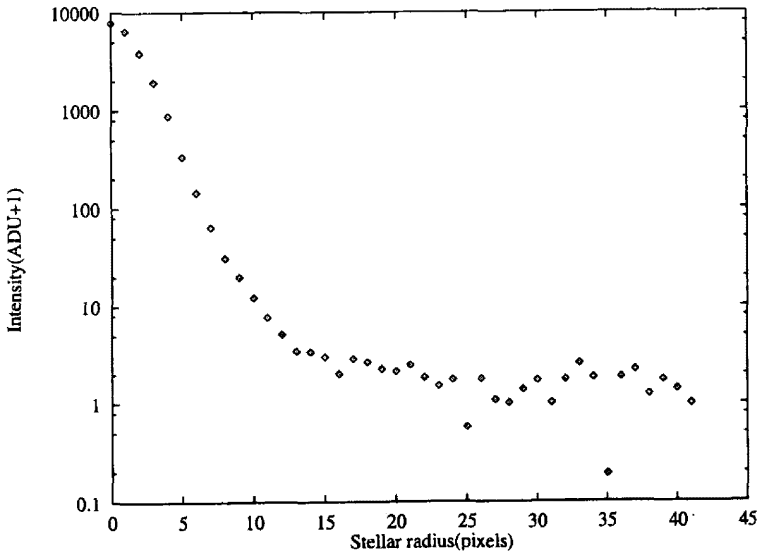

Figure 5.9: Radial profile of the brightness of the Point Spread Function. The horizontal axis shows the distance from the center of the star in pixel, and the vertical axis shows the brightness in ADU.

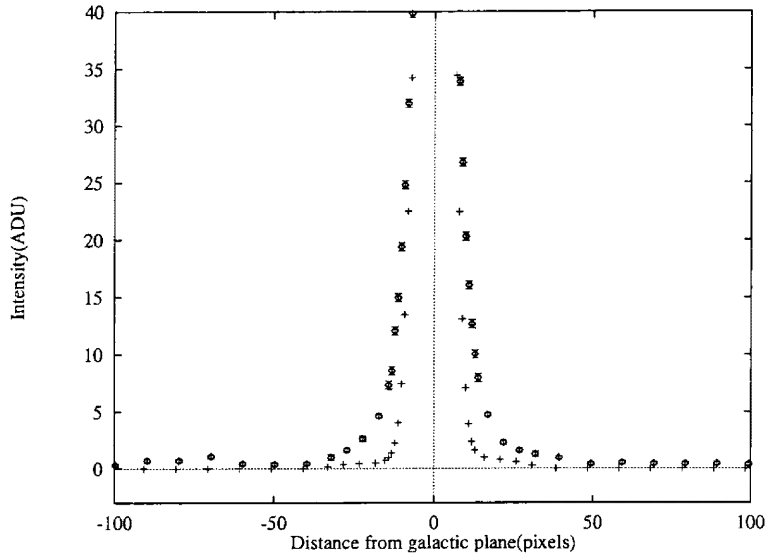

Figure 5.10: The observation data of IC5249 and the result of the convolution. Diamonds with error bars show the observation data of IC5249. Crosses show the convolved data of ± 1kpc region from galactic plane with Point Spread Function.

along the vertical axis in units of the ADU. Diamonds with error bars represent the observed data and crosses indicate the convolved data of the bright region with the PSF, respectively. It is obvious that the observed data are spread more widely than the convolved data. It means that scattered light, either in the telescope or in the atmosphere, does not cause an extended light profile around IC5249.

5.5 Masking

Light from foreground stars prevents accurate photometry of IC5249. Stars in the final image were searched with the IRAF command "daophot" and masked out to a radius where the intensity of star dropped down to 1.8 times the sky fluctuation(2.5ADU in the final image of the MOA-red filter and 1.1ADU in that of the MOA-blue filter, respectively). There were many dark star features

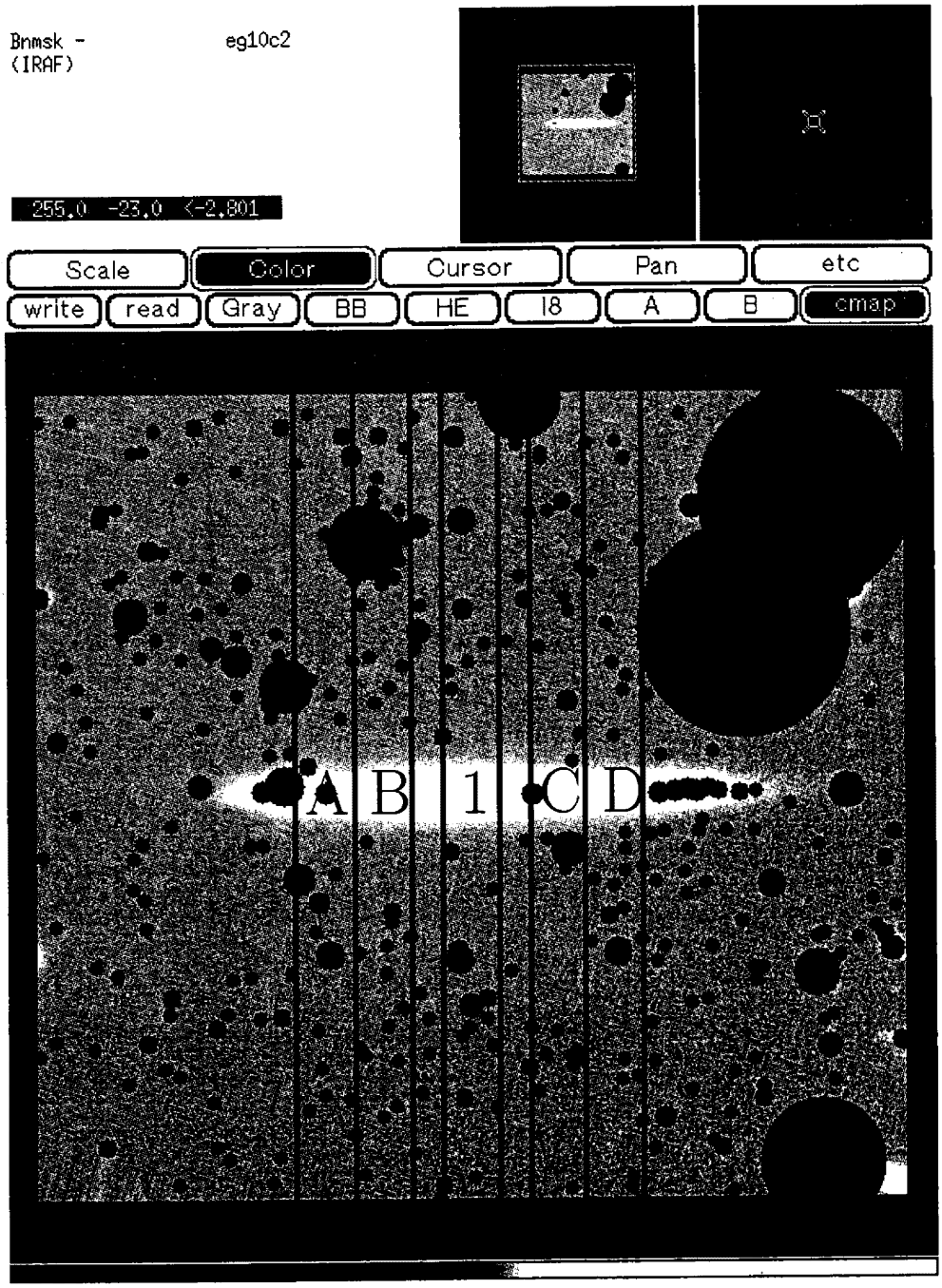

Figure 5.11: The final image of MOA-blue filter after masking of stars. Four regions labeled A, B, C and D were used for the fitting the observation data to various models.

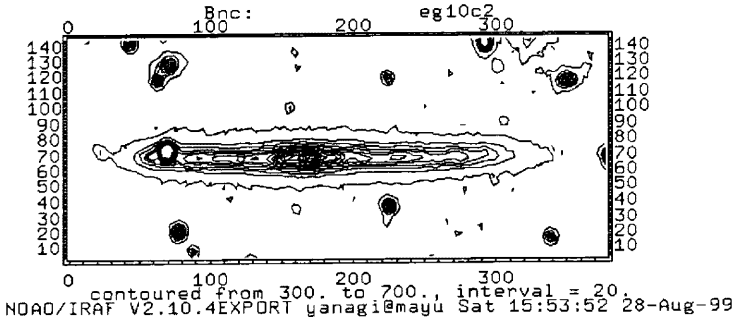

(a) MOA-blue filter

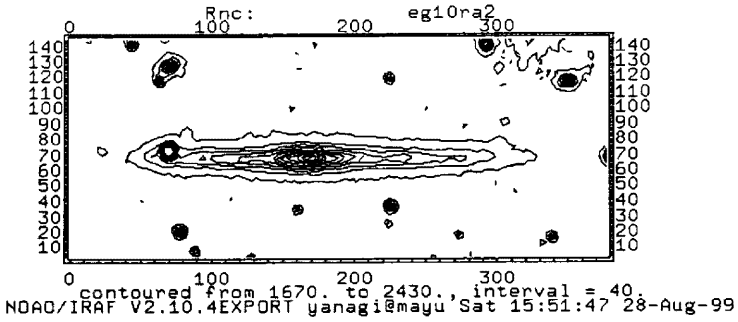

(b) MOA-red filter

Figure 5.12: The contour of the final image.

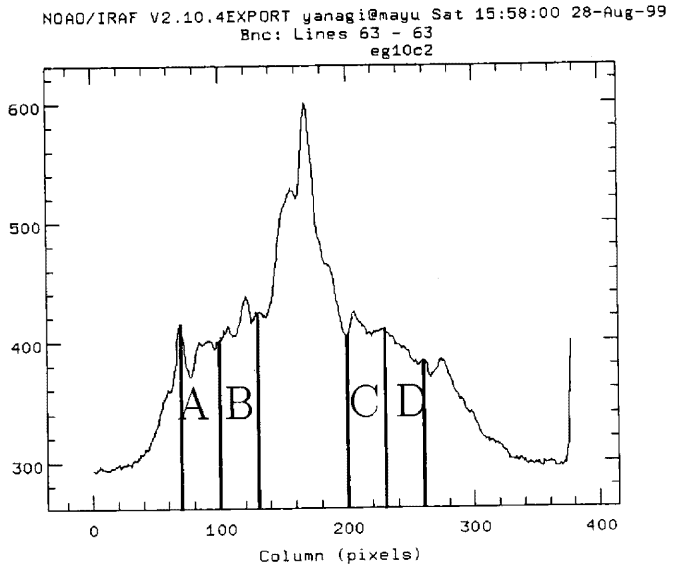

Figure 5.13: The brightness profile of IC5249 at the galactic plane. The horizontal axis shows the distance along the galactic plane in pixel, and the vertical axis shows the brightness of IC5249 in ADU. Four regions labeled A, B, C and D were used for the fitting the observation data to various models.

that were not identified with "daophot". These features were masked out with round pattern for the darkest star in the search of "daophot". The final image of the MOA-blue filter in which whole stars were masked out is shown in Figure 5.11.

5.6 Photometry of IC5249

Contour plots of the final images of IC5249 in both the MOA-red and the MOA-blue filters are shown in Figure 5.12. These may be compared with the H_I distribution displayed in Figure 3.1. There is no evidence for flaring and warping in either contour. In what follows, I shall assume the Hubble constant equal to $65 kms^{-1}Mpc^{-1}$. This corresponds to a distance of 36 Mpc for IC5249 and a pixel size on the sky of 0.144kpc at IC5249, because the recession velocity of IC5249 is $2340 km/s$(see Chapter 3).

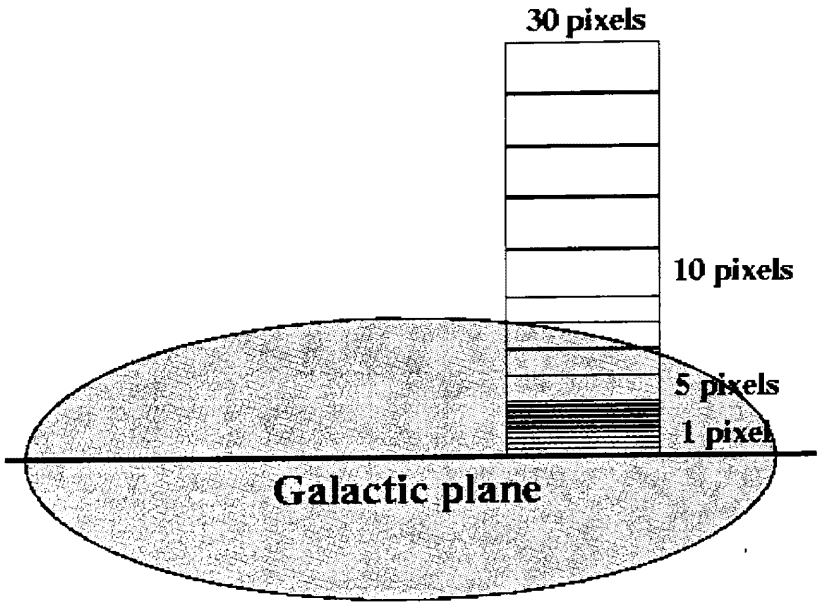

Figure 5.14: The bins used for the photometory of IC5249.

In order to characterize the disk and the weakly extended light profile of IC5249, surface photometric measurements perpendicular to the galactic plane were carried out for the four regions at the positions labeled A, B, C, and D shown in Figure 5.11. Widths(parallel to galactic plane) of these regions are 4.3 kpc and heights(perpendicular to galactic plane) are 64.0 kpc. Central positions of these regions are at distances of 11.2 kpc, 6.9 kpc, -6.9 kpc and 11.2 kpc, respectively, from galactic center of IC5249. The galactic center of IC5249 was determined as the pixel of highest ADU value. In order to distinguish the extended light profile from the disk profile, the central bulge region was avoided for surface photometric measurements. The light profile at the galactic plane and four regions used for photometric measurements are shown in Figure 5.13. The regions were divided into rectangular bins with 1 pixel width from galactic plane to a distance of 2.2 kpc, 5 pixel width from 2.2 kpc to 5.5 kpc

and thereafter 5 pixel width(see Figure 5.14). The surface brightness for each bin was determined by the average ADU value. This helps one to obtain weak light from regions far off the galactic plane.

The determination of the sky level is important for accurate photometry of the extended light profile. 1 ADU in regions far from the galactic plane is nearly equivalent to a 1 - 2 magnitude difference of the brightness. The sky level of each region in both the MOA-red and the MOA-blue filters is shown in Figure 5.15. Error bars correspond to the fluctuation of ADU in regions far from the galactic plane(20 - 30 kpc) where light from IC5249 is negligible. Large error bars mean small numbers of pixels in bins because of the masking of star features. The enhanced ADU level around 19 kpc from the galactic plane in the regions A and B was caused by a star of the 13.0 magnitude in the V passband. While the sky level in the image of the MOA-blue filter is uniform, that of the MOA-red filter has inclination of sky level perpendicular to the galactic plane. The difference of sky level on both sides was about 0.1 - 0.2%. The reason for the inclination of the sky level may be an air mass effect ,as IC5249 was observed with the MOA-red filter at the end of October and November when the latitude of IC5249 was moderately low. The difference of the air mass causes the change of sky brightness. In comparison with regions A and B, the tendency of the inclination is more remarkable in regions C and D. Two bright red stars near these regions might cause this effect(see Figure 5.6). The sky levels were determined by the median value for regions from the galactic plane(20 - 30 kpc). The enhanced ADU level in regions A and B mentioned above were not used for the determination of the sky levels. The value of the sky level was 293.8 ADU in the MOA-blue filter and 1732.9 in the MOA-red filter. In the image of the MOA-red filter, the sky level was higher than that of the MOA-blue filter implying larger fluctuations and there was also

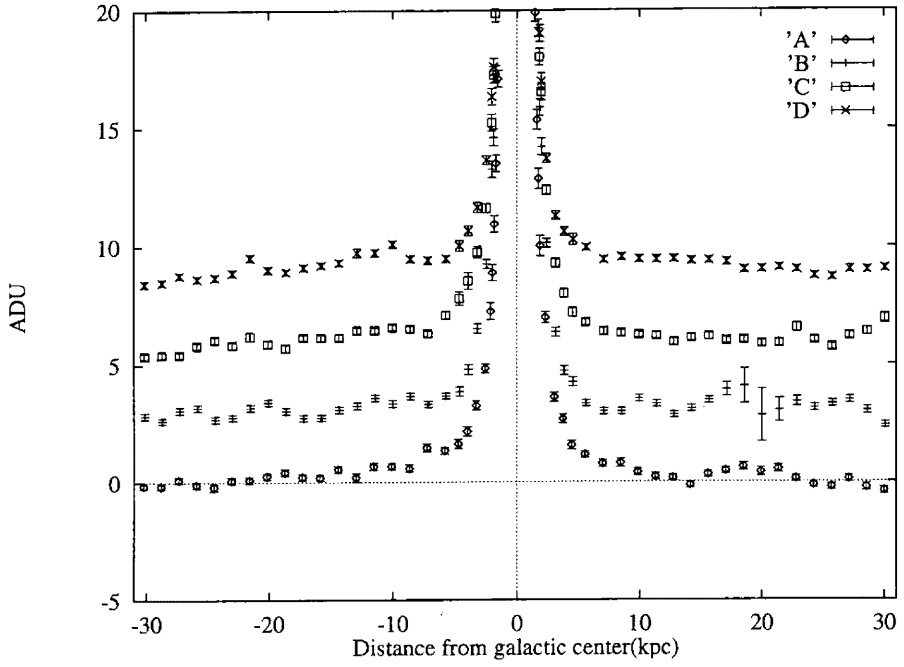

(a) MOA-blue filter

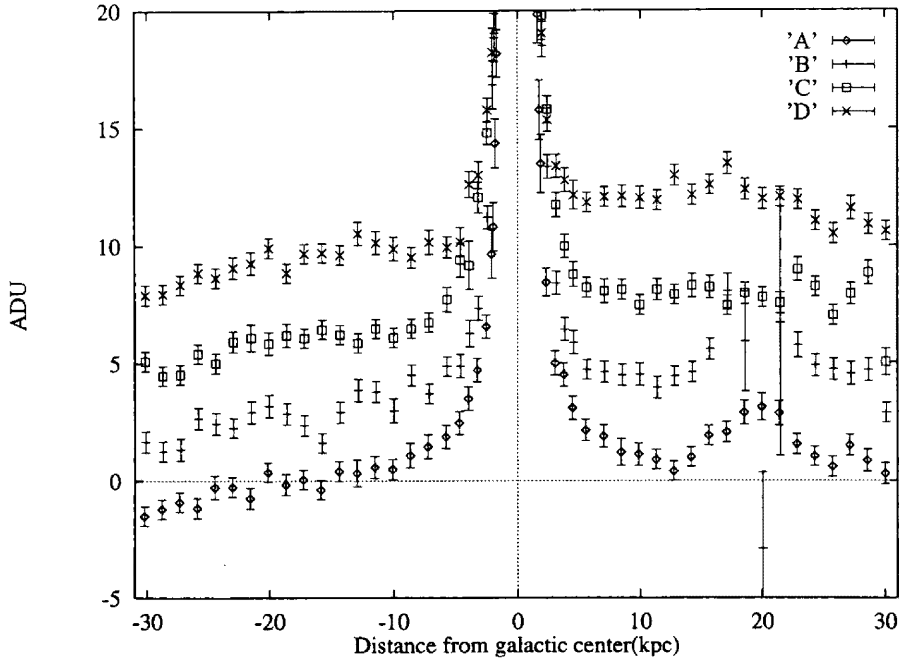

(b) MOA-red filter

Figure 5.15: The sky conditions of A, B, C and D region. The horizontal axis shows the perpendicular distance from the galactic plane in kpc and the vertical axis shows the sky condition in ADU. Each condintion is the result of sky level subtraction. The conditions of B, C and D region are added 3, 6 and 9 ADU, respectively.

an inclination of the sky level. As well, the total exposure time of the MOA-red filter of 5 hours 48 minutes was shorter than that of the MOA-blue filter which was 9 hours 9 minutes. The image obtained by the MOA-blue filter was used mainly for the following analysis, but in order to get the color profile, the image of the MOA-red filter was also used.

The light profile of each region in the MOA-blue filter is shown in Figure 5.16. The whole light profiles contain a clearly extended light profile from 5.0 kpc to 10.0 kpc in addition to a straight line profile that fits the observational data from 0.5 kpc to 2.5 kpc. In Figure 5.16, the straight line indicates an exponential profile. An exponential profile has been observed in many galaxies(Wainscoat et al 1989; Aoki et al 1991). The deviation from an exponential profile near the galactic plane is caused by dust absorption. Dust absorption was also confirmed by other observations(Wainscoat et al 1989; Aoki et al 1991; van Dokkum et al 1994). Color profiles of whole regions were obtained using the final images of both tho MOA-red and MOA-blue filters and are shown in Figure 5.17. As mentioned above, in the final image of the MOA-red filter, an inclination of the sky level exists. In order to get accurate color profiles, the sky level in the final image of the MOA-red filter was corrected. Correction of sky level was done by setting a single baseline for each profile as the best linear fit to the data from -30 to -20 kpc and from +20 to +30 kpc. The sky profiles of region C before correction and after correction are shown in Figure 5.18. After correction of the sky level in the final image of the MOA-red filter, color profiles were deduced by calculating the ratio of the intensity measured by the MOA-red filter to that by the MOA-blue filter. The color profile becomes increasingly more red with distance from the galactic plane. This phenomenon was confirmed by observations of NGC5907(Lequeux et al 1996) and NGC7814($00h03m18s, 16°09'00''$)(Lequeux, Dantel-Fort & Fort 1995) in the V

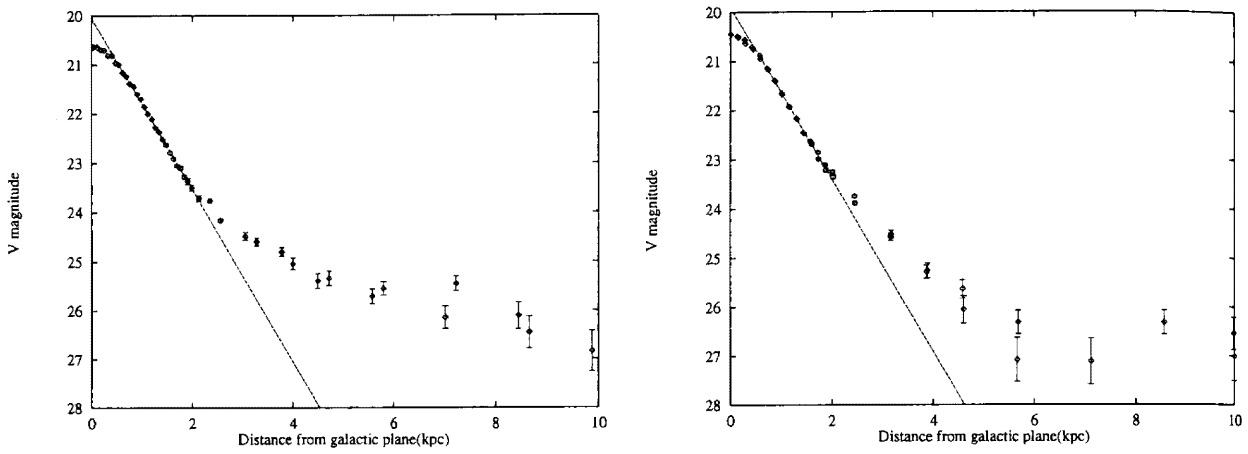

(a) A region

(b) B region

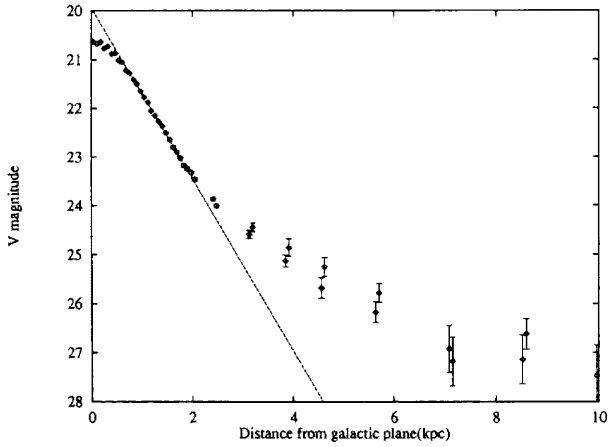

(c) C region

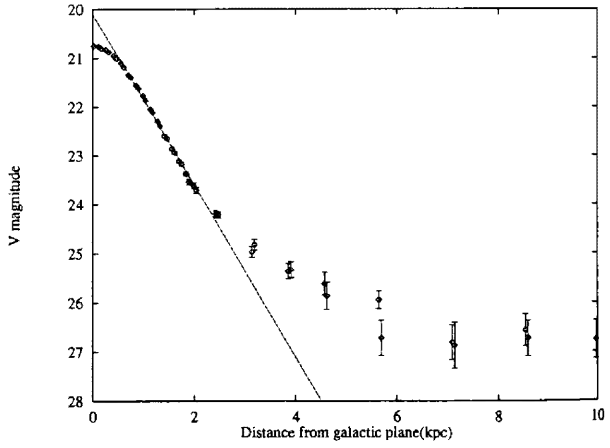

(d) D region

Figure 5.16: The brightness profiles of IC5249 in A, B, C and D region. The horizontal axis shows the perpendicular distance to the galactic plane in kpc, and the vertical axis shows the surface brightness of V passband in $magnitude/arcsec^2$

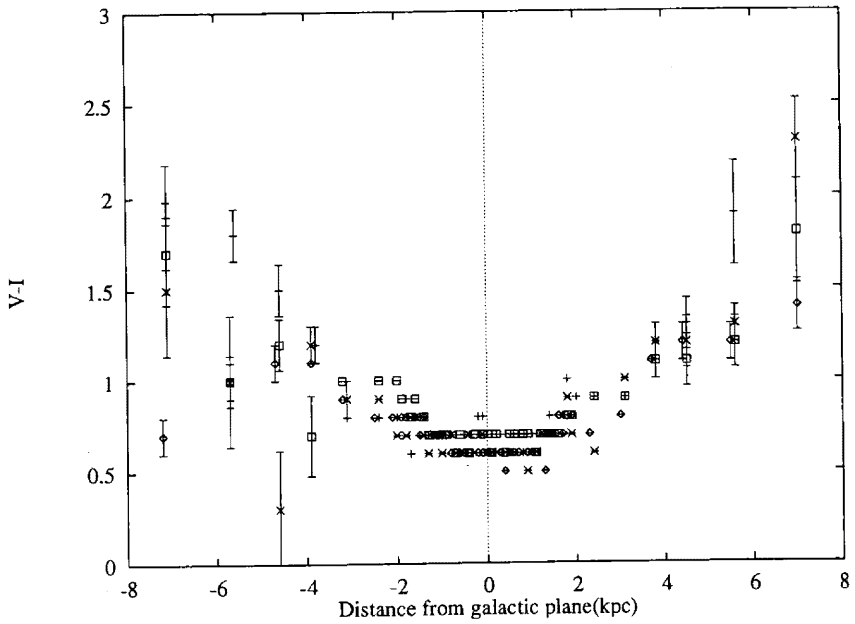

Figure 5.17: The color profiles of IC5249 perpendicular to the galactic plane. The horizontal axis shows the perpendicular distance to the galactic plane in kpc, and the vertical axis shows the color in V-I magnitude.

and I passband.

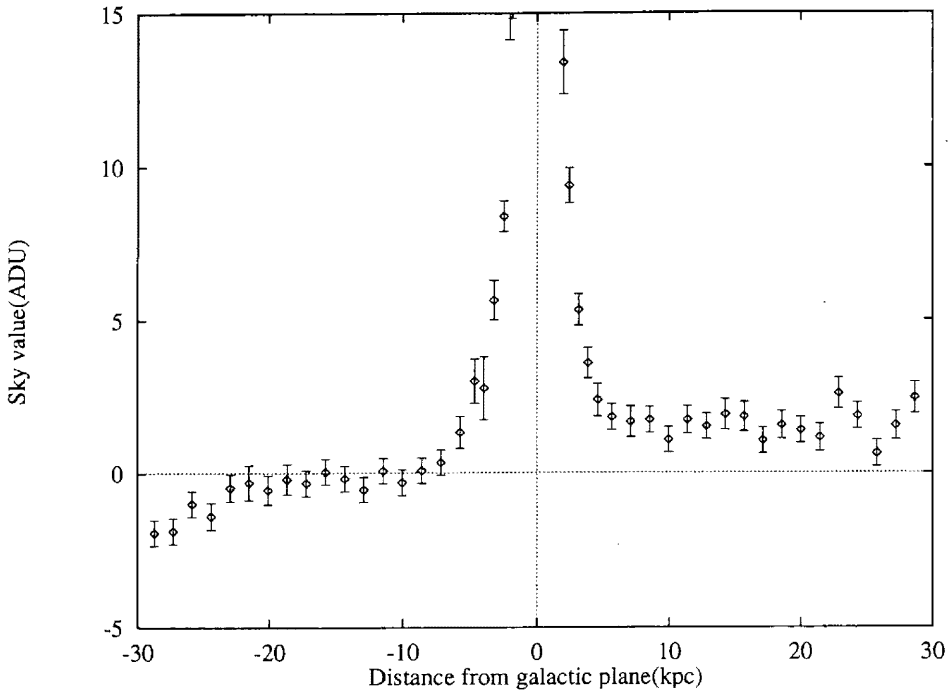

(a) Before correction

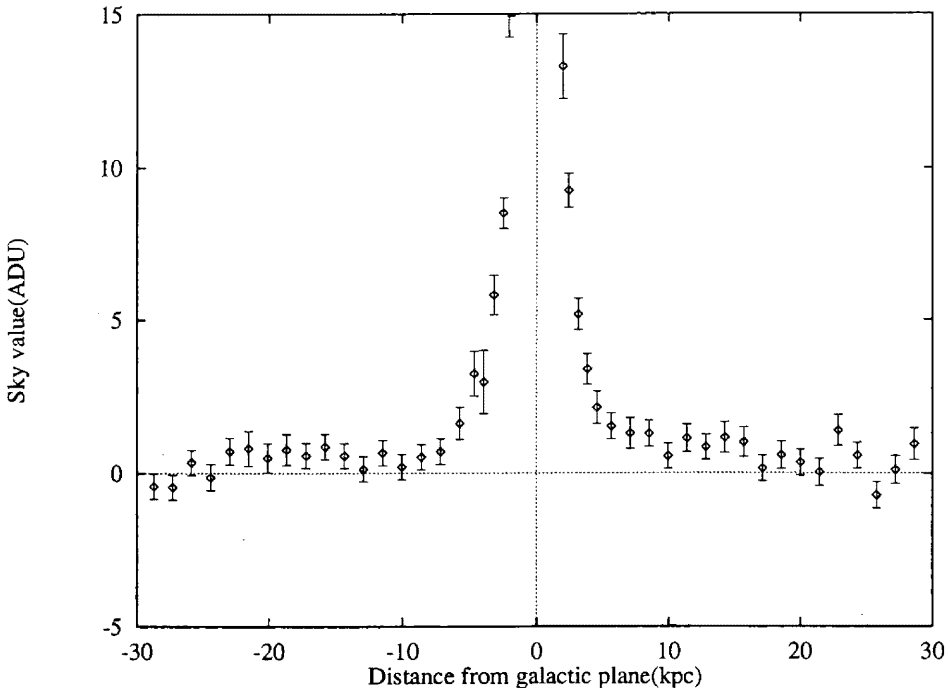

(b) After correction

Figure 5.18: Correction of the sky level. The horizontal axis shows the perpendicular distance to the galactic plane in kpc, and the vertical axis shows the sky condition in ADU.

Chapter 6

Discussion(Interpretation of observed data)

In this chapter, I attempted to fit the observed data shown in Figure 5.16 to various models, and discuss which model provided the best fit. The component of the detected light profile was also considered using the mass-to-light ratio and the color information.

6.1 Thin disk model

Near-infrared and optical observations of edge-on galaxies have established that the light profile perpendicular to the galactic plane appear to be fit by an exponential function as expressed in equation (6.1)(Wainscoat et al 1989; Aoki et al 1991).

$$S(z) = S_1 exp(-|z|/h_z) \tag{6.1}$$

Here S_1, z and h_z represent surface brightness in the galactic plane, perpendicular distance from the galactic plane and scale height, respectively. The exponential model is mathematically attractive because of its simplicity, although there is no firm physical basis for such a model.

As Burkert & Yoshii state, an exponential vertical mass density distribution can be constructed by adding up multiple stellar disk components(Burkert & Yoshii 1996). However, this can only be done if the contributions from stars with larger velocity dispersion increasingly dominate with increasing distance from the galactic plane. A mechanism to account for such a process is as yet unknown. Fuchs & Wielen tried to fit the results of the dynamical evolution models of our Galactic disk to the observed data, in order to calculate both the kinematics and the vertical stellar distribution(Fuchs & Wielen 1987). They concluded that the resulting vertical stellar distribution was better approximated by an exponential function, whereas the velocity dispersion showed a moderate, but significant gradient with distance from the Galactic plane as found in the result of Burkert & Yoshii.

The light profiles of the 4 regions in the final image obtained by the MOA-blue filter(Figure 5.11) were fitted to the equation (6.1). Fitted regions were $\pm$0.8-1.9 kpc from the galactic plane where there was no influence of absorption from the dust lane. The parameters for fitting are shown in Table 6.1.

Table 6.1: Parameters for fitting of equation(6.1)

Region	$S_1(m_V/arcsec^2)$	$h_z(pc)$
A	19.94	592
B	19.87	610
C	19.96	625
D	19.98	591

From Table 6.1, one finds that there are no large changes of surface brightness within the 4 regions. Many observations showed that the thin disk brightness distribution of spiral galaxies was described by an exponential function (Simien & de Vaucouleurs 1986; Kent 1984; de Jong & van der Kruit 1994; Walterbos

& Kennicutt 1987; Wevers, van der Kruit & Allen 1986). A small decrease of surface brightness with increasing galactocentric distance means that IC5249 has large scale length. It also seems that the scale heights of the 4 regions are almost equal. The mean value of these scale heights is 604.5 pc and the standard deviation is 14.0 pc(2.3 %). Many other observations also confirmed the constancy of the scale height. van der Kruit & Searle found, at least for their sample of edge-on galaxies, that the vertical scale height is in good approximation independent of position along the major axis(galactic plane)(van der Kruit & Searle 1981a; 1981b; 1982a; 1982b). Later studies of NGC891 ($02h22m36s, 42°21'00''$)(Kylafis & Bahcall 1987), NGC4565(Jensen & Thuan 1982) and NGC5907(Barnaby & Thronson Jr. 1992) also confirmed this phenomenon. Shaw & Gilmore studied a sample of 10 edge-on galaxies in which they found that the variation of disk scale heights as a function of galactocentric distance is typically within $\pm$ 3% of the observed mean value(Shaw & Gilmore 1990).

A possible explanation for the constancy of the scale height is the heating of the thin disk by giant molecular clouds or spiral structure (van der Kruit & Searle 1982b; Barnaby & Thronson Jr. 1992; Spitzer & Schwarzchild 1951; Lacey 1984; Carlberg & Sellwood 1985). However, to date there is no satisfactory explanation as to how the disk heating, with observed distribution of molecular clouds, can naturally lead to this result(de Grijs et al 1997). An alternative explanation for the consistency of the scale height was proposed by Bertin & Lin (Bertin & Lin 1987). They assumed that the heating of the thin disk was caused by a spiral instability owing to the birth of young stars. However, on closer inspection, the scale height seems to increase in the radially outer parts of a number of galaxies including our Galaxy(Kent et al 1991; de Grijs & Peletier 1997; van der Kruit & Searle 1981a; 1981b). In this thesis, I

used the constancy of the scale height for fitting the observed data to the thin disk and thick disk models.

The observed data, which were obtained in the region ±0.8-1.9 kpc from the galactic plane (dust free regions) in whole 4 regions, were fitted to the thin disk model described in the equation (6.2). Then the scale parameters(scale length and scale height) of IC5249 were extracted.

$$L(R,z) = L_0 exp(-|R|/H) exp(-|z|/h) \tag{6.2}$$

Here R and z denote the cylindrical radial and transverse coordinates relative to the disk, respectively. H and h denote a scale length and a scale height, respectively. L_0 is the central luminosity density of IC5249. For observers, the light profile of IC5249 is seen as a projected form of equation (6.2) on the celestial sphere. The observed data were fitted to line integrals of the luminosity density(equation (6.2)) assuming IC5249 to be perfectly edge-on. The equation (6.3) shows the integrated form of the equation (6.2) along observers' line of sight.

$$\begin{aligned} S(R,z) &= \int_{-\infty}^{\infty} L_0 exp(-|R|/H) exp(-|z|/h) dl \\ &= 2L_0 exp(-|z|/h) \int_0^{\infty} exp(-|R|/H) dl \\ &= 2L_0 exp(-|z|/h) R \int_0^{\infty} exp\left\{-R\sqrt{(1+x^2)}/H\right\} dx \end{aligned} \tag{6.3}$$

Relation between the galaxy and its parameter describing its geometry are shown in Figure 6.1. The set of parameters (L_0, R, h), with which the equation (6.3) reproduced the observed data the best(χ^2 was smallest), were calculated.

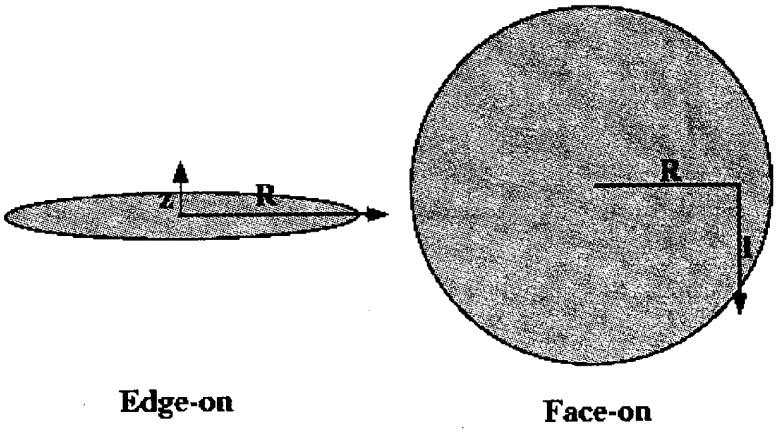

Figure 6.1: The relation between the galaxy and its parameters.

For this purpose, the Powell method was used(Press et al 1992). The results are shown in Table 6.2 and Figure 5.16.

Table 6.2: Parameters for the thin disk model

Parameter	Corresponding Value
$L_0(ADU)$	1.01
$h(pc)$	602
$H(Kpc)$	19.9

In Table 6.3, the scale parameters of other edge-on galaxies of de Grijs are shown(de Grijs 1997). Here h_I, H_B, H_I, H_K and V_{rot} denote the scale height obtained by the I passband, the scale length by the B passband, the I passband, and the K passband and the rotation velocity of the galaxy, respectively. The scale length of IC5249(H) is slightly large in comparison with the value for other edge-on galaxies (5.0-10.0 kpc). However, the scale length obtained by the MOA-cam1 with the MOA-red filter(Abe et al 1999) was 11 kpc, which means that the scale length ratio of the MOA-blue filter to that of MOA-red

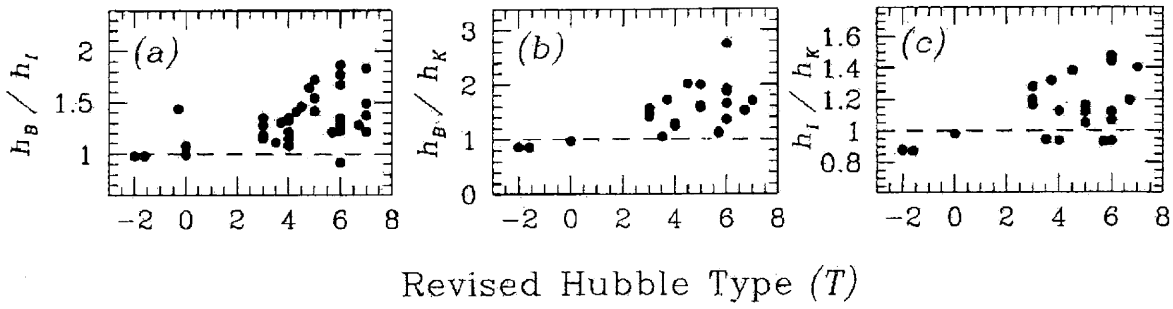

Figure 6.2: The scale length ratios of B, I and K passband observed by de Grijs. The horizontal axis shows the revised Hubble types, and the vertical axis shows the scale length rations between two passbands.

filter is 1.73.

The value of 1.73 is included in that of the B versus I passband scale length ratio of Sc(or Sd) galaxies, which is shown by de Grijs(de Grijs 1997). The galaxy type of IC5249 is also Sc or Sd. The scale length ratios of the B, I and K passbands extracted by de Grijs are shown in Figure 6.2 as a function of the revised Hubble type. The horizontal axis and the vertical axis show the revised Hubble type and the scale length ratio between two passbands, respectively. The revised Hubble types indicate the shapes of the galaxies. The values of -2, 1, 3, 6 and 8 correspond to S0, Sa, Sb, Sc and Sc-Irregular galaxies, respectively. The revised Hubble type of IC5249 is about 7 since its galaxy type is Sc or Sd. In Figure 5.16, it is obvious that another light profile exists in addition to the thin disk described by exponential function. The observed data are fit to the two component models (the thin disk plus other component) in the following sections.

Table 6.3: Scale parameters of edge-on galaxies

Galaxy name(ESO)	$h_I(kpc)$	$H_B(kpc)$	$H_I(kpc)$	$H_K(kpc)$	$V_{rot}(km/s)$
026-G06	0.38	3.58	2.95	2.10	100
033-G22	0.47	7.72	4.21		113
041-G09	0.76	7.36	6.07	6.52	182
074-G15	0.22	4.83	3.61		
138-G14	1.16	17.33	9.80	6.78	106
141-G27	0.29	3.51	2.63	1.83	87
142-G24	0.57	4.47	3.49	2.93	121
157-G18	0.33	3.20	2.50	2.35	91
201-G22	0.65	6.67	4.72	4.21	165
202-G35	0.26	1.81	1.57		116
235-G53	1.49	7.32	5.74		
240-G11	0.62	11.15	6.79		241
263-G15	0.37	6.47	3.87	3.45	
263-G18	0.56	6.21	4.59		
269-G15	0.54	5.42	4.07		176
286-G18	1.67	9.21	8.01	7.10	323
288-G25	0.41	2.28	2.10		
311-G12	0.28	1.18	1.18	1.21	
315-G20	0.88	4.99	4.26	4.00	
321-G10	0.38	2.03	1.89		145
322-G73	1.22	2.87	1.99		
322-G87	0.35	2.21	1.91		149
340-G08	0.32	2.63	1.95		99
340-G09	0.50	2.26	2.00	1.45	96
358-G26	0.46	0.95	0.97		
358-G29	0.56	1.02	1.04	1.19	160
383-G05	1.46	6.06	4.65	3.52	
416-G25	0.96	3.59	3.13	2.45	209
435-G14	0.52	4.62	3.00	2.86	162
435-G25	0.57	10.16	5.91	5.09	201
435-G50	0.27	2.14	1.69		79
437-G62	0.66	3.77	3.20	2.67	
444-G21	0.43	2.72	2.97		109
446-G18	0.55	5.38	3.99	3.43	190
446-G44	0.40	8.17	4.38	2.97	151
460-G31	0.97	9.95	6.81	4.93	225
487-G02	0.48	2.44	2.19	2.32	154
500-G24	0.53	1.76	1.80	2.05	
505-G03	0.20	3.52	2.36		89
506-G02	0.75	7.59	5.39		208
509-G19	1.86	11.74	8.86	9.44	
531-G22	0.55	4.55	3.75		177
564-G27	0.46	9.43	5.34	5.71	162
575-G61	0.31	2.39	1.74		65

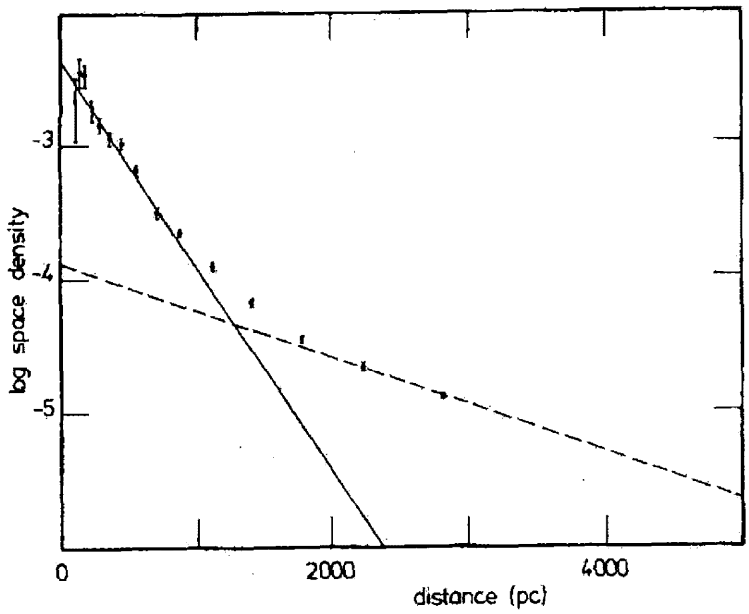

Figure 6.3: The observation result of our Galaxy by Gilmore and Reid. The horizontal axis shows the perpendicular distance to the galactic plane in pc, and the vertical axis shows the surface density of stars in log scale. The observation result is well reproduced by two component, the thin disk(solid line) and the thick disk(dashed line).

I considered 4 different types of light profiles for the other component added to the thin disk. Those are the thick disk model described by an exponential function(section 6.2), the globular cluster model described by inverse proportionality to the 3.5th power of galactocentric distance (section 6.3), the spherical halo model described by inverse proportionality to the square of galactocentric distance(section 6.4) and the flat halo model which is a flattened version of the spherical halo to the galactic plane(section 6.5). In the following sections, I fit the observed data to each model and examined which model best reproduces the data.

6.2 Double disk model

A thick disk was first detected by Burstein in a small sample of edge-on S0 galaxies(Burstein 1979). A thick disk has a larger scale height than that of the dominant thin disk component. In our Galaxy, Gilmore & Reid found the thick disk by deriving absolute magnitudes from photometric parallaxes for 12,500 stars around the South Galactic Pole(Gilmore & Reid 1983). Their result is shown in Figure 6.3. The vertical and horizontal axes show the surface density of stars on a logarithmic scale and the vertical distance from Galactic plane in units of pc, respectively. The observed data in Figure 6.3 are reproduced by two straight lines. The solid line represents the contribution of the thin disk, and dashed line corresponds to the contribution from the thick disk. They concluded that the scale height of the thick disk was 1450 pc, and 2 % of the stars in the solar neighbourhood comprised of this component. One of the most convincing examples of the existence of a thick disk component was found by van Dokkum et al in the case of the edge-on galaxy NGC6504($17h56m6s, 33°12'36''$), with a scale height (4.2 kpc) approximately 4 times the thin disk scale height(1.1 kpc) (van Dokkum et al 1994).

A number of possible origins for these thick disks can be considered. They could be truly separate dynamical components of galaxies, or due to the contribution from the light profile of the bulge (Freeman 1985). Other opinions are as follows. The thick disk could be the spheroidal component itself, responding to the flat potential of the thin disk(van der Kruit & Searle 1981b; Freeman 1985; Bahcall & Kylafis 1985; Jarvis & Freeman 1985), or it could be an intermediate population which formed at the same time as the spheroid formed (Gilmore 1984). However, de Grijs & Peletier argued that it was likely that the formation mechanism for the thick disk and the origin of the increasing scale height as a function of projected galactocentric distance were similar (de

Grijs & Peletier 1997). They ruled out the possibility that the thick disk was the intermediate component in a hierarchical formation scenario between the bulge and the thin disk. Therefore, the more likely formation mechanisms for the thick disk invoke the accretion of material by the early thin disk, causing violent dynamical heating processes to take place, thereby thickening the thin disk(Norris 1987; Statler 1989; Quinn et al 1993).

There is a possibility that a thick disk also exists in IC5249. The galactic model described in equation (3.2), which contained the thin disk and the thick disk, was considered(the double disk model). Here the subscripts 0 and 1 refer to the parameters of the thin disk and the thick disk, respectively. The observed data in the region of $\pm$0.8-10.0 kpc from the galactic plane in whole 4 regions(see Figure 5.11) were fitted to this model. As in the case of the thin disk model, the observed data were fitted to line integrals of the luminosity density(equation (3.2)) assuming IC5249 to be perfectly edge-on. Equation (6.4) shows the integrated form of equation (3.2) along observers' line of sight. The Powell method was used for fitting the data to this equation.

$$S(R,z) = 2L_0 exp(-|z|/h_0) R \int_0^\infty exp\left\{-R\sqrt{1+x^2}/H_0\right\} dx$$
$$+2L_1 exp(-|z|/h_1) R \int_0^\infty exp\left\{-R\sqrt{1+x^2}/H_1\right\} dx \quad (6.4)$$

The parameters for the double disk model are shown in Table 6.4. The result of fitting and the observed data in region B and C are shown in Figure 6.4.

Table 6.4: Parameters for the double disk model

Parameter	Corresponding Value
$L_0(ADU)$	0.997
$h_0(pc)$	543
$H_0(Kpc)$	21.4
$L_1(ADU)$	0.0408
$h_1(pc)$	3000
$H_1(Kpc)$	14.3
L_1/L_0	0.041
h_1/h_0	5.52
Reducedχ^2	1.1

A small reduced χ^2 means that the observed data were reproduced well by the double disk model. L_1/L_0 and h_1/h_0 are nearly equal to those of our Galaxy extracted by Gilmore & Reid($L_1/L_0 = 0.02, h_1/h_0 = 4.5$; Gilmore & Reid 1983). As a result, it is likely that the light profile in association with the thin disk in IC5249 is the thick disk.

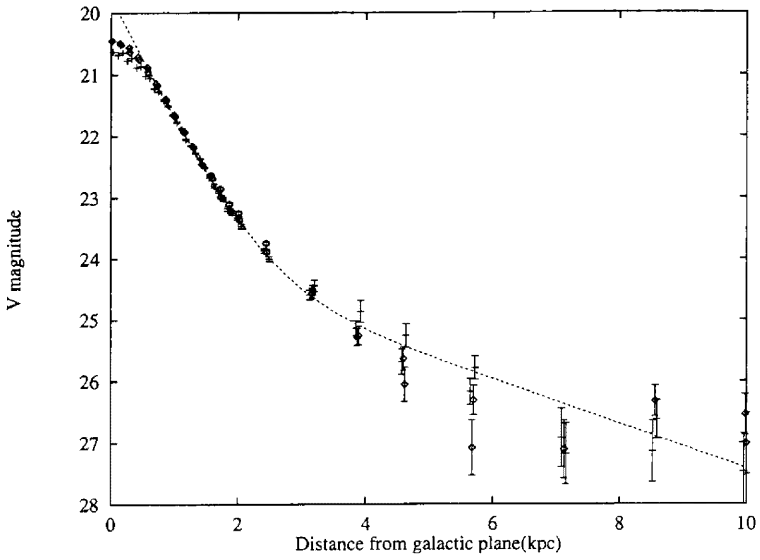

Figure 6.4: The result of fitting by double disk model and observed data in region B and C. The horizontal axis shows the perpendicular distance to the galactic plane in kpc, and the vertical axis shows the surface brightness in V passband. Diamons and crosses with error bars represent the observed data and dashed line represents the fitted result by double disk model.

6.3 Thin disk model + globular cluster model

Many spiral galaxies and elliptical galaxies possess a large number of globular clusters. It is considered that a spiral galaxy may contain a few hundred globular clusters while an elliptical galaxy contains a few thousand(Harris & Racine 1979). The process of constructing globular clusters depends seriously on how galaxies were formed in an early time of the universe. There are presently two scenarios being considered for galaxy formation. One is that galaxies were formed over a short time period of a hundred million years or so(Eggen, Lynden-Bell & Sandage 1962), and the other calls for formation over a long time period of a thousand million years or so(Searle & Zinn 1978).

In the former scenario, globular clusters and halo stars were born when huge gas clouds of size in 100 kpc collapsed to galaxies by free fall. In this case, the ages of globular clusters are nearly the same. In latter scenario, galaxies

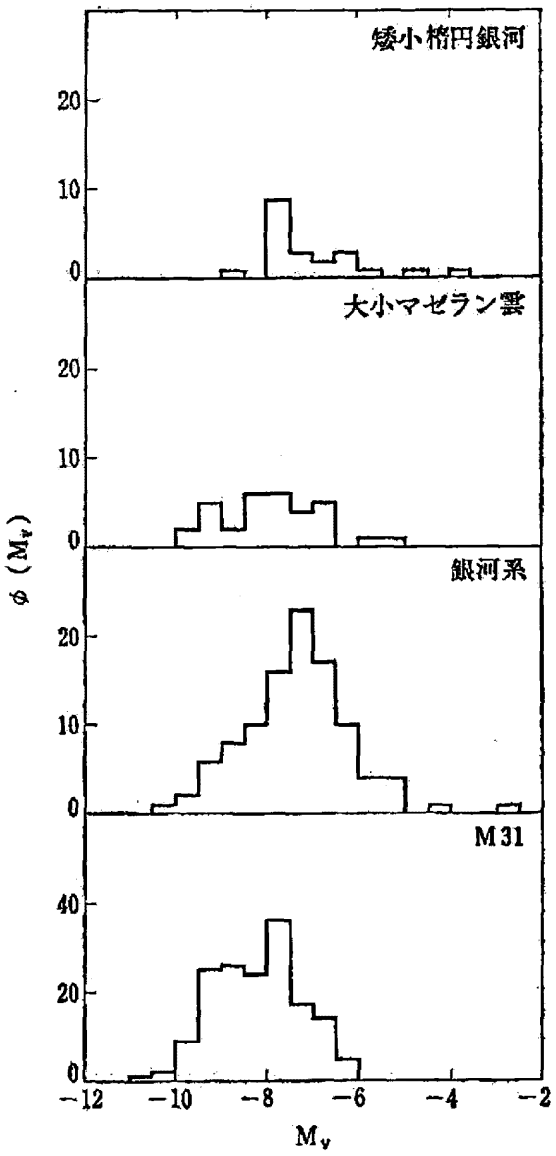

Figure 6.5: The luminosity functions of globular cluster for some galaxies. The horizontal axis shows the absolute magnitude of globular cluster, and the vertical axis shows the number of the globular clusters.

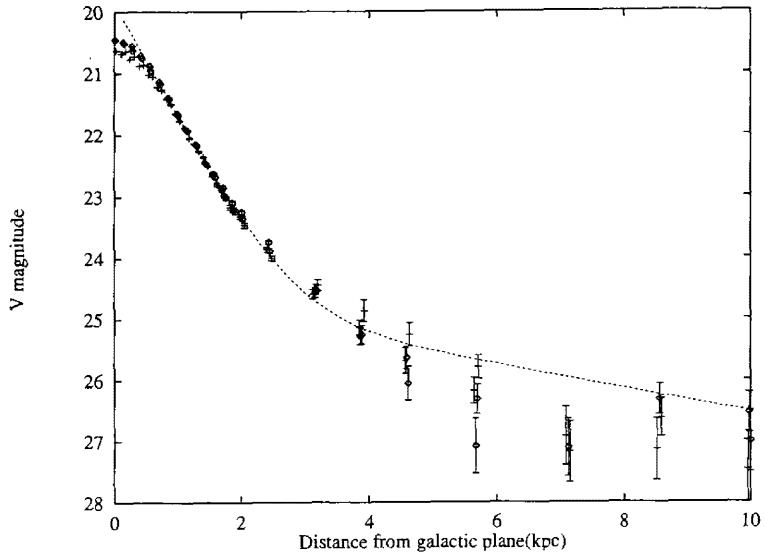

Figure 6.6: The result of fitting by thin disk + globular cluster model and observed data in region B and C. The horizontal axis shows the perpendicular distance to the galactic plane in kpc, and the vertical axis shows the surface brightness in V passband. Diamons and crosses with error bars represent the observed data and dashed line represents the fitted result by thin disk + globular cluster model.

were gradually formed by hierarchical merging of sub-systems which caused the formation of globular clusters. In this case, the ages of globular clusters were dispersed in time to some extent.

The number distributions of globular clusters in some galaxies are shown in Figure 6.5. The horizontal axis shows the absolute magnitude of globular clusters in the V passband. In Figure 6.5, the typical absolute magnitude of a globular cluster is about -8, which corresponds to 25 magnitude for the distance of 36 Mpc to IC5249. From the results of the calibration(see section 5.3), the 25 magnitude in the V passband is equivalent to about 2 ADU. This means that it is impossible to detect each globular cluster in the final image of IC5249. These globular clusters may togerher emit light in addition to the thin disk profile. Globular clusters in our Galaxy are distributed as described in equation (6.5)(Arimoto 1982).

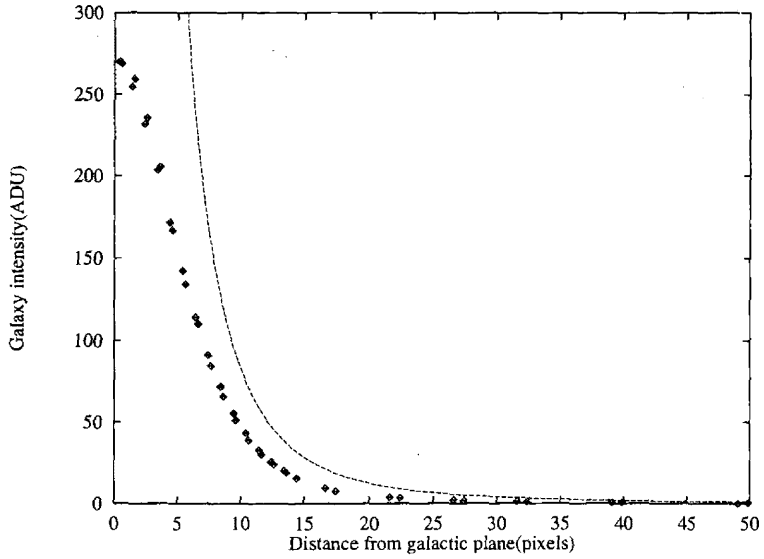

Figure 6.7: The observation data of region 1 and the fitting result. The horizontal axis shows the perpendicular distance to the galactic plane in pixel, and the vertical axis shows the surface brightness of V passband in ADU. Diamons and crosses with error bars represent the observed data and dashed line represents the fitted result by thin disk + globular cluster model.

$$\varphi(r) \propto r^{-3.5\pm0.5} \tag{6.5}$$

The thin disk + globular clusters model described in equation (3.4) was considered as a galactic model. The same process as the fit to the double disk model was invoked. The observed data in the distance of ±0.8-10.0 kpc from the galactic plane of the 4 regions were fit to the line integrals of equation (3.4). Equation (6.6) shows the integrated form of equation (3.4) along observers' line of sight. The Powell method was used for fitting the data to this equation.

$$\begin{aligned} S(R,z) &= 2L_0 exp(-|z|/h_0)R\int_0^\infty exp\left\{-R\sqrt{1+x^2}/H_0\right\}dx \\ &+\frac{2L_{gc}H_0^{3.5}}{(R^2+z^2)^{1.25}}\int_0^\infty \frac{1}{(1+x^2)^{1.75}}dx \end{aligned} \tag{6.6}$$

The parameters for the thin disk + globular clusters model are shown in Table 6.5. For comparison, the result of fitting and the observed data in the regions B and C are shown in Figure 6.6.

Table 6.5: Parameters for the thin disk + globular cluster model

Parameter	Corresponding Value
$L_0(ADU)$	0.746
$h_0(pc)$	588
$H_0(kpc)$	25.9
$L_{gc}(ADU)$	2.66×10^{-4}
L_{gc}/L_0	3.56×10^{-4}
Reducedχ^2	1.9

The reduced χ^2 is larger than that for the double disk model. On the basis of the reduced χ^2 and the number of degrees of freedom(138), the thin disk + globular cluster model is rejected with confidence level of 99.5 %. The light profile of the region 1 in Figure 5.11 and the values calculated from equation (6.6) in the region with the parameters described in Table 6.5 are shown in Figure 6.7. Diamonds show the observed light profile, and the dashed line shows the values determined from equation (6.6). The bulge is included in region 1. Therefore, the values determined from equation (6.6) should show lower ADU values than the observed data, if the thin disk + globular cluster model is correct, because the bulge profile is not considered in equation (6.6). However, the opposite result is seen in Figure 6.7. This means that the expected light profile of the thin disk + globular clusters model, which is fitted to the observed data of regions A, B, C and D in Figure 5.11, is not able to explain the light profile of the region 1. These results virtually reject the notion that

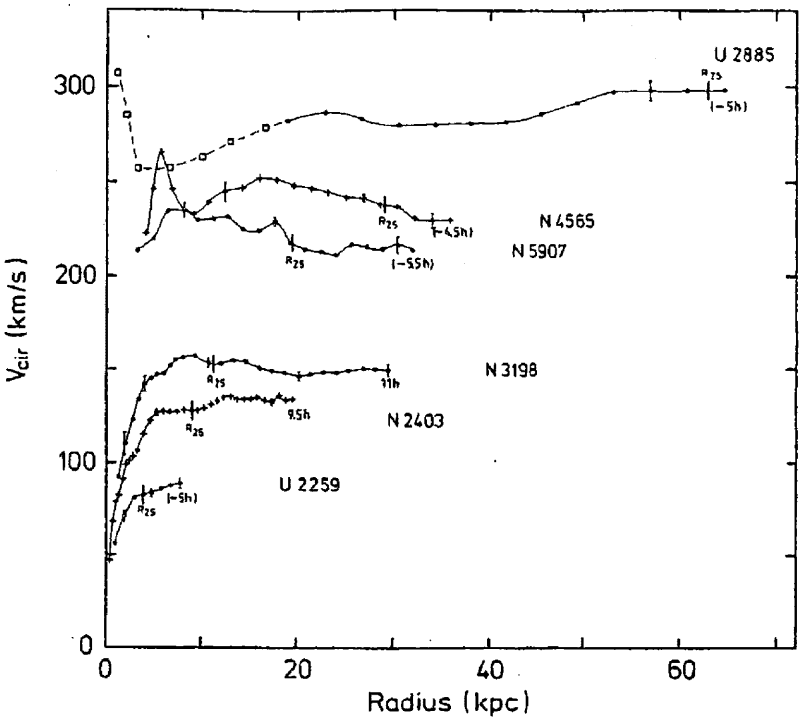

Figure 6.8: The rotation curves of some galaxies. The horizontal axis shows the distance from the galactic center along the galactic plane in kpc, and the vertical axis shows the rotation velocity in km/s.

the light profile in addition to the thin disk is caused by globular clusters.

6.4 Thin disk + spherical halo model

Optical and radio observations have shown that many spiral galaxies including our Galaxy have a constant rotational velocity at any place in the galactic plane(Rubin & Ford 1970; Sofue 1996).

The rotation curves of some spiral galaxies are shown in Figure 6.8(Sancisi & van Albada 1987). The most simple density distribution of a spiral galaxy, which shows a flat rotation curve as described in Figure 6.8, is inversely proportional to the square of the galactocentric distance following equation (6.7). However, actual light profiles observed by using optical photomety show an exponential distribution along the galactic plane, which decreases its density rapidly in comparison with the equation (6.7)(see Figure 6.9). This means

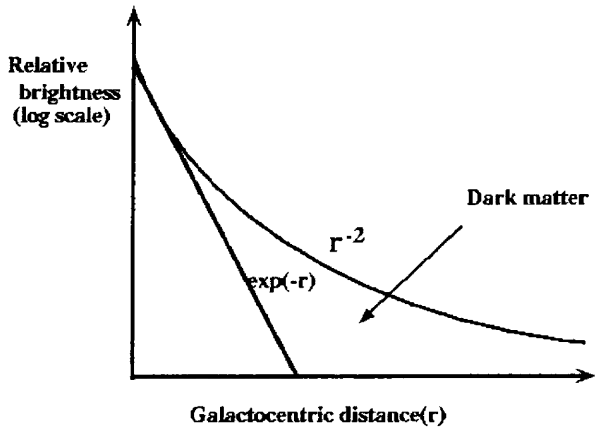

Figure 6.9: exponential profile and the inverse proportional distribution to the square of galactocentric distance. The horizontal axis shows the distance from the galactic center, and the vertical axis shows the relative brightness in log scale.

that spiral galaxies contain a lot of dark matter, which is not explained by the exponential distribution.

$$\rho(r) = \frac{V^2}{4\pi G r^2} \tag{6.7}$$

As described in Chapter 1, dark matter in spiral galaxies may be composed of red dwarfs or brown dwarfs. If this is in case, red dwarfs or brown dwarfs, which show mass distribution following equation (6.7), contribute to the emission of the light profile in association with the thin disk.

Therefore, the thin disk + spherical halo model described in equation (3.3) was considered as a galactic model. The same process as the fit to the double disk model was carried out. The observed data in the range of $\pm$0.8-10.0 kpc from the galactic plane in regions A, B, C and D, were fit to the line integrals of equation (3.3). Equation (6.8) shows the integrated form of equation (3.3) along observers' line of sight where the Powell method was used to fit the data

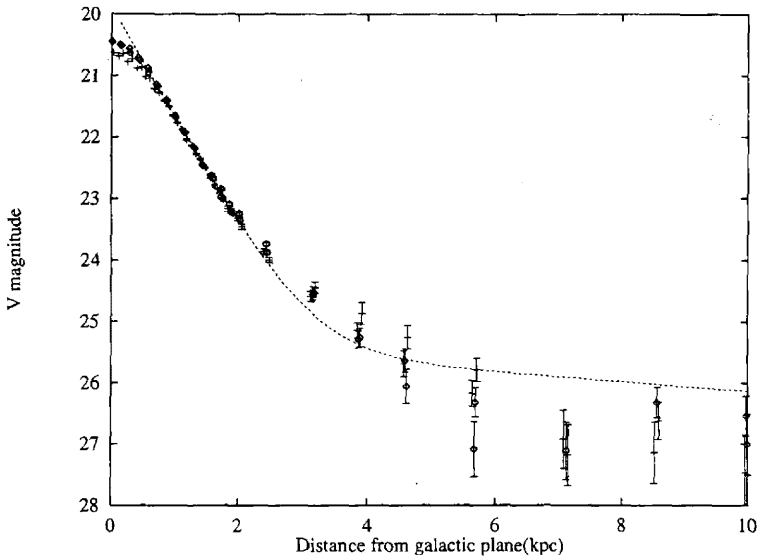

Figure 6.10: The result of fitting by thin disk + spherical halo model and observed data in region B and C. The horizontal axis shows the perpendicular distance to the galactic plane in kpc, and the vertical axis shows the surface brightness in V passband. Diamons and crosses with error bars represent the observed data and dashed line represents the fitted result by thin disk + spherical halo model.

to this equation.

$$S(R,z) = 2L_0 exp(-|z|/h_0) R \int_0^\infty exp\left\{-R\sqrt{(1+x^2)}/H_0\right\} dx + \frac{\pi L_{dm} H_0^2}{\sqrt{R^2+z^2}} \tag{6.8}$$

The parameters for the thin disk + spherical halo model are shown in Table 6.6. For comparison, the result of the fit and observed data in regions B and C are shown in Figure 6.10. The reduced χ^2 shows a larger value than that of the double disk model. From this reduced χ^2 value and the number of degrees of freedom(138), the thin disk + spherical halo model is rejected with confidence

level of 99.5 %.

Table 6.6: Parameters for the thin disk + spherical halo model

Parameter	Corresponding Value
$L_0(ADU)$	0.957
$h_0(pc)$	598
$H_0(kpc)$	20.6
$L_{dm}(ADU)$	1.03×10^{-3}
L_{dm}/L_0	1.08×10^{-3}
Reducedχ^2	2.0

6.5 Thin disk + flat halo model

Many studies have supposed that the mass distribution of the galactic halo, which contains dark matter, is spherical as described in equation (6.7). However, the rotation curve of a spiral galaxy measured along the galactic plane is unable to determine the shape of the galactic halo (Olling 1995). As described in Chapter 1, a many observations and theories suggested that the shape of the galactic halo might be flat.

Therefore, observed data were fitted to the thin disk + flat halo model. The spherical power law model of Evans was adopted as the flat halo profile(Evans 1994). In his model, the gravitational potential is given in cylindrical coordinates (R, ϕ, z) by equation (6.9).

$$\Phi_{halo} = (v_0^2/2)log(R_c^2 + R^2 + z^2 q^{-2}) \tag{6.9}$$

Here v_0, R_c and q are the normalization of the gravitational potential, the core radius, and the axial ratio of the equipotential spheroid. $q = 1$ corresponds

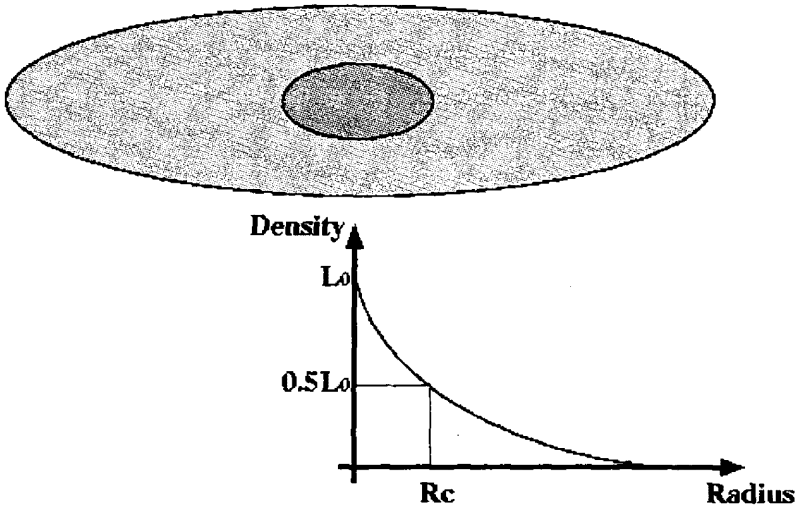

Figure 6.11: The core radius

to a spherical halo. The core is means the galactocentric distance where the mass density becomes a half that of the galactic center(see Figure 6.11). The contribution of the flat halo to the rotational velocity in the galactic plane is given by equation (6.10).

$$V_{halo} = \frac{v_0 R}{(R^2 + R_c^2)^{1/2}} \tag{6.10}$$

Equation (6.10) indicates that the rotational velocity contributed by the flat halo depends only on the core radius, and not on the axial ratio.

In Figure 6.12, the rotation curves with some core radii are shown. The solid, long dashed, short dashed and dotted curves correspond to the rotation curves with the core radius 2 kpc, 5 kpc, 10 kpc and 20 kpc, respectively. All rotation curves are set to reach 200 km/s at infinity. Figure 6.12 indicates that the rotation curve with the larger core radius has a more slowly rising curve. The density distribution of the flat halo calculated from its gravitational potential(equation (6.9)) is described by equation (6.11).

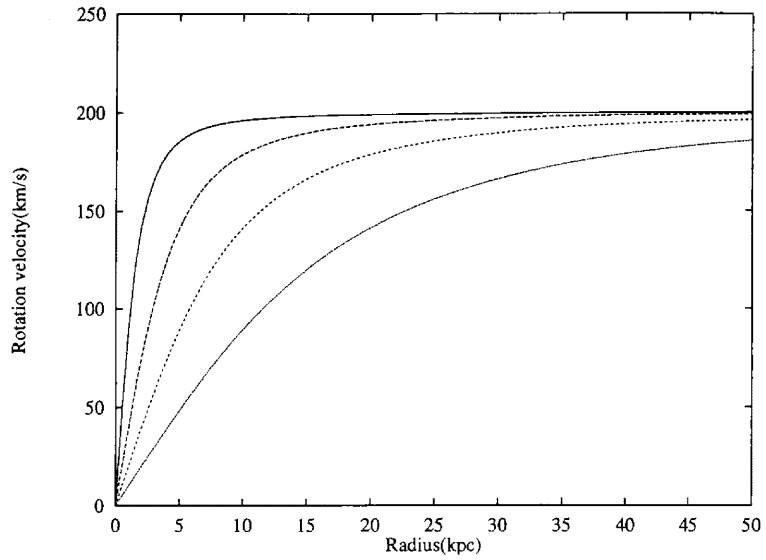

Figure 6.12: The rotation curves of halo components. The horizontal axis shows the distance from the galactic center along the galactic plane in kpc, and the vertical axis shows the rotation velocity in km/s. The solid line, long dashed line, short dashed line and dotted line represent the rotation curve of the halos with core radius of 2kpc, 5kpc, 10kpc and 20kpc, respectively.

$$\begin{aligned} \rho_{halo}(R,z) &= \frac{v_0^2}{4\pi G q^2}\left\{R_c^2(1+2q^2)+R^2+z^2(2-q^{-2})\right\} \\ &\quad \times(R_c^2+R^2+z^2q^{-2})^{-2} \end{aligned} \tag{6.11}$$

The thin disk + flat halo model described in equation (6.12) was considered as the galactic model. The same process as the fit to the double disk model was employed. The observed data in the range of ±0.8-10.0 kpc from galactic plane in regions A, B, C and D were fit to the line integrals of equation(6.12). Equation (6.13) shows an integrated form of equation (6.12) along observers' line of sight, where the Powell method was used for fitting the data to this equation.

$$
\begin{aligned}
L(R,z) &= L_0 exp(-|R|/H_0) exp(-|z|/h_0) \\
&\quad + \frac{v_0^2}{4\pi G q^2 (M/L)} \left\{ R_c^2(1+2q^2) + R^2 + z^2(2-q^{-2}) \right\} \\
&\quad \times (R_c^2 + R^2 + z^2 q^{-2})^{-2}
\end{aligned} \tag{6.12}
$$

$$
\begin{aligned}
S(R,z) &= 2L_0 exp(-|z|/h_0) R \int_0^\infty exp\left\{ -R\sqrt{(1+x^2)/H_0} \right\} dx \\
&\quad + \frac{v_0^2}{2\pi G q^2 (M/L)} \int_0^\infty \frac{\left\{ R_c^2(1+2q^2) + R^2 + l^2 + z^2(2-1/q^2) \right\}}{\left\{ R_c^2 + R^2 + l^2 + (z/q)^2 \right\}^2} dl
\end{aligned} \tag{6.13}
$$

Here M/L represents the mass-to-light ratio of the flat halo. The core radius turned out to change considerably during the fitting process. Therefore, the core radius was controlled during the fitting process, changing its value from 0.0 kpc to 40.3 kpc gradually. The parameters for the thin disk + flat halo model for each core radius are shown in Table 6.7. For comparison the result of fitting and the observed data in regions B and C are shown in Figure 6.13. The reduced χ^2 takes the minimum value for the flat halo with the core radius of 0.0 kpc. The flat halo with the core radius of 0.0 kpc has infinite mass density in the center ,which is extracted by equation (6.11) with $R_c = 0.0$, and a mass concentration at the central region of it. However, the largest reduced χ^2 is about 1.2, which means the observed data can be well fit to equation (6.13) with each set of parameters in Table 6.7. From Table 6.7, one can say that the axial ratio decreases as the core radius increases, which means the observed data can be reproduced better by a flatter halo model.

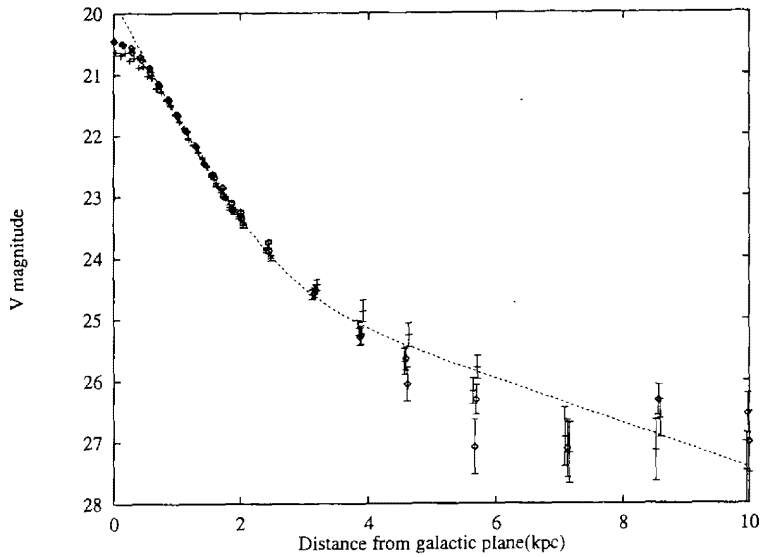

Figure 6.13: The result of fitting by thin disk + flat halo model and observed data in region B and C. The horizontal axis shows the perpendicular distance to the galactic plane in kpc, and the vertical axis shows the surface brightness in V passband. Diamons and crosses with error bars represent the observed data and dashed line represents the fitted result by thin disk + flat halo model.

6.6 The component of the flat halo

As described in previous section, it is likely that the light profile in addition to the thin disk discovered by the observation of IC5249 may be the flat halo. The flat halo was considered to be comprised of red dwarfs from the observation of NGC5907(Sackett et al 1994; Lequex et al 1996; Rudy et al 1997; James & Casali 1998). Therefore, the possibility of red dwarfs being responsible for a flat halo was examined considering the color information(Figure 5.17) and the mass-to-light ratio of IC5249.

Using the rotational velocity of IC5249(100 km/s) and the observed intensity of the flat halo, one is able to calculate the mass-to-light ratio of IC5249. Some parameter sets of the thin disk + flat halo model were selected from Table 6.7 and the mass-to-light ratio for each set was calculated. The results are

Table 6.7: Parameters for the thin disk + flat halo model

Core radius(Kpc)	$L_0(ADU)$	$h_0(pc)$	$H_0(Kpc)$	$\frac{v_0^2}{4\pi G}(ADU)$	Axial ratio	Reducedχ^2
0.0	0.790	543	26.3	22.19	0.507	0.98
1.44	0.790	543	26.3	21.95	0.504	0.98
1.88	0.808	545	25.8	21.42	0.495	0.98
4.31	0.834	545	25.1	20.63	0.481	1.00
5.75	0.867	548	24.2	19.88	0.467	1.01
7.19	0.903	549	23.3	19.20	0.451	1.03
8.63	0.937	552	22.6	18.65	0.436	1.05
10.1	1.054	556	20.3	18.01	0.422	1.09
11.5	1.056	558	20.2	17.76	0.405	1.10
12.9	1.057	558	20.2	17.57	0.389	1.11
14.4	1.059	559	20.2	17.40	0.373	1.13
15.8	1.060	559	20.1	17.27	0.359	1.14
17.3	1.061	561	20.1	17.17	0.346	1.15
18.7	1.061	561	20.1	17.09	0.334	1.16
20.1	1.062	562	20.1	17.03	0.323	1.17
25.2	1.062	565	20.0	16.97	0.289	1.20
30.2	1.064	568	19.8	17.03	0.263	1.22
35.2	1.069	569	19.7	17.18	0.240	1.23
40.3	1.077	571	19.5	17.35	0.221	1.24

shown in Table 6.8.

It is thought that stars in the flat halo were born in the formation epoch of the galaxy(stars of population II). That means the amount of metal in these stars is extremely low. Baraffe et al calculated the evolution model of low metal red dwarfs and showed its physical properties (Baraffe et al 1997). In Table 6.9, mass, effective temperature, brightness, color and mass-to-light ratio of a red dwarf calculated from the result of Baraffe et al are shown. The color of the outer region of IC5249 shown in Figure 5.17 is $V - I = 1.3 - 1.5 magnitude$. Therefore one can say that the flat halo may be composed of red dwarfs, taking account of the result of the calculation shown in Table 6.9, the observed color information of Figure 5.17 and the mass-to-light ratio in

Table 6.8: Mass to light ratio of the flat halo

Core radius(Kpc)	Axial ratio	$\frac{v_0^2}{4\pi G}(ADU)$	Mass to light ratio(in $M_\odot/L_\odot$)
0.0	0.507	22.19	18.42
5.75	0.467	19.88	20.57
10.1	0.422	18.01	22.70
20.1	0.323	17.03	24.01
30.2	0.263	17.03	24.01
40.3	0.211	17.35	23.56

Table 6.8. Red dwarfs in the halo of IC5249 possess the properties as the mass-to-light ratio $(M/L)/(M_\odot/L_\odot) \approx 20-25$, the color $V-I \approx 1.3-1.5 magnitude$ and the mass $M \approx 0.3-0.4M_\odot$.

6.7 Summary of interpretation of observed data

The light profile observed by the long exposure photometry of IC5249 was fit to various models. The additional light profile to the thin disk was confirmed obviously from the fitting of observed data to the thin disk model. Therefore, four two-components models, which were the double disk model, the thin disk + globular clusters model, the thin disk + spherical halo model and the thin disk + flat halo model, were considered to determine which model best reproduced the observed data.

The values of reduced χ^2 for the thin disk + globular clusters model and the thin disk + spherical halo model are larger than those for the double disk model and the thin disk + flat halo model. This means that the thin disk + globular clusters model and the thin disk + spherical halo model do not fit to the observed data well. Also, as shown in Figure 6.7, the thin disk + globular clusters model does not fit the light profile of the bulge region. Therefore, one

Table 6.9: Physical properties of a red dwarf

Mass of star($M_\odot$)	T_{eff}	M_V	M_I	$V-I$	Mass to light ratio(in $M_\odot/L_\odot$)
0.083	1779	20.92	14.41	6.51	226500
0.085	2342	17.67	13.11	4.56	11300
0.090	3005	14.70	11.96	2.74	798.4
0.100	3395	13.25	11.17	2.08	233.3
0.110	3565	12.63	10.76	1.87	145.0
0.130	3749	11.91	10.21	1.70	88.3
0.150	3852	11.43	9.81	1.62	65.5
0.200	4004	10.59	9.09	1.50	40.3
0.300	4172	9.58	8.19	1.39	23.8
0.400	4304	8.87	7.58	1.29	16.5
0.500	4623	7.83	6.72	1.11	7.9
0.600	5292	6.61	5.76	0.85	3.1
0.700	5914	5.51	4.83	0.68	1.3
0.750	6282	4.87	4.28	0.59	0.78
0.800	6688	3.97	3.47	0.49	0.36

can say that the other component in association with the thin disk is a thick disk or a flat halo. If the double disk model is correct, the rotational velocity of the mass distribution of equation (3.2) decreases in the outer part of the galaxy. The declining rotation curve is inconsistent with the flat rotation curve observed in many spiral galaxies, and so a third component must be added in addition to the thin and thick disk. However, some declining rotation curves have been reported(Honma 1999). If the thin disk + flat halo model is correct, the rotation curves of the mass distribution described by equation (6.11) become flat, which means that dark matter problem in association with spiral galaxies is solved(see Figure 6.12).

Figure 6.9(the result of fitting to the thin disk + spherical halo model) and Figure 6.13(the result of fitting to the thin disk + flat halo model) show that the flat halo model fits better than the spherical halo model. This suggests that the observational results, in which the halo shape is considered to be spherical, may give a wrong interpretation about the dark matter in spiral galaxies. Also, Figure 6.4(the result of fitting to the double disk model) and Figure 6.13 show that it is almost impossible to distinguish the double disk model from the thin disk + flat halo model. In other words, thick disks thought to exist in many spiral galaxies including our own may, infact, be flat halos. To distinguish these two models, for edge-on galaxies, the light profile of 10-15 kpc region from the galactic plane must be investigated in detail. Then it must be determined which distribution best reproduces the data the exponential function or inverse proportionality to the square of galactocentric distance. For this purpose, high signal-to-noise ratio observations, usually carried out by a large telescope looking at a wide field of view like SUBARU, is needed.

If the observed light profile comes from the flat halo, it is inferred from the color information and the mass-to-light ratio that the flat halo is composed of red dwarfs with the mass of $0.3 - 0.4 M_{\odot}$. This interpretation indicates that all the dark matter in IC5249 can be explained by the presence of baryonic matter.

In order to verify the flat halo model involving of red dwarfs, this model was applied to our Galaxy and examined whether the observed data of the dark matter in our Galaxy could be reproduced(Appendix A and B). It turned out that the flat halo model reproduced the rotation curve of our Galaxy, the optical depth of microlensing effect and the number of stars observed by HST toward high galactic latitudes.

Chapter 7

Conclusion

In order to solve the dark matter problem of spiral galaxies, the southern edge-on galaxy IC5249 was observed for 9 hours in the V passband and 6 hours in the I passband using the MOA observation system from August to November in 1998. As a result, an extended light profile in addition to the thin disk was discovered. In order to examine what the source of the light profile was, the observed data of IC5249 was fit to four models. They were the double disk model, the thin disk + globular clusters model, the thin disk + spherical halo model and the thin disk + flat halo model. The results of fitting indicated that the observed data can be well reproduced by the double disk model or the thin disk + flat halo model, which means that the source of the light profile is a thick disk or the flat halo. The color of the light profile was $V-I = 1.3-1.5 magnitude$. If the light profile was assumed to come from a flat halo, the mass-to-light ratio was 18-24(in unit of $M_\odot/L_\odot$) from the rotational velocity(100 km/s) and the observed brightness of IC5249. These observational results were compared with the properties of low metal red dwarfs calculated by Baraffe et al(Baraffe et al 1997) and it was concluded that the flat halo was composed of 0.3-0.4$M_\odot$ red dwarfs.

Considering the circumstances mentioned above, the dark matter estimated from flat rotation curves of spiral galaxies is likely to be composed of red dwarfs, viz baryonic matter. However, the observations of IC5249 did not allow one to distinguish between the flat halo model from the thick disk model.

Acknowledgement

First of all, I would like to express my deepest gratitude to my supervisor Prof. Yasushi Muraki, who gave me many chances to learn various things especially about scientific experiment. Also I would like to thank Prof. Maki Sekiguchi(Institute for Cosmic Ray Research, University of Tokyo) who gave me many advices and supports for constructing our mosaic CCD camera MOA-cam2.

I am grateful to Prof. Philip Yock(Auckland Unversity), Prof. Yutaka Matsubara, Prof. Kimiaki Masuda, Prof. Fumio Abe and Prof. Shuji Sato for supporting my work on MOA collaboration, many advices and checking my manuscript. I am quite indebted to Mrs Pam Kilmartin, Mr Alan Gilmore, Dr Ian Bond, Mr Nick Rattenbury and Mr Glenn Pennycook for observations and various helps in Mt John University Observatory.

I would like to thank students of MOA collaboration in Solar-Terrestrial Environment laboratory, Miss Sachiyo Noda, Mr Takahiro Sumi, Mr Yuji Kato and Mr Chikahisa Noguchi. Discussions with them at the weekly seminar were highly stimulating for me. Also I would like to thank other members of MOA collaboration, Prof. Mitsuaki Fujimoto, Prof. John Hearnshaw, Prof. Denis Sullivan, Mr Micheal Reid, Mr Brian Carter, Dr. Richard Dodd, Mr Garry Nankivell, Dr. Noiman Rumsey, Dr. Morihiro Honda, Prof. Masanori Yoshizawa, Prof. Takashi Nakamura, Prof. Fumitaka Sato, Prof. Seiji Kabe, Prof. Makoto Kobayashi, Prof. Yoshiyuki Watase, Prof. Jun Jugaku, Prof. Toshiharu Saito, Prof. Barbel Koribalski, Prof. Koji Ohnishi, Dr. Yukitoshi

Kan-ya and Dr. Mareki Honma.

I thank the members of the cosmic ray group in the Solar-Terrestrial Environment laboratory, Mr Takuya Murata, Mr Harufumi Tsuchiya, Mr Akira Yuki, Mr Syuhei Ohno, Mr Masataka Kato and Mr Hiroaki Toyoizumi. And also to the staff in the laboratory, I express my great thanks.

Finally, My deep thanks go to my wife Mimi, my daughter Mayuka, my parents, my younger sister and my wife's parents, who always support me warmly and kindly.

References

Abe F. et al., 1997, Variables Stars and the Astrophysical Returns of the Microlensing Surveys, 75

Abe F. et al., 1999, AJ, 118, 261

Adams F. C., Laughlin G., 1997, ApJ, 468, 586

Afonse C. et al., 1999, A&A, 344, 63

Alard C,. Mao S., Guibert J., 1995, A&A, 300, L17

Alcock C. et al., 1993, Nature, 365, 621

Alcock C. et al., 1996, ApJ, 461, 84

Alcock C. et al., 1997, ApJ, 486, 697

Alcock C. et al., 1998, ApJ, 499, L9

Ansari R. et al., 1997, A&A, 1997, 324, 843

Aoki T. E., Hiromoto N., Takami H., Okamura S., 1991, PASJ, 43, 755

Arimoto N, 1982, "Globular Cluster", Chijin-Shokan, 187

Auburg E. et al., 1993, Nature, 365, 623

Bahcall J. N., Flynn C., Gould A., 1992, ApJ, 389, 234

Bahcall J. N., Flynn C., Gould A., Kirhakos S., 1994, ApJ, 435, L51

Bahcall J. N., Kylafis N. D., 1985, ApJ, 288, 252

Bahcall J. N., Schmidt M., Soneira R. M., 1982, ApJ, 258, L23

Baraffe I., Chabrier G., Allard F., Hauschildt P. H., A&A, 327, 1054

Barnaby D., Thronson Jr. H. A., 1992, AJ, 103, 41

Bertin G., Lin C. C., 1987, Proceedings of the 10th IAU European Regional Astronomy Meeting, 255

Binney J., Tremaine S., 1987, "Galactic Dynamics", Princeton press
Burkert A., Yoshii Y., MNRAS, 282, 1349
Burstein D., 1979, ApJ, 234, 829
Carberg R. G., Sellwood J. A., 1985, ApJ, 292, 79
Casali M. M., James P. A., 1995, MNRAS, 274, 265
Chabrier G., Segretain L., Mera D., 1996, ApJ, 486, L21
Charlot S., Silk J., 1995, ApJ, 445, 124
da Costa L. N., Pellegrini P. S., Davis M., Meiksin A., Sargent W. L. W., Tonry J. L., 1991, ApJS, 75, 935
de Grijs R., 1997, PhD thesis, Kapteyn Astronomical Institute
de Grijs R., Peletier R.F., 1997, A&A, 320, L21
de Grijs R., Peletier R.F., van der Kruit P. C., 1997, A&A, 327, 966
de Jong R. S., van der Kruit C., 1994, A&AS, 106, 451
Dekel A., Shalosman I., 1983, IAU Symposium No.100, 197
Dubinski J., 1994, ApJ, 431, 617
Eggen O. J., Lynden-Bell D., Sandage A. R., 1962, ApJ, 136, 748
Evans N. W., 1994, MNRAS, 267, 333
Flynn C., Gould A., Bahcall J. N., 1996, ApJ, 466, L55
Freeman K. C., 1985, IAU Symposium No.106, 113
Fuchs B., Wielen R., The Galaxy,Proceedings of the NATO Advanced Study Institute, 375
Gilmore A., 1994, Private communication
Gilmore G., 1984, MNRAS, 207, 223
Gilmore G., Reid N., 1983, MNRAS, 202, 1025
Gilmore G., Unavane M., 1998, MNRAS, 301, 813
Gould A., Miralda-Escude J., Bahcall J. N., 1994, ApJ, 423, L105
Graff D. S., Freese K., 1996, ApJ, L49
Guth A., 1981, Phys. Rev., D23, 347

Harris W. E., Racine R., 1979, Ann.Rev.Astron.Astrophys, 17, 241
Hernquist L., 1990, ApJ, 356, 359
Hoffner P., Sparke L., 1994, ApJ, 428, 466
Honma M., 1999, PhD thesis, University of Tokyo
Honma M., Kan-ya Y., 1998, ApJ, 503, L139
Ioka K., Tanaka T., Nakamura T., 1998, Abstracts of the 19th Texas Symposium on Relativistic Astrophysics and Cosmology, 480I
James P. A., Casali M. M., 1998, MNRAS, 301, 280
Jarvis B. J., Freeman K. C., 1985, ApJ, 295, 324
Jensen E. B., Thuan T. X., 1982, ApJS, 50, 421
Kent S. M., 1984, ApJS, 56, 105
Kent S. M., Dame T., Fazio G., 1991, ApJ, 378, 131
Kuijken K., Gilmore G., 1989, MNRAS, 239, 605
Kylafis N. D., Bahcall J. N., 1987, ApJ, 317, 637
Lacey C. G., 1984, MNRAS, 208, 687
Lequex J., Dantel-Fort M., Fort B., 1995, A&A, 296, L13
Lequex J., Fort B., Dantel-Fort M., Cuillandre J. -C., Mellier Y., 1996, A&A, 312, L1
Lequex J., Combes F., Dantel-Fort M., Cuillandre J. -C., Fort B., Mellier Y., 1998, A&A, 334, L9
Levasseur P., Carignan C., Byun Y. -I., 1992, Proposal No.C212 to the Australia Telescope National Facility
Mathewson D. S., Ford V. L., Buchhorn M., 1992, ApJS, 81, 413
Miyamoto M., Nagai R., 1975, PASJ, 27, 533
Morrison H. L., Boroson T. A., Harding P., 1994, AJ, 108, 1191
Muraki Y. et al., 1999, PTPS, 133, 233
Noda S., 1999, M.Sc. thesis, Nagoya University
Norris J., 1987, The Galaxy,Proceedings of the NATO Advanced Study In-

stitute, 297
Olling R. P., 1995, AJ, 110, 591
Oort J. H., 1960, Bull. Astron. Inst. Netherlands, 15, 45
Paczynski B., 1986, ApJ, 304, 1
Palanque-Delabrouille N. et al., 1998, A&A, 332, 1
Press W. H., Teukolsky S. A., Vetterling W. T. Flannery B.P., 1992, "Numerical Recipes", Cambridge press, 406
Quinn P. J., Hernquist L., Fullagar D. P., 1993, ApJ, 403, 74
Rauscher B.J. et al., 1998, ApJ, 506, 116
Rattenbury N.J., 1999, M.Sc. thesis, University of Auckland
Rhie S. H. et al., 1998, AAS, 193, 108.05
Roberts M. S., Haynes M. P., 1994, ARA&A, 32, 115
Rubin V. C., Ford W. K. Jr., 1970, ApJ, 159, 378
Rubin V. C., Thonnard N. T., Ford W. K. Jr., 1980, ApJ, 238, 471
Rubin V. C., Thonnard N. T., Ford W. K. Jr., Burstein D., 1982, ApJ, 261, 439
Rubin V. C., Burstein D., Ford W. K. Jr., Thonnard, N. T., 1985, ApJ, 289, 81
Rudy R.J., Woodward C. E., Hodge T., Fairfield S.W., Harker, D. E., 1997, Nature, 387, 159
Sackett P. D., Gould A., 1993, ApJ, 419, 648
Sackett P. D., Morrison H. L., Harding P., Boroson T. A., 1994, Nature, 370, 441
Sackett P. D., Rix H., Jarvis B., Freeman K. C., 1994, ApJ, 436, 629
Sackett P. D., Sparke L., 1990, ApJ, 361, 408
Sancisi R., van Albada T. S., 1987, IAU Symposium No.117, 67
Sargent W. L. W., 1987, IAU Symposium No.124, 777
Sato K., 1981, MNRAS, 195, 467

Scalo J. M., 1986, Fundam. Cosmic Physics, 11, 1
Searle L., Zinn R., 1978, ApJ, 225, 357
Sekiguchi M., Iwashita H., Doi M., Kashikawa N., Okamura S., 1992, PASP, 104, 744
Sekiguchi M., Nakaya H., Kataza H., Miyazaki S., 1998, ExA, 8, 51
Shang Z. et al., 1998, ApJ, 504, L23
Shaw M. A., Gilmore G., 1990, MNRAS, 242, 59
Simien F., de Vaucouleurs G., 1986, ApJ, 302, 564
Sofue Y., 1996, ApJ, 458, 120
Sparke L., Casertano S., 1988, MNRAS, 234, 873
Spitzer L., Schwarzschild M., 1951, ApJ, 114, 385
Statler T. S., 1989, ApJ, 344, 217
Sumi T., 1999, M.Sc. thesis, Nagoya University
Tody D., 1986, Proc. SPIE, 627, 733
Tomaney A. B., Crotts A. S., 1996, AJ, 112, 2872
Toomre A., 1983, IAU Symposium No.100, 177
Udalski A., Kubiak M., Szymanski M., 1997, AcA, 47, 319
Uemizu K. et al., 1998, ApJ, 506, L15
van der Kruit P. C., Searle L., 1981a, A&A, 95, 105
van der Kruit P. C., Searle L., 1981b, A&A, 95, 116
van der Kruit P. C., Searle L., 1982a, A&A, 110, 61
van der Kruit P. C., Searle L., 1982b, A&A, 110, 79
van Dokkum P. G., Peletier R. F., de Grijs R., Balcells M., 1994, A&A, 286, 415
Wainscoat R. J., Freeman K. C., Hyland A. R., 1989, ApJ, 337, 163
Walterbos R. A. M., Kennicutt R. C., 1987, A&AS, 69, 311
Wevers B. M. H. R., van der Kruit P. C., Allen R. J., 1986., A&AS, 66, 505
Yanagisawa T., 1996, M.Sc. thesis, Nagoya University

Yanagisawa T. et al., 1999, submitted to ExA
Yokoyama J., 1997, A&A, 318, 673
Zheng Z. et al., 1999, AJ, 117, 2757
Zwicky F., 1933, Helv. Phys. Acta, 6, 110

Appendix A

Application of "the flat halo model with single red dwarf" to our Galaxy

In this thesis, it was shown that the light profile observed in IC5249 in addition to the thin disk might be caused by the flat halo, and its composition might be red dwarf. In appendix A, I applied the flat halo model composed of red dwarfs to our Galaxy and examined whether it reproduced observed results about dark matter of our Galaxy. In this model, whole red dwarfs, which construct the flat halo, have the same mass of 0.3-0.4 $M_{\odot}$(see Chapter 6). This model is called "the flat halo model with single red dwarf",or just "S model" for simplicity after this.

A.1 Rotation curve

Many spiral galaxies including our Galaxy show flat rotation curves(Sofue 1996). The rotation curve of our Galaxy is shown in Figure A.1. Rotation curves of our Galaxy with some cases of "S model" were drawn using parameters described in Table 6.7 and compared with the observed result shown in Figure A.1.

Four components which contribute to the rotation curve were considered. Those were central mass concentration(black hole), the bulge, the thin disk

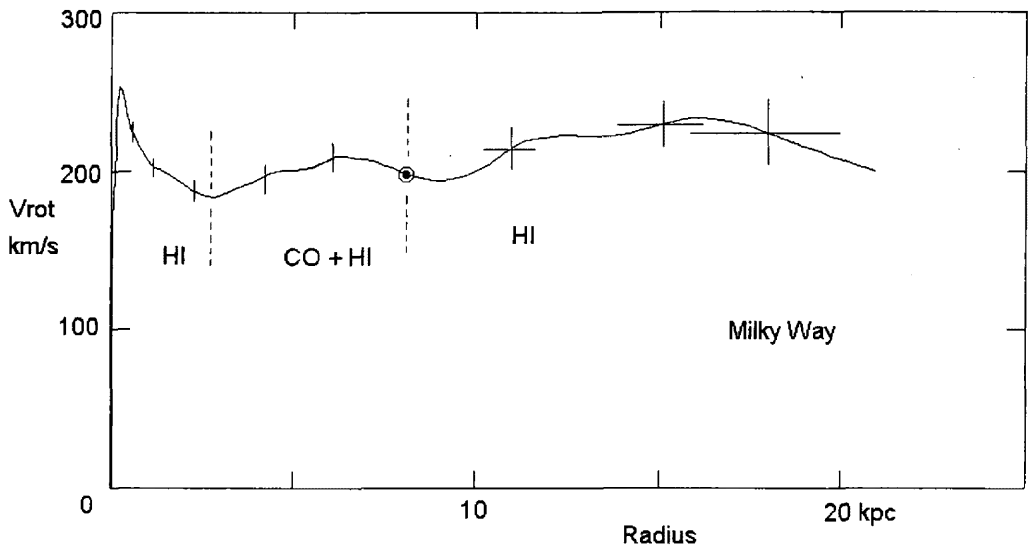

Figure A.1: The rotation curve of our Galaxy. The horizontal axis shows the distance from the galactic center along the galactic plane in kpc, and the vertical axis shows the rotation velocity in km/s.

and the flat halo, respectively. Rotation velocity caused by each component is calculated from the gravitational potential of it using equation (A.1).

$$V_i = \left(R \frac{\partial \Phi_i}{\partial R} \right)^{\frac{1}{2}} \quad , i = BH, bulge, disk, halo \tag{A.1}$$

The Miyamoto-Nagai potential(Miyamoto & Nagai 1975) was used for the gravitational potentials of central black hole and the bulge. The Miyamoto-Nagai potential is described in equation (A.2).

$$\Phi_i(R,z) = \frac{GM_i}{\left\{ R^2 + \left[a_i + (z^2 + b_i^2)^{1/2} \right]^2 \right\}^{1/2}} \quad , i = BH, bulge \tag{A.2}$$

Here G and M_i are gravitational constant and total mass of each component.

a_i and b_i are scale height and scale length of each component, respectively. In spherical mass distribution, a_i becomes $a_i = 0$ and b_i indicates the scale radius of its mass distribution. For central black hole, M, a and b were considered $5 \times 10^9 M_\odot$, $0pc$ and $120pc$,respectively. For the bulge, those parameters are considered $10^{10} M_\odot$, $0pc$ and $750pc$, respectively. The rotation velocity of the potential is described in equation (A.3) using equation (A.1).

$$V_i = \sqrt{\frac{GM_iR^2}{(R^2 + b_i^2)^{3/2}}} \quad , i = BH, bulge \tag{A.3}$$

The gravitational potential of the thin disk component is described as equation (A.4) when the surface mass density is $\Sigma(R) = \Sigma_0 exp(-R/R_d)$(Binney & Tremaine 1987).

$$\Phi_{disk}(R,0) = -\pi G\Sigma_0 R[I_0(y)K_1(y) - I_1(y)K_0(y)] \quad , y \equiv R/2R_d \tag{A.4}$$

Here I_n and K_n are modified Bessel functions. R_d is the scale length of the thin disk and the value of 3.5 kpc was used (Bahcall et al 1982). The surface mass density of the Galactic center Σ_0 was calculated on the assumption that the distance to the Galactic center was 8.5 kpc(Bahcall et al 1982). For surface mass density of the solar neighborhood, Kuijken and Gilmore showed the value of $\Sigma_{solar} = 46 \pm 9 M_\odot/pc^2$(Kuijken & Gilmore 1989) and Bahcall, Flynn and Gould showed $\Sigma_{solar} = 88 M_\odot/pc^2$ (Bahcall, Flynn & Gould 1992). The rotation curve of our Galaxy is examined with changing surface mass density of the solar neighborhood (Σ_{solar}) from 37 to $88 M_\odot/pc^2$. The relationship between surface mass density of the Galactic center(Σ_0) and solar neighborhood(Σ_{solar}) is described in equation (A.5).

$$\Sigma_0 = \Sigma_{solar} exp(R_0/R_d) \tag{A.5}$$

Here R_0 is the distance to the Galactic center(8.5 kpc). From equation (A.1) and (A.4), rotation velocity of the thin disk profile is given by equation (A.6).

$$V_{disk} = \sqrt{4\pi G\Sigma_0 R_d y^2 [I_0(y)K_0(y) - I_1(y)K_1(y)]} \tag{A.6}$$

The spherical power law model of Evans(Evans 1994; equation (6.9)) was used for "S model" halo. The rotation velocity of "S model" halo is given by equation (6.10). The rotation velocity caused by whole components is calculated by equation (A.7).

$$V_{total} = \sqrt{V_{central}^2 + V_{bulge}^2 + V_{disk}^2 + V_{halo}^2} \tag{A.7}$$

By adopting the above relations, the rotation curve of our Galaxy was extracted using the some parameter sets of the flat halo models shown in Table 6.7. At this time, the surface mass density of solar neighborhood was chosen in the range from $37 M_\odot/pc^2$ to $88 M_\odot/pc^2$ to adjust the rotation velocity around the sun($R = 8.5 kpc$) is 210 km/s. The parameters of "S model" halo(core radius and axial ratio) and surface mass density of solar neighborhood in each model are described in Table A.1. Rotation curve of each model is shown in Figure A.2.

In Figure A.2, diamond, plus, square, cross and triangle show the rotation curves of our Galaxy possessing "S model" halo with the core radius of 5.75, 10, 20, 30 and 40 kpc, respectively. Five rotation curves in Figure A.2 reproduce the observed rotation curve of our Galaxy shown in Figure A.1 well.

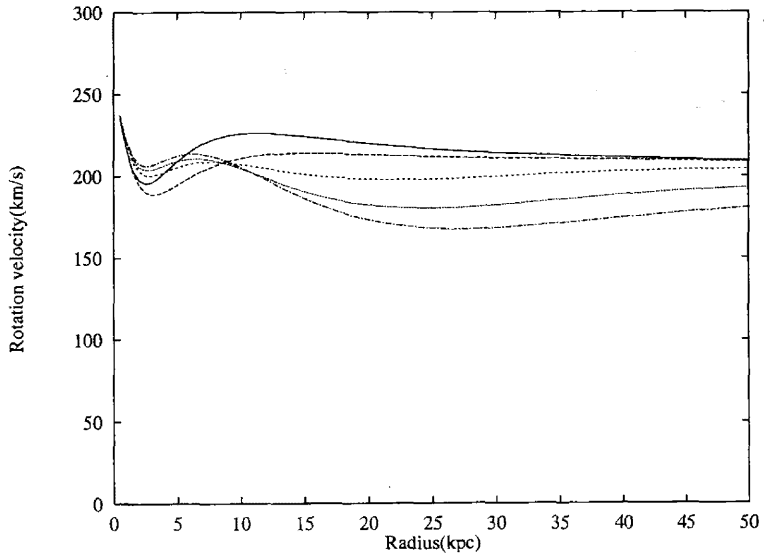

Figure A.2: The rotation curves of thin disk + flat halo model. The solid line, the long dashed line, short dashed line, dotted line and dotted-dashed line represent the rotation curves of thin disk + flat halo model with the core radius of 5.75kpc, 10kpc, 20kpc, 30kpc and 40kpc, respectively.

A.2 Observation of microlensing effect

In this section, it was examined whether "the flat halo model with single red dwarf" applied to our Galaxy reproduce the observed result of microlensing effect.

The mass of MACHO is estimated from the duration of microlensing effect. Duration of microlensing effect is transit time of back ground star through a circle of Einstein radius, which is defined by equation (A.8).

$$t_{event}(l) = \frac{\pi R_E(l)}{2 < |v_\perp| >}, \quad R_E(l) = \sqrt{\frac{4Gm}{c^2}\frac{l(D_s - l)}{D_s}} \tag{A.8}$$

Here l, R_E, $v_\perp$, G, m, c and D_s are distance to MACHO, Einstein radius,

Table A.1: Parameters for rotation curves

Halo core radius(kpc)	Axial ratio	Surface mass density($M_\odot/pc^2$)
5.75	0.467	37.0
10.0	0.422	46.0
20.0	0.323	72.5
30.0	0.263	80.0
40.0	0.211	85.0

perpendicular velocity of MACHO to observer's line of sight, gravitational constant, mass of MACHO, light velocity and distance to background star, respectively. It is shown in equation (A.8) duration of microlens effect is decided by three parameters, mass, position and velocity of MACHO. In order to extract mass of MACHO from duration of microlensing effect, two other parameters have to be assumed by some models.

The contribution of MACHO to dark matter of our Galaxy (fraction) is the ratio of observed optical depth τ_{obs} to that of some model, which describe density distribution of MACHO. Observed optical depth is defined by equation (A.9).

$$\tau_{obs} = \frac{1}{E}\frac{\pi}{4}\sum_i \frac{t_{event,i}}{\varepsilon(t_{event,i})} \tag{A.9}$$

Here E is total exposure(number of stars×total exposure time) and $\varepsilon(t_{event})$ is detection efficiency of the microlensing effect with duration of t_{event}. Optical depth calculated from one model is given by equation (A.10).

$$\tau_{model} = \frac{4\pi G}{c^2}\int_0^{D_s} \rho(l)\frac{l(D_s-l)}{D_s}dl \tag{A.10}$$

Here $\rho(l)$ is the density distribution of MACHO. MACHO collaboration indicated that their observed optical depth was $\tau_{obs} = 2.9^{+1.4}_{-0.9} \times 10^{-7}$. They concluded that a half of the dark matter of our Galaxy were made of MACHOs in consideration of $\tau_{model} = 5.0 \times 10^{-7}$ calculated by standard halo model. The density distribution of standard halo model is given by equation (A.11).

$$\rho(r) = \rho_0 \frac{R_0^2 + a^2}{r^2 + a^2} \tag{A.11}$$

Here $\rho_0 (= 0.0079 M_\odot / pc^3)$, $R_0 (= 8.5 kpc)$ and $a (= 5.0 kpc)$ are halo density of solar neighborhood, distance to the Galactic center and core radius of the halo, respectively.

τ_{model} was calculated by appling the flat halo model of equation (6.11) with some parameter sets(Table 6.7) to $\rho(l)$ of equation (A.10), and compared with τ_{obs} obtained by the observation of MACHO collaboration. In Table A.2, used parameters of the flat halo model(core radius and axial ratio), τ_{model} and τ_{obs}/τ_{model}(fraction) are described. From Table A.2, it is understood that almost

Table A.2: optical depth of "the flat halo model with single red dwarf"

Halo core radius(kpc)	Axial ratio	$\tau_{model}(\times 10^{-7})$	τ_{obs}/τ_{model}
0.0	0.567	5.0	$0.58^{+0.28}_{-0.18}$
5.75	0.467	4.1	$0.71^{+0.34}_{-0.22}$
10.0	0.422	3.9	$0.74^{+0.36}_{-0.23}$
20.0	0.323	3.1	$0.94^{+0.45}_{-0.29}$
30.0	0.263	2.7	$1.07^{+0.52}_{-0.33}$
40.0	0.211	2.4	$1.21^{+0.58}_{-0.38}$

dark matter of our Galaxy is composed of MACHOs in the flat halo models with core radius of 20, 30 and 40 kpc. The decrease of axial ratio with the

decrease of τ_{model} is interpreted as follows. The decrease of axial ratio means halo shapes becomes flatter along galactic plane. As a result, the total mass of halo component, which enter into microlens tube, is decreased. From Table A.2, It is obvious that τ_{model} is changeable with the model adopted. The conclusion of MACHO collaboration, that a half of dark matter of our Galaxy is composed of MACHOs, is correct with only standard halo model. The average event duration observed by MACHO collaboration was 61 days. Equation (A.8) indicates typical mass of MACHO is $0.4M_{\odot}$ in consideration of the perpendicular velocity of MACHO to line of sight, 200 km/s(Paczynski 1986). These correspond with the results described in Chapter 6, which means the flat halo of IC5249 is composed of red dwarfs with the masses of 0.3-0.4$M_{\odot}$.

A.3 Photometry by HST toward high galactic latitude region

In this section, it was examined whether "the flat halo model with single red dwarf" applied to our Galaxy reproduced the observed result of photometry by HST(Hubble Space Telescope) toward high galactic latitude region.

Bahcall et al observed high galactic latitude region ($l = 148°, b = -51°$) with the size of 4.4 square arcminutes using WFPC2(Wide Field Planetary Camera 2) of HST. Exposure time of V' (F606W) filter and I'(F814W) filter were 2 hours and 2.83 hours, respectively. As a result, they detected fifteen stars(Bahcall et al 1994). The limiting magnitude of their observation in I passband was $I_{max} = 25.3mag$ with $V - I > 2.0$ and $I_{max} = 24.7mag$ with $V - I < 2.0$.

Their result is shown in Figure A.3. They concluded from their observation result that contribution of red dwarf to dark matter of our Galaxy was less than 6 %. From same observation result, Graff and Freese indicated that the

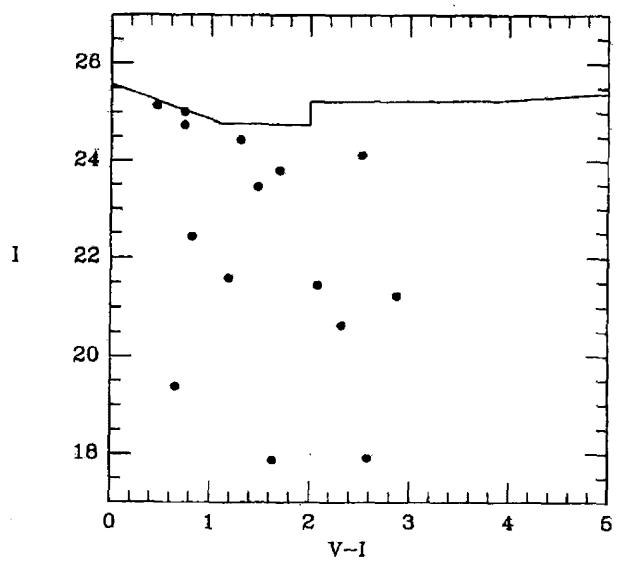

Figure A.3: The observation result by Bahcall et al. using HST. The horizontal axis shows the V-I magnitude, and the vertical axis shows the I magnitde. The solid line represents the limiting magnitude of HST and dotted points are the stars detected by HST.

contribution was 0.14-0.37 % in consideration of low metalicity of halo stars. Also, they showed the contribution of red dwarf and brown dwarf was 0.25-0.67 % on assumption that the initial mass function(IMF) was described as $1/M$(Graff & Freese 1996).

The total mass toward observed direction of HST was estimated in consideration of "the flat halo model with single red dwarf", and compared with the observed result of Bahcall et al. All fifteen stars detected by them were assumed that their color and the mass were $V - I = 1.39$ and $0.3M_{\odot}$ which were obtained by the observation of IC5249 (see Chapter 6). The total mass toward observed direction of HST is calculated by equation (A.12).

$$M_{HST} = \int_0^{d_{max}} \rho(l)\Omega l^2 dl \qquad \text{(A.12)}$$

d_{max} is observable distance for HST under the limiting magnitude which is described in equation (A.13).

$$d_{max} = 10^{0.2(I_{max}-M_I)+1}pc \tag{A.13}$$

M_I was considered from Table 6.9 to be $M_I = 8.19$ by the color information $V - I = 1.39$ assumed above. This leads to $d_{max} = 20kpc$ with equation (A.13). $\rho(l)$ is density distribution of the flat halo model (equation (6.11)) and $\Omega(= 3.723 \times 10^{-7} sr)$ is observable solid angle for HST. The expected observable number of stars with HST in "the flat halo model with single red dwarf" is estimated by dividing the total mass M_{HST}(equation (A.12)) by the mass of red dwarf ($0.3M_{\odot}$). In Table A.3, the expected number of stars and upper limit ratio of actually observed number of stars by HST to the expected number with 95 % confidence level are shown. From Table A.3, it is understood that "the

Table A.3: Expected number of stars by HST observation

Halo core radius(kpc)	Axial ratio	Number of stars	Low mass star ratio(%)
0.0	0.567	3326	0.69
5.75	0.467	1938	1.2
10.0	0.422	1988	1.2
20.0	0.323	1815	1.3
30.0	0.263	1752	1.3
40.0	0.211	1594	1.4

flat halo model with single red dwarf" does not explain observed result of HST. Observed number of stars by HST is less than 1 % of that obtained from the model.

From Table A.3, it is shown that the expected number of stars decreases with increase of flatness(decrease of axial ratio) of the flat halo. This is interpreted as follows. As shown in Figure A.4, the density of the halo increases with increase of the flatness. However, in case flatter halo is observed with fixed solid angle, decrease of observable region excels increase of the density. In other words, to detect same number of stars in flatter halo, wide solid angle as shown in Figure A.4 by dotted-dashed line must be observed. Graff and Freese concluded the contribution of low metal red dwarf to the dark matter of our Galaxy was 0.14-0.37 %. However, they assumed the density distribution of the halo to be spherical. As a result, expected number of stars increased and they underestimated the contribution which was the ratio of number of observed stars to that of expected ones. The value of this section is five times theirs.

From above consideration, it seems that the observed result of HST is reproduced in case the halo is extremely flat. I examined how flat the halo should be with various core radiuses to explain the observed result of HST. As the process above, I assumed that whole fifteen stars detected by HST have the color information of $V - I = 1.39$ and mass of 0.3 $M_{\odot}$, and total mass of the flat halo was composed of these stars. Equation (A.12) and (A.13) were used for the examination. In Table A.4, the parameters of the flat halo which reproduces the observed result of HST(core radius and axial ratio) and optical depth of microlensing τ_{model} calculated by equation (A.10) are shown.

From Table A.4, it is clear that the flat halo model with the axial ratio of less than 0.1 reproduces observed result of HST. Also, optical depth of microlensing corresponds to lower limit of that indicated by MACHO collaboration(2.0×10^{-7}; Alcock et al 1997) with 15 % difference. The flat halo with the axial ratio of less than 0.1 was not observed in IC5249 and other edge-on galaxies until present day. However, such a flat halo is quite attractive as it explains rotation

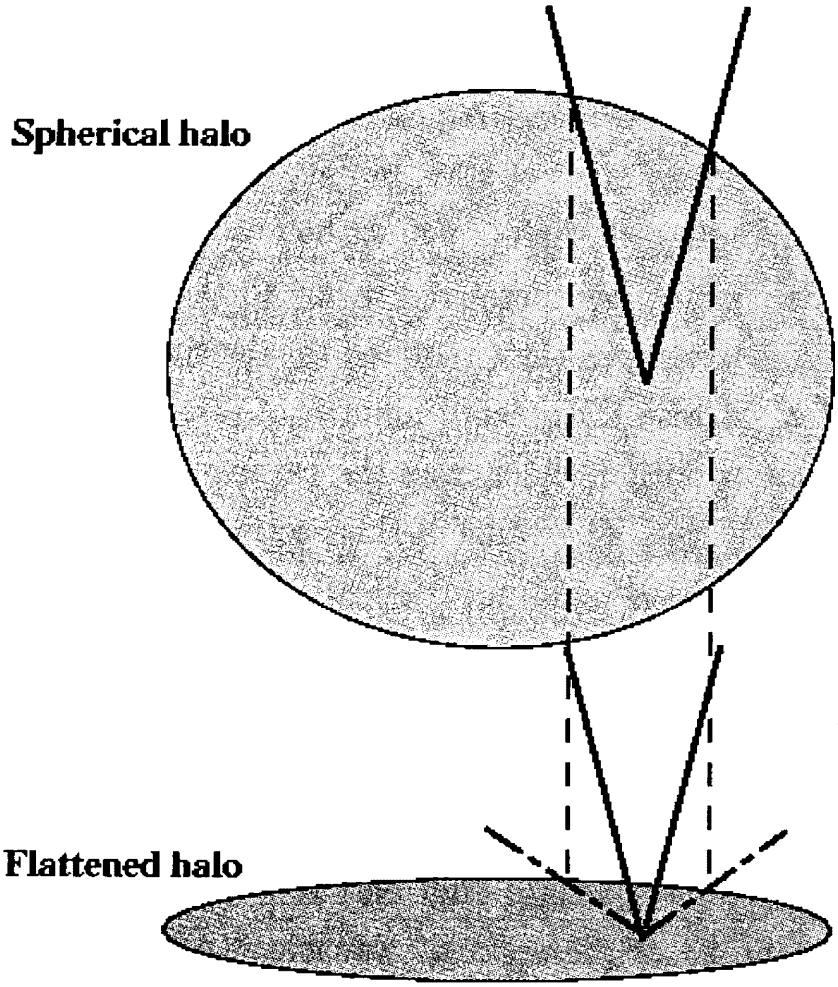

Figure A.4: The increase of the flatness and the decrease of observable region.

Table A.4: The parameters of the flat halo which reproduces observed result of HST

Halo core radius(kpc)	Axial ratio	$\tau_{model}(\times 10^{-7})$
0.0	0.09	1.6
5.75	0.076	1.7
10.0	0.060	1.7
20.0	0.037	1.7
30.0	0.026	1.7
40.0	0.020	1.8

curve of our Galaxy, optical depth of microlensing and observed result by HST. In case such a halo exists in some galaxies, it is impossible to detect that since the thin disk is too bright.

A.4 Summary of Appendix A

The flat halo model composed of red dwarfs of unique mass ("the flat halo model with single red dwarf") was applied to our Galaxy and examined whether it reproduces some observed results about dark matter of our Galaxy. As a result, the flat halo model reproduced rotation velocity of our Galaxy and optical depth of microlensing effect. However, the number of stars observed by HST toward high galactic latitude was too low to explain the model(1.2 %). This means only 1.2 % of the dark matter of our Galaxy is composed of red dwarf. Finally, It was understood that "the flat halo model with single red dwarf" reproduced these three observed results in case the halo was extremely flat.

Appendix B

Application of "the flat halo model with various red dwarfs" to our Galaxy

In Appendix B, I considered the flat halo which possessed various kind of red dwarfs in layer as drawn in Figure B.1. I call this halo model "the flat halo model with various red dwarfs". Here, I applied this model to our Galaxy and examined whether this model reproduced some observed results about dark matter of our Galaxy.

B.1 The flat halo model with various red dwarfs

The observed data of IC5249 indicate the color profile of this galaxy becomes redder according as the distance from galactic plane increases(Figure 5.17). This phenomena was observed in NGC5907(Lequeux et al 1996; Figure B.2) and NGC7814(Lequeux, Dantel-Fort & Fort 1995). In Table 6.9, it is clear that the value of V-I increases(the color becomes redder) according as mass of red dwarf becomes lighter. The halo, which possesses heavy red dwarfs near galactic plane and light ones at far region from the plane, explains above phenomena. Therefore, I considered "the flat halo model with various red dwarfs" which is composed of three types of red dwarfs existing different regions in the halo as shown in Figure B.1. For simplicity, I call "the flat halo model with various red dwarfs" "V model" sometimes. It was assumed that red dwarfs with

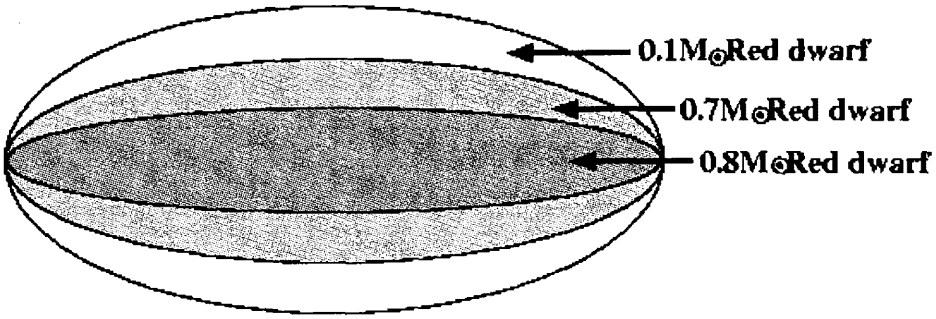

Figure B.1: The flat halo model with various red dwarfs. The red dwarfs with different mass exist in layer inside flat halo. The red dwarfs with $0.8M_{\odot}$ exist around the galactic plane. As the distance from galactic plane increases, the masses of red dwarfs decrease.

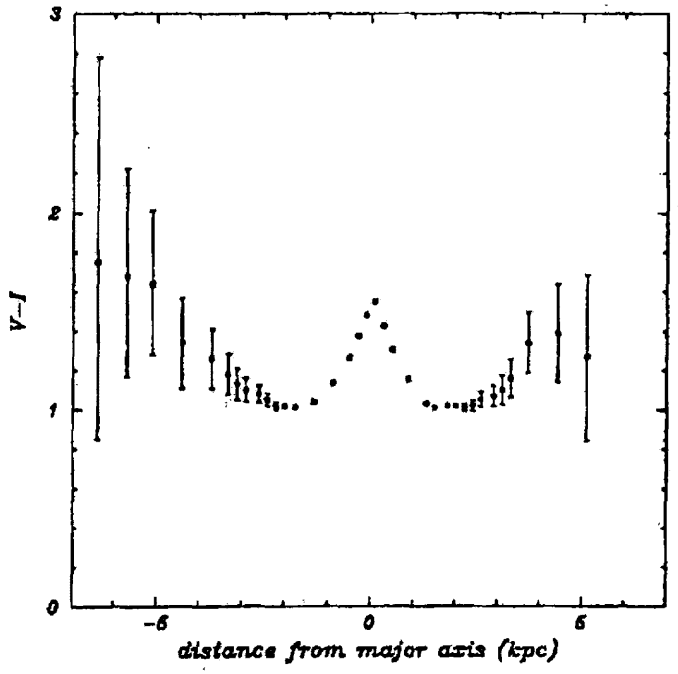

Figure B.2: The observation result of NGC5907 by Lequeux et al. The horizontal axis shows the perpendicular distance to the galactic plane in kpc, and the vertical axis shows the V-I magnitude.

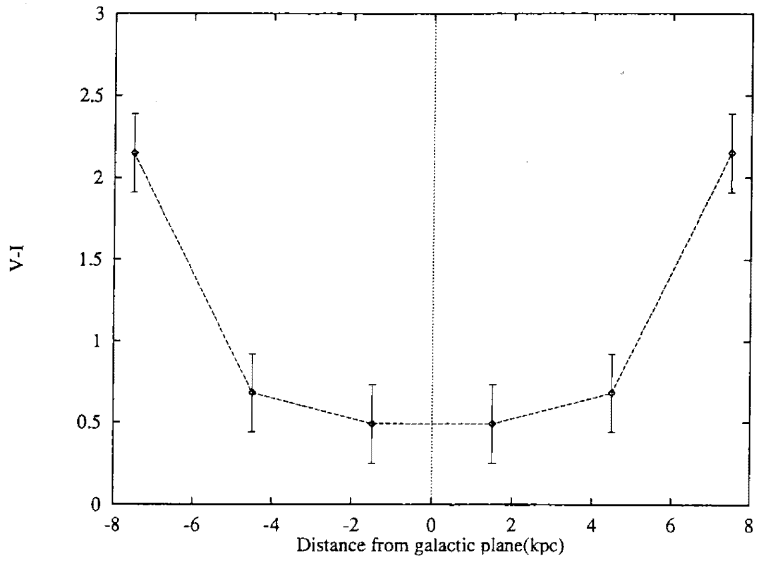

Figure B.3: The color profile of the flat halo model with various red dwarfs. The horizontalaxis shows the perpendicular distance to the galactic plane in kpc, andthe vertical axis shows the V-I magnitude.

the mass of 0.8, 0.7 and $0.1M_{\odot}$ exist in the region of 0-3 kpc, 3-6 kpc and 6-9 kpc from the Galactic plane, respectively. Color profile perpendicular to the galactic plane of "V model" is shown in Figure B.3. The observed color profile of IC5249(Figure 5.17) is well explained by Figure B.3.

B.2 Rotation curve

In this section, it was examined whether "the flat halo model with various red dwarfs" applied to our Galaxy reproduced the observed rotation curve of our Galaxy(Figure A.1).

It was assumed that rotation curve of our Galaxy including "V model" halo described above was composed of central black hole, bulge, thin disk and the flat halo as the case of "S model" in Appendix A. The rotation curve caused only by the flat halo was examined because other three components were same

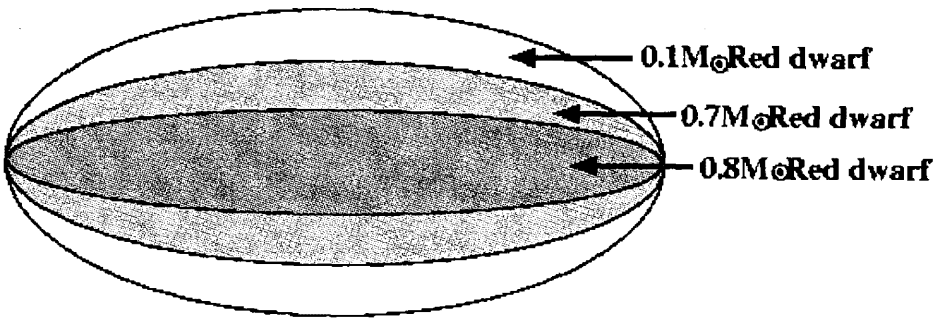

Figure B.4: The region used to extract the mass-to-light ratio of the flat halo model with various red dwarfs

as the case of "S model". In "S model", the light profile corresponds to mass distribution because the halo is made of one kind of red dwarf. In Table 6.9, it is shown that mass-to-light ratio of red dwarf increases according as the mass of it decreases. In other words, mass-to-light ratios differ with the region of the flat halo in "V model".

As a result, light profile of the halo dose not correspond to mass distribution. Therefore, mass-to-light ratio of the region described in Figure B.4 was calculated and compared with the mass-to-light ratio obtained by the observation of IC5249(Table 6.8). Some sets of parameters for the halo of "V model" were chosen from Table 6.8 and used for the calculation. The mass-to-light ratio was calculated as follows. Mass-to-light ratio of each region(0.36 at 0-3 kpc from the galactic plane, 1.3 at 3-6 kpc and 233 at 6-9 kpc) was multiplied by relative brightness obtained by using equation (6.11) and whole values were added up. In Table B.1, used parameters of the halo and the mass-to-light ratio of "V model" are described.

From table B.1, One found the mass-to-light ratios of "V model" with the

Table B.1: Mass-to-light ratio of "the flat halo model with various red dwarfs

core radius(kpc)	axial ratio	mass-to-light ratio ($M_\odot/L_\odot$)
0.0	0.507	0.61
5.75	0.467	0.49
10.1	0.422	2.99
20.1	0.323	12.6
30.2	0.263	23.0
40.3	0.211	25.1

core radius of 30.2 kpc(axial ratio is 0.263) and 40.3 kpc (axial ratio is 0.211) were almost equal to that of IC5249(Table 6.8). Rapid decrease of the mass-to-light ratio with decrease of core radius is interpreted as follows. Equation (6.11) indicates mass density near the galactic plane increases rapidly according as the core radius decreases. As a result, The influence of $0.8M_\odot$ red dwarf whose mass-to-light ratio is low (0.36) is enhanced near galactic plane and total mass-to-light ratio becomes low. In other regions at Figure B.4, mass-to-light ratios of "V model" halo with large core radius were also equal to that of IC5249. The mass-to-light ratios of both "S model" and "V model" are equal at any region of the Galactic plane. This means both models show same rotation curves and the Galaxy possessing "V model" halo reproduces the rotation curve of our Galaxy as "S model".

B.3 Observation of microlensing effect

In this section, I calculated optical depth τ_{model} of microlensing effect for "V model" by equation (A.10) and compared this with $\tau_{obs}(2.9^{+1.4}_{-0.9}\times10^{-7})$ extracted from the observation of MACHO collaboration. In equation (A.10), equation (6.11) was used for mass density ρ. However, mass-to-light ratios differ with the

distance from galactic plane. Therefore, the optical depth τ_{model} was calculated by adding up contribution of each region(0-3 kpc, 3-6 kpc and 6-9 kpc from galactic plane). Optical depth of each region is described as τ_{model} calculated by equation (A.10) times ratio of mass-to-light ratio of each region(0.36 at 0-3kpc, 1.3 at 3-6 kpc and 233 at 6-9 kpc from galactic plane) to observed one. τ_{model} and τ_{obs}/τ_{model}(fraction) were calculated for two models that explained the rotation curve of our Galaxy well(The models with core radius of 30.2 kpc and 40.3 kpc; see Table B.1). Obtained results are described in Table B.2.

Table B.2: Optical depth of "the flat halo model with various red dwarfs"

core radius(kpc)	axial ratio	$\tau_{model}(\times 10^{-7})$	τ_{obs}/τ_{model}
30.2	0.263	3.8	$0.76^{+0.37}_{-0.23}$
40.3	0.211	3.5	$0.83^{+0.40}_{-0.26}$

From Table B.2, one finds optical depth τ_{model} for "V model" corresponds well to τ_{obs} extracted by MACHO collaboration within the error.

B.4 HST photometry toward high Galactic latitude

In this section, I calculated detectable number of stars as "the flat halo model of various red dwarfs" was observed by HST and compared it with the actual observed result by HST(Bahcall et al 1994).

In Table B.3, properties of "V model" with distance from galactic plane are shown. In first column, Vertical distance form galactic plane are shown and corresponded values along the direction observed by HST($l = 148°, b = -51°$) are shown in round brackets. Second, third and fifth colum show mass of red dwarf, absolute magnitude of I passband and mass-to-light ratio, respectively.

Table B.3: Properties of "V model"

distance(kpc)	mass($M_\odot$)	$M_I(mag)$	d_{max}(Kpc)	mass-to-light ratio($M_\odot/L_\odot$)
0.0~3.0(0.0~3.9)	0.8	3.47	176	0.36
3.0~6.0(3.9~7.7)	0.7	4.83	94.0	1.3
6.0~9.0(7.7~11.6)	0.1	11.17	5.1	233

Those values are described in Table 6.9. Fourth column shows maximum observable distances by HST in case HST observes the star of the absolute magnitude described in third column. Table B.3 indicates it is impossible to observe $0.1M_\odot$ red dwarfs, which exist at 6.0-9.0 kpc from the galactic plane, by HST because of their darkness. Expected number of stars, in case "V model" halo is observed by HST, was calculated by equation (B.1).

$$N_{exp} = \frac{1}{0.8M_\odot}\int_{0.0}^{3.9}\frac{0.36}{24.0}\rho(l)\Omega l^2 dl + \frac{1}{0.7_\odot}\int_{3.9}^{7.7}\frac{1.3}{24.0}\rho(l)\Omega l^2 dl \qquad \text{(B.1)}$$

Here ρ and Ω are mass density of the flat halo given by equation (6.11) and observable solid angle of HST($3.723\times10^{-7}sr$). Two terms represent contributions of 0-3 kpc and 3-6 kpc region from the galactic plane, respectively. Contribution from each region was obtained by multiplying ρ in the region by the ratio of mass-to-light ratio of Table B.3 to observed mass-to-light ratio. Expected observable number of stars is sum of divided value of total mass of each region by red dwarf mass of each region. Expected number was calculated by equation (B.2) for two models that explained the rotation curve of our Galaxy well(The models with core radius of 30.2 kpc and 40.3 kpc; see Table B.1). The results are described in Table B.4.

From Table B.4, one found expected number of stars by HST observation toward the halo of "V model" corresponded well to actually observed number of stars(15). The expect number was one hundredth of that of "S model"(see

Table B.4: Expected number of stars by HST observation("V model")

core radius(kpc)	axial ratio	number of stars
30.2	0.263	19.3
40.3	0.211	17.7

Table A.3). The reason of this difference is interpreted as follows. The bright red dwarfs with low mass-to-light ratio near the galactic plane are able to emit the brightness around the galactic plane with small number. In the far region from galactic plane, many dim red dwarf with high mass-to-light ratio exist, but those are too far and dim to observe by HST. These two effects restrict the expected number of stars by HST observation.

B.5 Summary of Appendix B

I applied "The flat halo model with various red dwarfs", where three kind of red dwarfs existed in layer, to our Galaxy and examined whether some observed results about dark matter of our Galaxy were reproduced. As a result, I found this model explained rotation curve of our Galaxy, optical depth τ_{obs} of microlensing effect and observed number of stars by HST toward high galactic latitude well.